8-2009

THE REALITY OF THE WOLF 630 MOVING GROUP

Eric Bubar
Clemson University, ebubar@gmail.com

THE REALITY OF THE WOLF 630 MOVING GROUP

A Dissertation

Presented to

the Graduate School of

Clemson University

In Partial Fulfillment

of the Requirements for the Degree

Doctor of Philosophy

Physics

---

by

Eric J. Bubar

August 2009

Accepted by:
Dr. Jeremy R. King, Committee Chair
Dr. Sean D. Brittain
Dr. Dieter H. Hartmann
Dr. Gerald A. Lehmacher

ABSTRACT

The concept of relic kinematic assemblages from dispersed stellar clusters has remained contentious since Eggen's initial formulation of moving groups in the 1960's. However, the availability of high quality parallaxes from the Hipparcos space astrometry mission has resulted in distance measurements for thousands of nearby, seemingly isolated stars. With these newly determined distances, a high resolution spectroscopic abundance analysis can be brought to bear on many of the alleged members of these relic associations. If a structure is a relic of an open cluster, the members can be expected to be monolithic in age and abundance inasmuch as homogeneity is observed in young open clusters.

In this dissertation I have examined 34 members of the Wolf 630 moving group using high resolution stellar spectroscopy. The stars of the sample have been analyzed through a process known as "chemical tagging" to determine abundance homogeneity and confirm the existence of a homogeneous subsample of 20 stars. Fitting the homogeneous subsample with Yale-Yonsei isochrones, yields a single evolutionary sequence of $\sim$2.7 $\pm$ 0.5 Gyr. Additionally basic N-Body simulations, using the NEMO Stellar Dynamics toolkit, have been used to examine the kinematic evolution of typical star clusters in a model galactic disk potential that has been studded with Giant Molecular clouds. The results of these simulations suggests a high degree of kinematic coherence following spatial dissolution, validating that open clusters can maintain a common kinematic identity following their loss of spatial concordance. It is, therefore, concluded that moving groups can plausibly represent the relics of dissolved open clusters and that a 20 star subsample of the Wolf 630 moving group sample of 34 stars could represent such a dispersed cluster with an $<$[Fe/H]$>$=-0.01 $\pm$ 0.02 and an age of 2.7 $\pm$ 0.5 Gyr.

DEDICATION

This work is dedicated to my wife Rachel. Without your help, support and encouragement I would never have been able to suceed. Thank you for constantly believing in me, even when I didn't, and pushing me to do my best.

I would also like to thank my parents, John and Kathleen, you always encouraged me to pursue my education and ensured that I had everything I ever needed. With your support I have been able to finally get one of those "cool robes". Thanks to Bryan for always offering his assistance with job applications and advice on public speaking, and thanks to Matt for carting me around in my many trips to Arizona and for offering assistance whenever I needed it.

ACKNOWLEDGMENTS

My everlasting gratitude goes to Jeremy King for his guidance, advice and never ending patience. Without his support and mentoring I never would have been able to finish this work a year ahead of time! He has taught me a vast wealth of information and instilled in me a great appreciation for the subtle techniques which underly a proper abundance analysis. From observing proposals to refereed publications the list of things Jeremy has taught me is expansive.

Many thanks are also owed to my dissertation commitee for their willingness to serve; Jeremy King, Sean Brittain, Dieter Hartmann and Gerald Lehmacher.

Finally, this dissertation makes use of data products from the Two Micron All Sky Survey, which is a joint project of the University of Massachusetts and the Infrared Processing and Analysis Center/California Institute of Technology, funded by the National Aeronautics and Space Administration and the National Science Foundation. This research has also made use of the SIMBAD database, operated at CDS, Strasbourg, France.

TABLE OF CONTENTS

Table of Contents (Continued)

Page

LIST OF TABLES

LIST OF FIGURES

List of Figures (Continued)

Figure Page

List of Figures (Continued)

Figure Page

CHAPTER 1

INTRODUCTION

Stars in the solar neighborhood (i.e. within 500 pc of the Sun) have been actively studied for over a century. The eventual goal of these studies is to piece together the dynamic and chemical evolution of the Galactic disk. To this end, one of the principle approaches for probing the disk has been to study the so-called galactic (or open) clusters, broadly defined as gravitionally bound groups of hundreds to thousands of stars in the galactic disk. Clusters are valuable astrophysical tools as they contain stars across a range of stellar mass that have formed from a common gas cloud, and as such, share common distances, common ages and common initial chemical abundances.

With their common initial chemical compositions, open clusters make attractive targets for studying galactic chemical evolution (Bragaglia, 2008). Abundances in open clusters, particularly metallicities (denoted [Fe/H], a measure of heavy elements in a star), are used to answer a variety of questions of interest in studying galactic chemical evolution. For example, [Fe/H], which has been measured for multiple open clusters, has been used to describe the galactic metallicity gradient, chemical mixing of the galactic disk and to determine age-metallicity relations (Boesgaard & Friel, 1990).

The two broad classications for open clusters, young (< 1.0 Gyr) and old (≥ 1.0 Gyr), each offer distinct advantages and disadvantages in piecing together a history of the disk. Young open clusters are numerous, bright, nearby and therefore conducive to high resolution spectroscopic abundance studies. They appear to dynamically evaporate into the field relatively quickly (within 1.0 Gyr), making them useful for studying the dynamics in the disk, although their rapid dispersal limits their practical application in studying the long term history of the Galactic disk. Old open clusters (ages from 1-10 Gyr), in contrast to their young counterparts, are well suited to probing the entire history of the Galactic disk over its 10 Gyr age (Friel (1995), Bragaglia & Tosi (2006)). However, they see practical

limitations in that they are found in relatively low numbers and are prefentially located outside of the solar circle and away from the Galactic plane (Friel (1995)), an apparent effect of the need to avoid dissolution by the dynamical processes that are responsible for the efficient evaporation of younger clusters (i.e. interactions with giant molecular clouds Spitzer (1958)): they must either be formed outside of the disk or dynamically evolve there through some form of non-disruptive heating. Clearly open clusters, both young and old, are valuable targets in piecing together both a chemical and dynamical history of the Galaxy.

One of the greatest advantages in using open clusters to study the evolutionary history of the Galaxy lies in their being well understood stellar populations. This correlates with their being a direct observational manifestation of the so-called Russell-Vogt theorem, which states that a star's mass and internal composition uniquely determine its subsequent evolution (Kaehler, 1978). In this sense, open clusters provide a coeval group of stars with similar age, distance and composition, allowing for in depth investigations into the detailed physics underlying stellar evolution. In fact, open cluster studies are often used to constrain theoretical models of stellar evolution (i.e. mass tracks and isochrones). The underlying physics used in generating these models is so well constrained that open cluster studies are now being used to explore more specific aspects of stellar evolution. For example, deficiencies in the the treatment of light element depletion have been revealed through the study of lithium in young open clusters (King et al., 2000) Despite the deficiencies in the models, in general isochrones and mass tracks can be used to trace the evolutionary sequences of open clusters relatively well.

In this sense, the same models that are constrained by results from open cluster studies are used extensively in the study of the clusters themselves. The general approach is to plot observed luminosities and color indices for stars in a cluster in an observational HR diagram. Through an approach referred to as main sequence fitting, observed apparent magnitudes are transformed into absolute magnitudes through comparison with stellar mass tracks, and the distance to the cluster is determined, independent of the need for direct distance measurements. Furthermore, ages can be determined based on the evolutionary

sequence that an open cluster's members trace in the HR diagram. The concept for this age dating is simple: through stellar evolution models the main sequence lives of stars as a function of their mass is well constrained. Once the turnoff of a cluster is established, the highest mass stars that remain on the main sequence provide an estimate of the age of the cluster. Thus, open clusters are self-contained stellar populations whose distances and ages can be obtained by models of stellar evolution, that are constrained by studying the clusters themselves.

With the disk richly populated by both field stars and open clusters, and considering that clusters are relatively well studied, the logical step in piecing together a more complete picture of the chemical and dynamical history of the disk is to study field stars. In recent years, the advent of large surveys such as *HIPPARCOS* (Perryman & ESA, 1997) has yielded precise parallaxes for thousands of nearby field stars, and in doing so, provided the necessary tools for investigating the field. In particular, studies of the velocity distributions of disk field stars in the solar neighborhood have identified stellar overdensities in kinematic phase space (Skuljan et al., 1999). The potential application of these velocity structures, commonly referred to as moving groups, was first identified by Eggen (1958) who considered these assemblages to be relic structures of dissolved open clusters. In this paradigm, a moving group would essentially be a spatially unassociated open cluster, therefore it would possess the same characteristics that make open clusters such valuable astrophysical tools (common ages and common initial chemical abundances) and similar techniques that are useful for studying open clusters could be applied. With the availability of precise *HIPPARCOS* parallaxes for stars in many moving groups, member distances would be well constrained. Through HR diagrams of moving groups, ages for otherwise random, spatially isolated moving group stars could be determined in the same manner as used for open clusters. Moreover, by selecting samples from *HIPPARCOS*, the stars are all nearby and therefore can be subjected to one of the most rigorous analyses available to astronomers: high resolution spectroscopy.

As of the writing of this dissertation, relatively little work had been done to explore the reality of classical moving groups as dissolved open clusters and their use in chemically tagging the galactic disk, with two notable exceptions, the Ursa Major Group and the HR1614 Moving Group. Soderblom & Mayor (1993) examined the Ursa Major moving group and utilized age information inferred from chromospheric emission to constrain group membership in UMa, assuming a classical open cluster dissolution origin for group members. While this study did not utilize chemical tagging to constrain group membership, it did illustrate the viability of moving groups representing dissolved populations of open clusters. King et al. (2003) and King & Schuler (2005) revisited the membership of the UMa group, using new and extant abundances. They used the results to constrain membership in the UMa group, showed the members to be chemically homogeneous, and noticed overexcitation/overionization effects in the cooler field star members of the group, similar to those observed in young ($<$ 500 Myr) cool open cluster dwarfs (Schuler et al. (2003), Schuler et al. (2004)). The first in depth application of chemical tagging to constrain moving group membership was by De Silva et al. (2007), who derived abundances for various elements for the HR 1614 moving group. They found that for their 18 star sample, 14 stars were metal-rich ([Fe/H] $\geq$ 0.25 dex with σ=0.03) leading to the conclusion that the HR 1614 moving group, which shared distinct kinematics and distinctly super-solar chemical abundances, was a remnant of a dissolved open cluster.

Considering the evidence for moving groups as disk field relics of dissolved open clusters, and the value of confirming the reality of such moving groups for tracing galactic chemical and dynamic evolution and allowing age dating of seemingly random field star populations, this dissertation establishes an approach for chemically tagging a distinct kinematically defined moving group. The goals of this dissertation will be to:

1) Examine a distinct kinematic structure of apparent field stars in the Galactic disk and use high resolution stellar spectroscopy to determine if it is monolithic in chemical abundance and/or age.

2) If the structure is not distinct in abundance and/or age, determine if there is a dominant

uniform subsample in age or abundance.

3) Explore dynamical effects using NBODY simulations to complement the observational results.

A basic framework for open cluster formation and dissolution into the field is now presented. This discussion can be skimmed for readers who are interested in the direct results of this dissertation work, but it provides useful details that are alluded to in the analysis of the results.

1.1 Embedded Clusters

1.1.1 Embedded Clusters in Giant Molecular Clouds

The canonical picture of star formation holds that most open clusters form due to fragmentation and gravitational collapse in giant molecular clouds (hereafter GMCs) (Stahler & Palla, 2005). The GMCs are predominantly composed of molecular hydrogen (H_2) with individual cloud masses of order 10^5 $M_\odot$. Star formation within this molecular gas appears to occur in clusters rather than in isolation. In fact 70-90 % of star formation occurs in embedded clusters (Lada et al. (1991), Lada et al. (1993), Carpenter et al. (1995), Phelps & Lada (1997)). Physically, embedded clusters are associated with only the most massive and dense cores of GMCs, characterized by masses of 100-1000 M⊙ and diameters of 0.5-1 pc (Lada & Lada, 2003). The primary difficulty with understanding the evolution of embedded clusters lies in their obscuration within dense molecular gas which efficiently extincts the optical light, necessitating use of infrared facilities.

1.1.2 Embedded Clusters Versus Open Clusters

While the processes by which embedded clusters evolve into currently observed open clusters are only rudimentarily understood, some general comparisons between embedded clusters and open clusters can be drawn.

The mass distributions of embedded clusters and open clusters, in some cases, appear to be similar. The typical mass spectrum within dense embedded cluster cores can be described by a power law function $\frac{dN}{dM} \propto M^\alpha$, where α=-1.6 to -1.7 (Lada et al. (1991),

King et al. (1998)). Power law indices for open cluster mass distributions (Elmegreen & Efremov (1997), van den Bergh & Lafontaine (1984)) appear to be very similar with α=-1.5 to -2.0. The most recent evaluation of mass distributions of open clusters, from Piskunov et al. (2008), derives a two-component distribution for open clusters based on a large, homogeneously analyzed sample of 650 open clusters in the solar neighborhood. Their power law distribution for high mass clusters ($M_C > 2.3\times10^3$ $M_\odot$) finds α=-1.66, in near perfect agreement with the embedded cluster α=-1.6 to -1.7. This would suggest that higher mass open clusters can emerge from their molecular clouds relatively unscathed by global dynamic effects.

Open clusters emerging from their embedded stages unscathed, however, is not necessarily common. Using a sample of 53 embedded clusters within 2.0 kpc of the Sun, Lada & Lada (2003) estimate that the birthrate of embedded clusters in the solar neighborhood is between 2-4 clusters per Myr per kpc^2, a factor of 10 higher than the 0.4 clusters per Myr per kpc^2 birthrate estimated for open clusters (Piskunov et al., 2008), which suggests that not all embedded clusters emerge to become open clusters. This is consistent with numerical simulations that find 10-80 % of embedded cluster stars are ejected (Lada & Lada, 2003) in the $\sim$ 10 Myrs that it takes stellar winds of massive O-type stars (Whitworth, 1979) or shocks from nearby supernovae to disperse the gas which shrouds embedded clusters. Taking into account that there is signficant uncertainty in how much stellar mass is typically ejected, an average open cluster observed today is believed to have emerged from a progenitor embedded cluster with a mass at least as great as $M_{EC} \approx 500$ $M_\odot$ (Lada & Lada, 2003). Furthermore, an open cluster which emerges from an embedded cluster must be tightly bound in order to survive primordial dispersal by the high winds and supernovae shocks responsible for gas dispersal. Ongoing studies of embedded cluster cores and their evolution into open clusters will provide a much more detailed picture of the processes by which open clusters are born.

1.2 Open Clusters

1.2.1 Cluster Mass Functions

According to the rough constraints inferred from a basic understanding of embedded clusters, it appears that open clusters which have emerged from their parent molecular clouds represent a lower limit of ∼10% of the total mass of the galactic disk (Adams & Myers, 2001). Open cluster studies, however, can better constrain the mass contribution that clusters may make to the galactic disk. Piskunov et al. (2008) utilized a sample of 440 clusters to derive a two segment cluster initial mass function (CIMF= $\zeta(m)$) for open clusters. From their sample they derive a CIMF:

$$\zeta(m) = \frac{k}{2.3\times10^3 M_\odot}\left(\frac{M_c}{2.3\times10^3 M_\odot}\right)^\alpha$$

$$\text{where } \alpha = -0.82 \pm 0.14 \text{ for } M_c < 2.3\times10^3 M_\odot$$

$$\text{and } \alpha = -1.66 \pm 0.14 \text{ for } M_c > 2.3\times10^3 M_\odot$$

and k=0.24 to appropriately normalize the function.

For the higher mass range, this is in good agreement with the embedded cluster mass function power law of $\alpha = -1.6$, suggesting again that higher mass open clusters survive mass ejection to retain their embedded mass distributions (Lada et al., 1993).

In utilizing this CIMF, Piskunov et al. (2008) also determine a cluster formation rate for the solar neighborhood and determine an estimate of the surface density of Galactic disk stars that have passed through an open cluster phase. By integrating their CIMF over mass ranges for observed open clusters (M_{low}=50 $M_\odot$ and M_{high}=3×10^5 $M_\odot$ from their Figure 5), they find an average initial mass for a forming cluster $<M>_C^{CIMF}$=4.5×10^{3}M$_\odot$. The surface density of stars in the galactic disk (Σ) that have passed through an open cluster phase of evolution can then be estimated by multiplying the rate at which clusters form per unit area times the age of the galactic disk times the typical initial mass of a forming cluster $\Sigma = vTM_C^{CIMF}$ where v=0.4 kpc^{-2}Myr^{-1} (formation rate of clusters in the solar neighborhood), T=13 Gyr (the age of the Galactic disk) and M_C^{CIMF}=4.5×10^3 $M_\odot$.

With the above parameters, they derive a surface density for stars that have been through an open cluster phase: Σ=22$M_\odot$ pc^{-2}. Using a more realistic age for the galactic

disk of 10 Gyr, this surface density is: Σ=18$M_{\odot}$ pc^{-2}. Both results are consistent with the embedded cluster results of Lada & Lada (2003), who found Σ=10-30 M$_{\odot}$ pc^{-2}. To obtain an estimate of the total contribution of open clusters to the mass of the galactic disk, this surface density can be compared to the results of Holmberg & Flynn (2004) who utilized Hipparcos K giants in the solar neighborhood to estimate the total surface density of all mass in the galactic disk to be 56 $\pm$ 6 M$_{\odot}$pc^{-2}, $\sim$ 10 M$_{\odot}$ higher than the estimates of Kuijken & Gilmore (1989). This comparison leads to an estimate of $\sim$40 % of the stars of the galactic disk passing through an open cluster phase, significantly greater than the lower limit of 10% estimated by Lada & Lada (2003). Therefore, stars which have spent time in an open cluster phase of evolution represent between 10 and 40 % of the total mass of the galactic disk.

1.2.2 Physical, Spatial and Kinematic Properties

From an expanded cluster sample utilized to derive their cluster mass functions, Piskunov et al. (2008) recently derived a consistent set of masses and radii for a set of 650 open clusters in the solar neighborhood. They utilize the classical King parameters r$_c$, r$_t$ and k (where r$_c$ is the core radius, r$_t$ is the tidal radius and k is a normalization factor) (King, 1966), to produce density profiles which analytically describe observed open clusters. In deriving spatial descriptions, the core radius is the radius where the stellar brightness in the cluster has dropped to half of its total value and the tidal radius is an estimate of the radius cutoff, outside of which there are no cluster members. Average core radii for their entire sample appear to be $\sim$1.5 pc with an accuracy of 15-50% while tidal radii appear to be 7-10 pc with an accuracy of 20%. In Figure 1.1 both the tidal radius (top) and core radius (bottom) for the cluster sample of (Piskunov et al., 2008) are plotted versus cluster age. Typical tidal radii appear to be of order 5-20 pc, while the core radius varies from 1-10 pc. The radii and ages shown have all been derived by Piskunov et al. (2008) and therefore are a consistent set of masses and radii for a large sample of nearby open clusters.

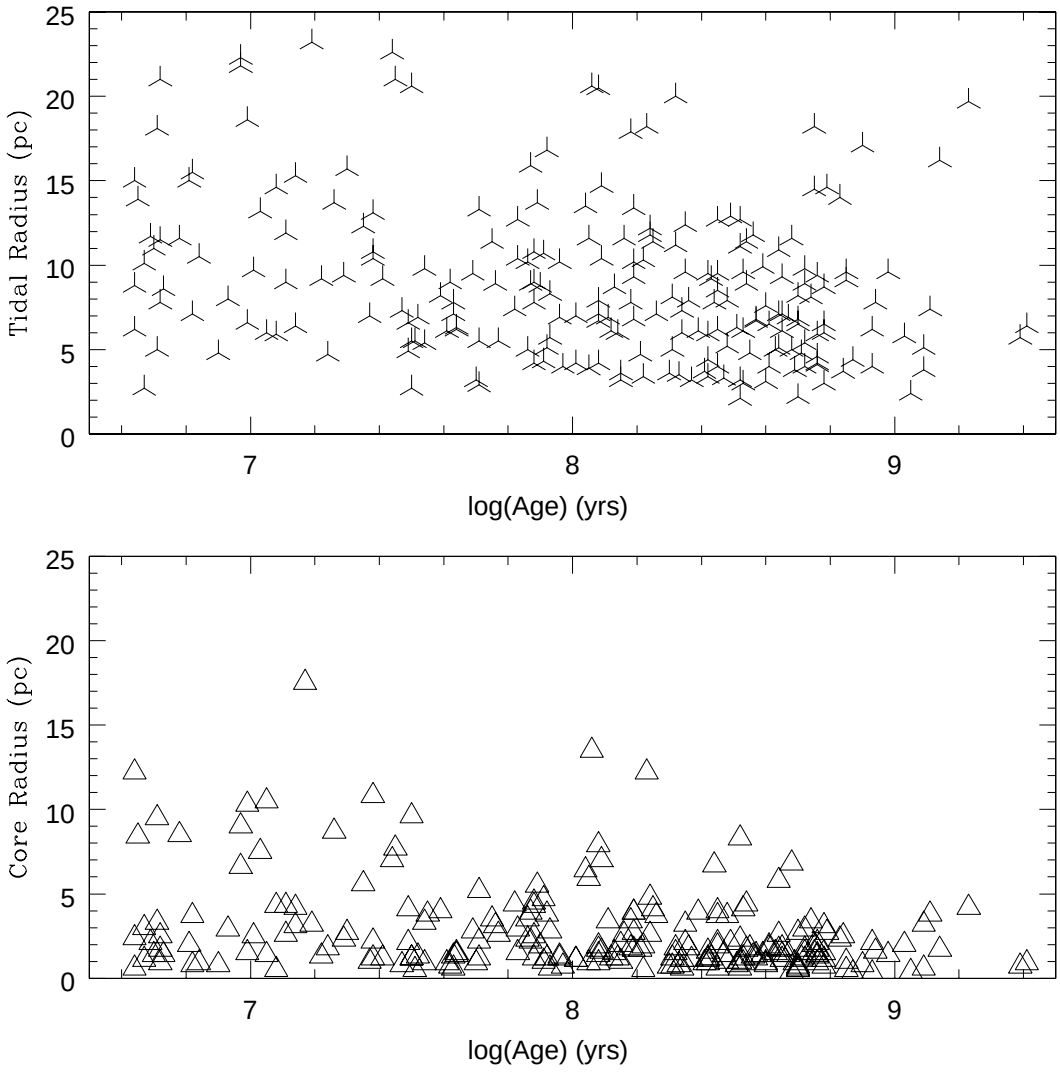

Figure 1.1 Tidal radii (top) and core radii (bottom) versus ages for a sample of 236 open clusters from Piskunov et al. (2008). The tidal radius varies from ∼5-20 pc while the core radius varies from 1-10 pc.

Kinematics of open clusters provide another essential piece of the puzzle when describing an open cluster, particularly when constraining membership. If a star is a gravitationally bound member of a cluster, then its radial velocity must be characteristic of the overall center of mass cluster velocity. In fact, this is one of the limiting factors used to constrain open cluster membership. Accurate radial velocity measurements are available for many of the most well studied open clusters. A sample of radial velocity dispersions across multiple open clusters of varying age are presented in Table 1.1. Notice the low dispersion in velocities that appears to characterize open clusters across multiple age ranges. The canonically quoted velocity dispersion for open cluster members of ~ 1 kms^{-1} is consistent with Table 1.1 and will be assumed as a good approximation for typical open clusters.

Table 1.1

Open Cluster Velocity Dispersions

Cluster Name	Velocity Dispersion kms^{-1}
Hyades	2.85
Praesepe	0.79
Coma Ber	0.44
Pleiades	1.02
Alpha Persei	1.08
NGC 752	1.05
NGC 2682	0.71
NGC 6475	1.33
NGC 7092	1.20
IC 2391	0.55
IC 2602	0.90
Blanco 1	0.82

1.2.3 Chemical Homogeneity of Open Clusters

One of the most valuable characteristics of open clusters is the conventional assumption that they are relatively homogeneous. Support for this homogeneity can be seen in multiple open cluster metallicity studies. For example, Paulson et al. (2003) determined

the Hyades to be a chemically homogeneous open cluster (<[Fe/H]>=0.13 with σ=0.05) using KECK HiRES spectra of 55 F-K type dwarfs, for which they derived differential abundances for Fe and various α elements. This homogeneity was later examined by De Silva et al. (2006) who extended the uniformity of the Hyades to heavier neutron capture elements (Zr, Ba, La, Ce and Nd, with a maximum σ=0.05 dex) for a subsample of the stars observed by Paulson et al. (2003). In order to place this homogeneity in context with what is presented in this dissertation, a sample of Hyades stars with [Fe/H] and respective uncertainties has been taken from Schuler et al. (2006). This reference was used as the abundances have been derived using a similar approach as utilized herein and uncertainties for both [Fe/H] and [Ni/H] are quoted. In analyzing their data, smoothed histograms were created of the [Fe/H] and [Ni/H]. These histograms are described in more detail in chapter 3, but to summarize, each metallicity is smoothed into a gaussian distribution and these distributions are summed to yield a smooth histogram. Examining 1.2 the dotted line shows the [Fe/H] distribution while the solid line shows the [Ni/H] distribution. They histograms are nearly gaussian with the possibility of an enhanced metallicity tail, i.e. asymmetry skewed towards higher abundances. The salient point, however, is that the metallicity distributions, including respective uncertainties, do not show indications of chemically deviant members. Stars with discrepant metallicities should clearly show up as bumps in [Fe/H] distributions done in this manner, as demonstrated in chapter 3. As a quantitative estimate of the homogeneity of the sample, a reduced chi-squared statistic has been calculated for the Hyades sample. The result, χ^2_ν=1.303, will be utilized as a rough value for describing a sample as homogeneous.

1.2.4 Evolution of Open Clusters

The estimates of Piskunov et al. (2008) suggested that 40 % of galactic disk stars have spent time in open cluster stages. This, however, does not imply that the stars are **currently** residing in clusters. Observationally, this can be inferred from the age distribution of open clusters (Figure 1.3). Approximately 66 % of observed open clusters

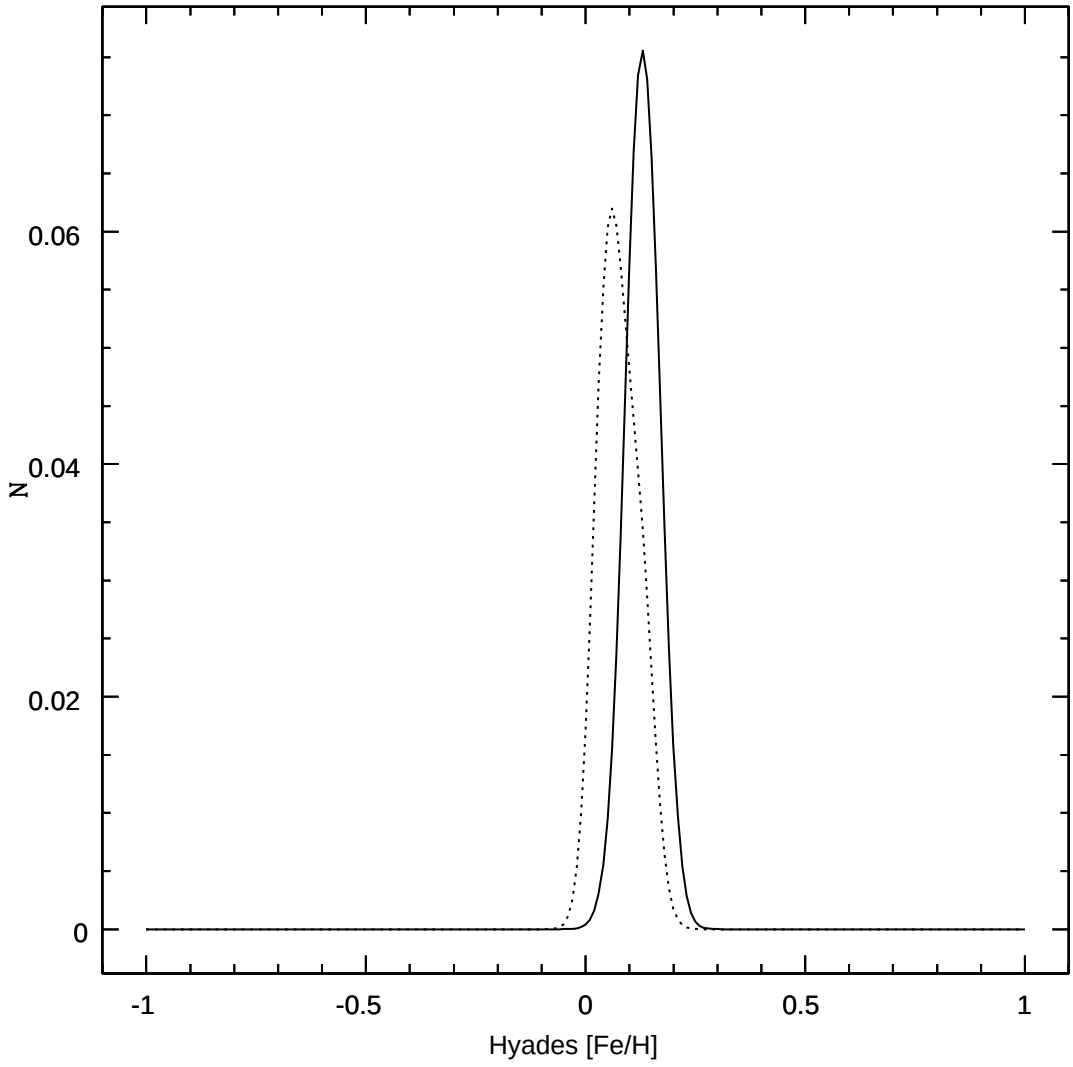

Figure 1.2 A smoothed metallicity distribution for the Hyades is presented. Data are taken from Schuler et al. (2006) for [Fe I/H] (dotted) and [Ni/H] (solid). Notice that both distributions are smooth. The lack of "bumps" in the distributions are suggestive that no stars are extremely chemically deviant, while the shift in peak metallicity in Ni is indicative of a slight enhancement in overall Nickel abundance for the sample.

are younger than 250 Myr and $\sim$ 95 % of open clusters are younger than 1 Gyr. Assuming continuous star formation, when compared to the 8-10 Gyr age of the galactic disk, open clusters appear to evaporate relatively quickly.

1.2.5 Open Cluster Evaporation

The lower mass stars of open clusters are the first victims of dispersal into the galactic field. This is theoretically expected from the view of mass segregation, whereby as a cluster evolves over several relaxation timescales (described below) the higher mass stars settle to a dense core, while the lower mass members disperse into an outer corona of stars. Indeed, mass segregation is both predicted by simulations (Spitzer & Shull, 1975) and observed in a magnitude limited sample of young open clusters (Schilbach et al., 2006).

Dispersal of cluster members into the field can occur through a variety of mechanisms, including internal stellar encounters, interactions with the Galactic tidal field, and shredding by passing Giant Molecular Clouds.

In the following discussion, for simplicity assume an average open cluster is composed of 500 stars, each of 1 $M_{\odot}$, distributed in a constant density sphere of radius 10 pc and internal velocity dispersion of 1 kms^{-1}. For this stellar system, when in virial equilibrium the typical evaporation time due to internal star-to-star interactions is: $\tau_{ev} \sim 100\tau_{relax}$ (Binney & Tremaine, 1987), where the relaxation time is:

$$\tau_{relax} \sim \frac{0.1N_*}{ln(N_*)}) * \tau_{cross}$$

$$\tau_{cross} \sim \frac{R}{v},$$

where R is the tidal radius for the cluster and v is the velocity of a star, relative to the mean velocity of all stars in the cluster. Evaporation of an average open cluster as described above solely through these internal stellar encounters would take of order 8.0 Gyr. This suggests that additional mechanisms are responsible for their evaporation.

Open clusters are also subjected to tidal forces from the potential of the galactic disk. NBody simulations of the extent of these tidal forces on disruption timescales of open clusters suggest that the disruption times for an open cluster in a representative Milky-Way

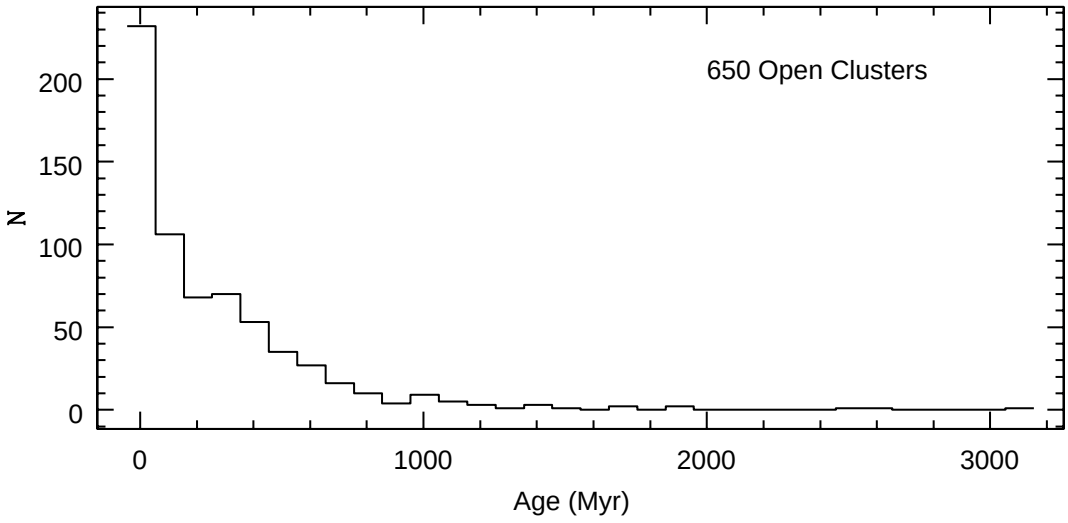

Figure 1.3 Histogram of the ages for 650 Open Clusters in the solar neighborhood from Piskunov et al. (2007). Approximately 66 % of open clusters appear to be younger than 200 Myr, suggesting that clusters evaporate on relatively short timescales.

disk potential can be analytically described by a power law function of the initial cluster mass. According to Lamers et al. (2005), the disruption timescale due to the galactic potential for a cluster in the Milky Way disk is:

$$\tau_{dis} \propto 6.9 * (\frac{M_C}{10^4 M_\odot})^{0.62} \text{ Gyr.}$$

For an average cluster mass of M_C=500 $M_\odot$ the dispersal timescale as a result of tidal forces of the galactic potential would be $\tau_{disp} \sim 1$ Gyr, still too low to explain the dearth of open clusters older than ∼250 Myr.

Historically, the inability of internal stellar encounters and tidal field dissolution to rapidly disperse a cluster led to studies of the shredding of a cluster by interactions with large structures in the galactic disk (Spitzer, 1958). The most likely candidates for these large structures are, ironically, the same structures that give birth to clusters: giant molecular clouds (Wielen, 1985). The most recent examination of the dynamics of dissolution of an open cluster by a passing GMC (Gieles et al., 2006) found that interactions with GMCs can evaporate an open cluster according to a power-law expression as a function of initial cluster mass. Their equation 24 for the solar neighborhood (where the density of GMCs in the solar neighborhood is taken to be ρ=0.03 $M_\odot pc^{-3}$, the surface density of an individual GMC is σ_n=170 $M_\odot pc^{-2}$ and cluster/cloud velocity dispersion is σ_v=10 kms^{-1}) determines a cluster dispersal timescale (where complete dispersal means stellar density of a cluster becomes indistinguishable from the density of field stars) induced by a passing GMC is:

$$\tau \propto 2.0 * \frac{M}{10^4 M_\odot} * (\frac{3.75pc}{r_h})^3 \text{ Gyr,}$$

where r_h is the radius which contains half of the mass of the cluster. For the homogeneous sphere of 500 stars described above, the half radius is ∼7.75 pc and an interaction with a GMC can dissolve an open cluster in ∼ 10 Myr.

A combination of these three dispersal mechanisms; evaporation from internal stellar encounters, stripping from the tidal field of the galactic potential and shredding by interaction with a passing GMC, results in the evaporation of an open cluster into spatial densities that are indistinguishable from the field (of order 1 $M_\odot pc^{-3}$ (Stahler & Palla, 2005)), on

timescales that are reasonably consistent with observations. Neglecting the drastic shredding of a cluster by interaction with a giant molecular cloud, the remaining mechanisms for dispersing a cluster are not particularly violent. Consequently, the ejected stars of an open cluster can, potentially, retain their common velocity dispersions and be associated with other dispersed cluster members through these common velocities, as explored in chapter 4. The groups of stars that reside in common velocity structures, without spatial association, have come to be known as moving groups.

1.3 Moving Groups

The development thus far leads to the classical formulation of Eggen (1958): that open clusters gradually dissolve into the galactic disk and evaporated members retain common kinematics to become moving groups. Indeed, studies of kinematics of stars in the solar neighborhood reveal many distinct velocity structures and substructures of stars moving through space with common velocities (Skuljan et al., 1999). The larger structures can be associated with well established stellar streams which are unlikely to share a common origin as a dispersed open cluster. Antoja et al. (2008) examined similar velocity streams to those identified by (Skuljan et al., 1999) in a study of kinematics of ∼14000 F through K stars in the solar neighborhood obtained from Nordström et al. (2004). Using isochrone ages and metallicities derived from *uvby-β* photometry, they found that the branches were composed of stars with varying metallicity and age, suggesting the branch members did not have a common origin. Their final conclusions were that the branches had a dynamic origin, the nature of which would be explored in future work that has yet to be published. Occasionally, this result is quoted to refute the classical picture of moving groups. This would seem to be premature considering that both Antoja et al. (2008) and Skuljan et al. (1999) found that the smaller structures and substructures in their studies could be associated with many of the classical moving groups proposed by Eggen. It is these smaller kinematic substructures that are the most likely targets for being moving groups that are dissolved remnants of open clusters.

In order to explore the reality of moving groups being dissolved stellar aggregates, in this dissertation a moving group will be defined by the following characterisitics, following the work of Soderblom & Mayor (1993).

(1) The stars of a moving group must have similar UVW space motions, with particular emphasis on the V velocity. Since the V motion defines the direction of travel for a group orbiting the Galaxy, it has historically been the distinguishing velocity for classical moving groups, a convention that will be maintained in this work.

(2) Stars in a moving group, when placed in a Hertzsprung-Russell Diagram, trace out a distinct evolutionary sequence, consistent with members sharing a single age and composition. This is an essential characteristic for a moving group to possess if it is a dissolved open cluster.

(3) Stars in a moving group must share common chemical signatures, as determined through chemical tagging. Again, this requirement assumes that a moving group, being a relic of an open cluster, maintains similar homogeneity as that currently observed in open clusters.

A potentially powerful and rigorous test for determining if members of a moving group represent Eggen's formulation of a moving group as a dissolved relic of an open cluster is to examine chemical abundances of alleged members. By establishing a chemical abundance trend for a moving group, members can be chemically constrained as bona-fide members of a stellar aggregate. This technique, dubbed chemical tagging, has only been applied (in regards to moving groups) to an 18 star subsample of the HR 1614 moving group. Results from this study suggest that it is, in fact, a relic structure of a dissolved cluster, with 14 members showing homogeneous abundances comparable to those observed in open clusters (De Silva et al., 2007). In fact, the chemically homogeneous stars of their sample can be seen to trace out a clear main sequence with an approximate isochrone age of 2 Gyr (Figure 7 of De Silva et al. (2007)). Unfortunately, their sample included only dwarf stars, so a complete tracing of the evolutionary sequence with varying mass was not possible. Nevertheless, their results are promising. If a similar chemical tagging approach can be effectively applied to additional kinematically linked groups of stars to reveal chemically

distinct samples which appear to trace a clear evolutionary sequence, then the standard evolutionary models used for age dating open cluster members can be used to determine ages in seemingly random field stars!

This work aims to apply the approach of chemical tagging to a sample of dwarf and giant stars that have previously been identified as members of the classical Wolf 630 Moving Group of Olin Eggen (Eggen, 1958). From this sample of stars, an approach will be developed to extract a chemically homogeneous subsample that represents a common evolutionary sequence of a single age and chemical composition. Furthermore, considering that this dissertation aims to describe a moving group as a dissolved open cluster, simple NBODY simulations will be conducted to explore how moving groups might form and evolve.

CHAPTER 2

WOLF 630

2.1 History of Wolf 630

The first identification of the Wolf 630 moving group was made in 1965 by Olin Eggen (Eggen, 1965). He noted that several K and M dwarfs and giants in the solar neighborhood appeared to have similar space motions to that of the multiple star system Wolf 630 ((U,V,W)=(23, -33, 18) kms^{-1}). These kinematics, distinctive of membership in an old disk population, also placed the stars in a relatively sparsely populated region of kinematic phase space (Eggen, 1969). Eggen also noted that the color magnitude diagram for the K and M dwarfs and giants with common kinematics to those of Wolf 630 appeared to trace an evolutionary sequence similar to the M67 open cluster. In this sense, the old disk membership suggested by the kinematics and the evolutionary sequence being similar to the 5-6 Gyr cluster, M67, seemed consistent with the Wolf 630 group being composed of an old population of stars. Although his sources are not completely transparent, at least some of the distances in this study were determined from trigonometric parallaxes (17 of 54 stars), with the remainder coming from "luminosity estimates of many kinds". As a rudimentary form of chemical tagging, Eggen (1970) tested the metal abundances of 23 Wolf 630 group members through *uvby-β* photometry. Chemical homogeneity for group members was judged by variations in $\delta[m_1]$=(v-b)-(b-y), a metallicity sensitive photometric index, that were found to be comparable with variations in the Hyades, Praesepe, and the Coma Berenices clusters.

Relatively little work was done following this, until Tuominen and Vilhu studied the chemical composition of five field giant stars that were alleged members of Wolf 630 (Tuominen & Vilhu, 1979). As described in Vilhu et al. (1978), they utilized coudé spectra from the 2.6 m telescope of the Crimean Astrophysical Observatory which yielded spectra with a dispersion of 6 $Åmm^{-1}$. Using a curve of growth approach, they determined metallicities

from equivalent widths and found that three stars appeared to be chemically homogeneous. The average metallicity ([Fe/H]) for their homogeneous sub-sample of 3 stars suggested an overall metallicity for Wolf 630 of [Fe/H]$\sim$+0.23. However, it must be noted that their analysis was not done with respect to the Sun. Their metallicities are quoted with respect to a standard star of solar metallicity, so while they derived a metallicity of 0.00 for their reference star (i.e. solar metallicity), literature determinations suggest their standard star metallicity is -0.08. This would lower the average metallicity for the group to [Fe/H]$\sim$ 0.15.

McDonald & Hearnshaw (1983) revisited the collective membership of the Wolf 630 moving group by comparing scatter in the color-absolute magnitude diagram for stars assigned to Wolf 630 with the intrinsic scatter observed for the old ($\sim$5 Gyr) open cluster M67, previously noted by Eggen as tracing a similar sequence to that of the Wolf 630 group. They attempted to recreate the approach presumably utilized by Eggen to find his original Wolf sample (Eggen, 1965). In summary, they defined a group velocity of V_G=-32.8 $\pm$ 1.3 kms^{-1}, the V velocity which characterizes Wolf 630. Then, they utilized standard trigonometric formulae to calculate the V motion for each possible group member, based on proper motions and radial velocities. The final absolute magnitudes they report were found by determining the parallax necessary for the calculated V motion to be equal to the group velocity. Typical uncertainties for absolute magnitudes calculated in this manner appear to be between 0.2-0.4 magnitudes, larger than magnitude uncertainties obtainable with precise parallax information currently available from Hipparcos. With absolute magnitudes, they created a color-magnitude diagram for their chosen Wolf sample and compared the scatter of apparent members with the observed scatter in M67. Their conclusions were that either (1) the intrinsic scatter in the Wolf 630 moving group color-magnitude diagram was greater than that of M67, or (2) the errors in radial velocities and/or proper motions they utilized must have been underestimated by a factor of 2.4 or (3) many of the stars in their sample were, in fact, non-members. Unfortunately, the radial velocities and parallaxes that they used are not given; thus their uncertainties cannot be compared with new, high quality

Hipparcos parallaxes and radial velocities from CORAVEL, which limits the tests, making use of updated data, that can be performed on their conclusions.

Taylor (1994) examined metallicities from "published values of [Fe/H] from diverse papers" of 40 members of the Wolf 630 group. His sample composes 26 % of Eggen's original samples (Eggen, 1969). He concluded that metallicity dispersions within his sample were too great for meaningful conclusions about the existence or non-existence of a genuine, chemically distinct Wolf 630 moving group. This suggests the need to obtain high quality [Fe/H] determinations with minimal uncertainties in testing for chemical uniqueness in the Wolf 630 group.

Since the work of Taylor (1994) no targeted attempts have been made to determine the true nature of the candidate Wolf 630 moving group. However, the velocity distribution study of Skuljan et al. (1999) suggested a possible rediscovery of the group. In their study, Skuljan et al. derive velocity contours for a sample of over 4500 early and late-type stars in the solar neighborhood with available Hipparcos parallaxes and radial velocities. In their figure 10 they present UV velocity contours for 3561 late type dwarfs in the solar neighborhood. There is a clear overdensity of stars near the position of Wolf 630. Furthermore, this structure appears to be distinctly separated from any other known moving groups or stellar streams. This provides compelling evidence that Wolf 630 is a real kinematic structure. The question of if the structure has a common origin and chemical history will be addressed in this dissertation.

Despite the distinct kinematic structure exhibited by the Wolf 630 moving group when examined with updated Hipparcos parallaxes, it has not been specifically targeted in a study which makes use of the most modern data. This is remedied in this dissertation, where accurate parallaxes and photometry from the updated *HIPPARCOS* data reduction (van Leeuwen, 2007) coupled with high precision radial velocities from CORAVEL (Nordström et al. (2004) and references therein) allow for developing a Wolf 630 sample with internally consistent distances and magnitudes, thereby removing the uncertainties faced by McDonald & Hearnshaw (1983). Furthermore, a single high resolution spectroscopic study of Wolf 630

moving group members will allow for derivation of a sole source and an internally consistent set of metallicites with low internal uncertainty to test chemical homogeneity in the group, removing the largest source of uncertainty from Taylor (1994).

2.2 The Stellar Sample

2.2.1 Literature Parameters

The 34 stars in this sample were previously identified as members of the Wolf 630 group (Eggen (1969), McDonald & Hearnshaw (1983)) according to UVW kinematics. Updated parallaxes and proper motions were taken from the latest reduction of Hipparcos data (van Leeuwen, 2007). Visible band photometry (B, V, B_{Tycho}, V_{Tycho}) was taken from the *HIPPARCOS* catalogue (Perryman & ESA, 1997). Near infrared J, H and K photometry was taken from (Cutri et al., 2003). Precision Coravel radial velocities were taken from the compilation of Nordström et al. (2004).

2.2.2 Kinematics

Galactic UVW kinematics have been determined from proper motions, parallaxes and radial velocities using a modified version of the code of Johnson & Soderblom (1987). In this code, the U velocity is positive towards the Galactic center, the V velocity is positive in the direction of Galactic rotation and the W velocity is positive in the direction of the North Galactic Pole (NGP). The kinematics are plotted in the UV kinematic plane (Figure 2.1) and the relevant parameters for determination of these kinematics are presented in Table 2.1. The two plots show the same information. The left plot is a zoomed in view of the kinematics, while the right plot shows the velocity structure on the same scale as that of Skuljan et al. (1999). Note that the slight tilt in the UV plane is characteristic of many streams and moving groups detected by Skuljan et al. (1999).

Table 2.1

Kinematic Infomation

HIP	π	PM RA	PM DEC	Radial Velocity	U	V	W
	mas	mas/yr	mas/yr	kms^{-1}	kms^{-1}	kms^{-1}	kms^{-1}
102531	31.69± 2.37	-6.1 ± -6.1	-201.74 ± 1.84	-7 ± 0.9	16.56 ± 1.57	-22.08 ± 1.44	-14.1 ± 1.28
102532	32.14± 1.19	-25.88 ± -25.88	-196.27 ± 0.8	-6.5 ± 0.9	17.81 ± 0.88	-21.22 ± 0.96	-11.3 ± 0.57
103983	15.7 ± 1.29	-71.25 ± -71.25	-155.22 ± 0.56	-6.8 ± 2.0	35.19 ± 3.38	-38.12 ± 3.09	-3.79 ± 1.13
104521	28.38± 0.9	49.07 ± 49.07	-151.85 ± 0.64	-17 ± 0.9	1.21 ± 0.51	-29.00 ± 0.87	-12.52 ± 0.74
105341	61.04± 1.31	-173.35 ± -173.35	-721.75 ± 0.72	21.1 ± 2.0	38.89 ± 1.41	-43.87 ± 1.34	-18.2 ± 1.33
11033	6.47 ± 0.87	9.02 ± 9.02	-58.12 ± 0.57	-3 ± 5.0	23.42 ± 3.57	-36.19 ± 4.94	-2.86 ± 4.67
112222	24.86± 0.93	9.8 ± 9.8	-171.17 ± 1.25	-2 ± 5.0	15.10 ± 0.92	-22.12 ± 3.77	-18.86 ± 3.37
112447	61.54± 0.77	233.06 ± 233.06	-492.04 ± 0.61	-5.3 ± 0.9	3.90 ± 0.13	-31.59 ± 0.76	-27.82 ± 0.70
113622	5.96 ± 0.8	5.06 ± 5.06	-83.58 ± 0.75	19.1 ± 2.0	32.03 ± 4.04	-36.73 ± 6.68	-49.26 ± 4.93
114155	6.07 ± 0.67	0.26 ± 0.26	-33.31 ± 0.49	-26.8± 0.9	14.86 ± 1.47	-33.80 ± 1.46	-5.64 ± 2.25
114924	49.31± 0.58	111.7 ± 111.7	-236.29 ± 0.44	-25.3± 2.0	7.40 ± 0.64	-27.26 ± 1.88	-21.76 ± 0.38
1170	6.62 ± 0.82	-27.15 ± -27.15	-73.78 ± 0.41	-22.5 ± 0.9	41.77 ± 5.35	-40.49 ± 4.49	17.07 ± 1.08
12784	7.89 ± 0.92	36.53 ± 36.53	-35.79 ± 0.7	-31.9 ± 2.0	15.61 ± 1.78	-38.96 ± 3.51	14.14 ± 1.42
13064	4.07 ± 0.9	-2.07 ± -2.07	-48.35 ± 0.77	-14 ± 5.0	42.76 ± 8.33	-39.03 ± 8.99	-4.67 ± 5.68
13701	24.49 ± 0.72	77.73 ± 77.73	-219.99 ± 0.63	-20.3 ± 0.9	27.22 ± 0.70	-40.27 ± 1.23	9.47 ± 0.77
14501	31.76± 0.91	-7.99 ± -7.99	-260.71 ± 0.9	12.3 ± 2.0	18.55 ± 1.30	-29.59 ± 0.87	-21.15 ± 1.68
17792	4.61 ± 1.01	72.36 ± 72.36	10.28 ± 0.89	-78.6 ± 2.0	29.99 ± 7.98	-42.54 ± 9.01	95.48 ± 11.5
23852	35.34± 0.82	-5.61 ± -5.61	-382.35 ± 0.57	-23.8 ± 2.0	39.46 ± 1.91	-35.45 ± 1.01	-19.6 ± 0.89
29525	55.2 ± 0.96	78.11 ± 78.11	-297.1 ± 0.77	3 ± 5.0	5.92 ± 4.72	-25.07 ± 1.69	-6.43 ± 0.34
29843	25.06± 0.68	127.42 ± 127.42	-258.64 ± 0.5	-4.3 ± 2.0	43.74 ± 1.66	-32.57 ± 1.76	4.43 ± 0.61
32064	8.63 ± 0.77	34.99 ± 34.99	-46.05 ± 0.6	0.9 ± 0.9	18.91 ± 1.89	-24.89 ± 2.26	5.75 ± 0.67
33671	21.26± 0.74	0.6 ± 0.6	-124.13 ± 0.83	18 ± 2.0	14.39 ± 1.26	-25.74 ± 1.75	-14.85 ± 0.57
34440	10.68± 0.82	-5.02 ± -5.02	-103.52 ± 0.53	-17 ± 2.0	26.00 ± 2.01	-33.60 ± 3.11	-24.5 ± 1.71
3455	15.54 ± 0.82	-6.96 ± -6.96	-113.88 ± 0.6	0.6 ± 0.9	19.66 ± 1.07	-26.78 ± 1.45	-10.4 ± 1.01
34909	4.66 ± 0.9	14.66 ± 14.66	-41.8 ± 0.57	-9.2 ± 0.9	23.44 ± 3.03	-39.06 ± 8.19	-6.32 ± 1.20

Table 2.1 – Continued

HIP	π	PM RA	PM DEC	Radial Velocity	U	V	W
mas	mas/yr	mas/yr	kms^{-1}	kms^{-1}	kms^{-1}	kms^{-1}	
3559	31.39 ± 1.03	-32.25 ± -32.25	-205.68 ± 0.59	-12.8 ± 2.0	21.86 ± 0.72	-25.68 ± 0.89	3.84 ± 1.94
36732	11.15± 0.7	24.1 ± 24.1	-70.23 ± 0.51	16.4 ± 2.0	16.00 ± 1.98	-31.30 ± 1.99	-5.46 ± 0.40
36962	13.57± 0.87	-39.58 ± -39.58	-108.08 ± 1.05	-20.6± 0.9	16.20 ± 0.85	-27.59 ± 2.08	-31.9 ± 1.65
3992	7.27 ± 0.79	22.13 ± 22.13	-63.64 ± 0.56	5.5 ± 2.0	5.81 ± 1.05	-35.50 ± 4.22	-25.82 ± 2.87
40023	23.82± 0.74	-71.82 ± -71.82	-348.06 ± 0.43	-43 ± 2.0	38.16 ± 1.69	-52.25 ± 2.03	-51.62 ± 1.36
41484	45.89± 0.84	-18.98 ± -18.98	-351.48 ± 0.66	-33.8± 2.0	21.30 ± 1.63	-38.29 ± 0.67	-23.34 ± 1.17
42499	53.98± 1.04	-109.35 ± -109.35	-499.89 ± 0.75	-13.4± 2.0	19.08 ± 1.45	-30.37 ± 1.23	-30.21 ± 1.09
4346	6.54 ± 1	-6.99 ± -6.99	-44.82 ± 0.58	1.9 ± 2.0	20.53 ± 3.28	-22.31 ± 3.57	-12.87 ± 2.54
43557	41.42± 1.19	153.13 ± 153.13	-235.45 ± 0.66	3.5 ± 0.9	19.48 ± 0.87	-25.37 ± 0.84	4.78 ± 0.48
45617	57.05± 1.08	49.78 ± 49.78	-507.62 ± 0.51	-18 ± 2.0	22.69 ± 1.40	-36.93 ± 0.90	-15.55 ± 1.37
48390	24.9 ± 0.82	20.98 ± 20.98	-174.56 ± 0.42	-1.8 ± 0.9	13.04 ± 0.66	-30.62 ± 1.06	-4.01 ± 0.70
5027	38.99 ± 1.88	-34.15 ± -34.15	-316.8 ± 1.4	2.8 ± 5.0	24.98 ± 1.26	-29.47 ± 1.43	-4.05 ± 4.99
50505	48.45± 0.85	62.98 ± 62.98	-299.34 ± 0.63	-8.3 ± 2.0	13.33 ± 1.15	-28.03 ± 0.50	1.24 ± 1.65
52366	4.39 ± 0.79	-3.18 ± -3.18	-18.84 ± 0.55	15.5 ± 0.9	-4.17 ± 0.96	-22.38 ± 3.72	12.15 ± 0.92
5286	48.2 ± 1.06	99.08 ± 99.08	-491.71 ± 0.55	-3.4 ± 2.0	9.38 ± 0.96	-34.40 ± 1.41	-34.26 ± 1.51
53229	33.4 ± 0.78	92.47 ± 92.47	-286.06 ± 0.55	16.1 ± 0.9	15.90 ± 0.67	-36.31 ± 0.83	22.56 ± 0.83
53465	10.46± 0.72	14.4 ± 14.4	-97.54 ± 0.54	-54.4± 2.0	41.11 ± 1.46	-43.35 ± 2.79	-37.23 ± 1.93
6108	11.41 ± 0.98	-5.54 ± -5.54	-37.51 ± 0.5	11.1 ± 5.0	9.47 ± 1.19	-11.31 ± 1.02	-12.4 ± 4.96
6732	10.63 ± 0.77	50.82 ± 50.82	-58.73 ± 0.61	-41.7 ± 2.0	12.16 ± 9.17	-51.31 ± 16.7	12.58 ± 19.7

2.2.3 The Spectra

Spectroscopy of the sample was obtained in March 2007 and November 2008 with the KPNO 4 meter Mayall telescope, the Echelle spectrograph with grating 58.5-63 and a T2KB 2048X2048 CCD detector. The slit width of $\sim$ 1 arcsec yields a resolution of R $\sim$ 40,000, with a typical S/N of 200. The spectra have incomplete wavelength coverage extending from approximately 5800 Å to 7800 Å.

The spectra have been reduced using standard routines in the echelle package of IRAF[1] . These include bias correction, flat-fielding, scattered light correction, order extraction, and wavelength calibration. Sample spectra are presented in Figure 2.2.

[1] IRAF is distributed by the National Optical Astronomy Observatories, which are operated by the Association of Universities for Research in Astronomy, Inc., under cooperative agreement with the National Science Foundation.

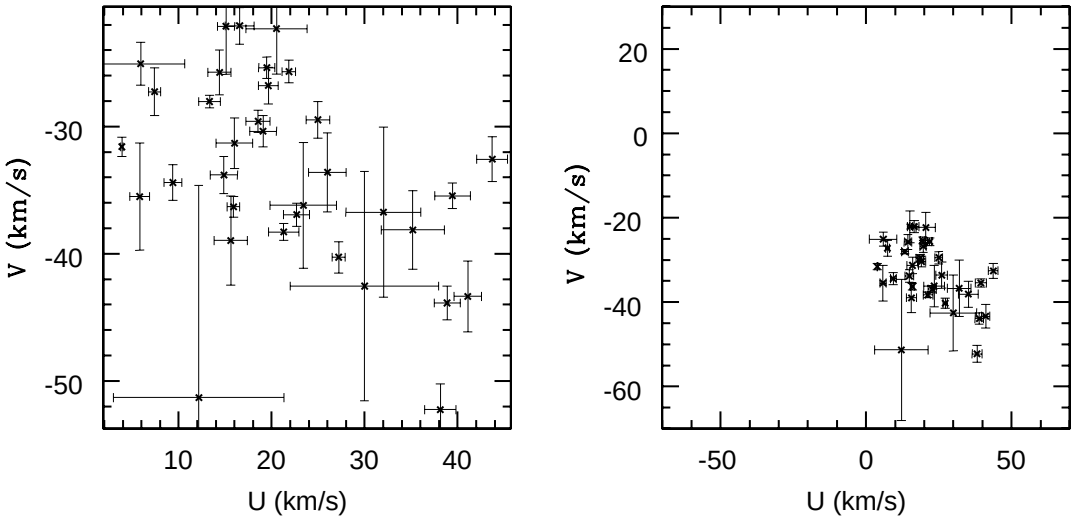

Figure 2.1 U and V kinematics for the 34 star Wolf 630 Sample. UVW kinematics were calculated from an updated version of the code of Johnson & Soderblom (1987). The left plot is a zoomed in view of all the stars while the second plot is a zoomed out scale, similar to the scales shown for literature studies of velocity structure in the solar neighborhood.

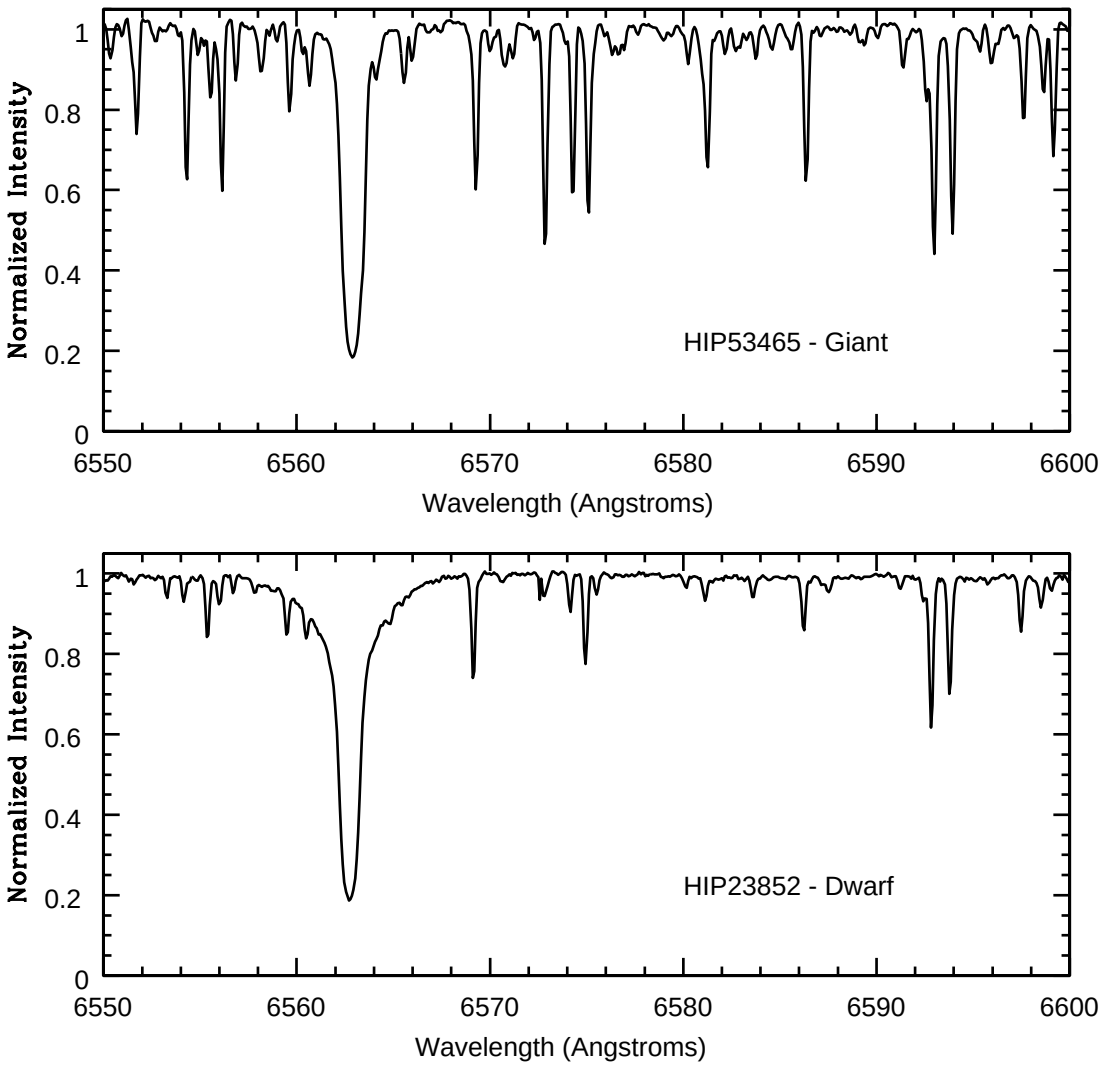

Figure 2.2 Sample normalized spectra for the 34 star sample. The top panel shows a giant star and the bottom displays a dwarf. The typical S/N in these spectra are ∼200.

CHAPTER 3

CHEMICAL ABUNDANCE ANALYSIS

3.1 Theory of Abundance Analysis

A standard spectroscopic abundance analysis has been applied to the spectroscopic sample. A rigorous treatment of the concepts underlying this form of analysis can be found in standard texts on stellar atmospheres (Mihalas (1978), Gray (2005)), but there are key components that merit a description, including the determination of basic physical parameters, formation of suitable linelists and selection of model atmospheres. The first step in allowing application of these techniques is to form a suitable line sample.

3.1.1 Line Selection

Spectroscopic physical parameters are typically determined by enforcing balance constraints on abundances derived from lines of Fe, which has a plethora of suitable neutral (Fe I) and ionized (Fe II) lines available in the optical. For spectroscopic work of this form, the linelists must contain the wavelength for the line, the excitation potential (i.e. energy difference between the ground state level and the lower level responsible for forming the absorption line) and the oscillator strengths, or log gf's (a line specific quantum mechanical measure of the probability for a transition to occur). Initially, low excitation potential ($\chi <$ 6.00 eV) Fe I lines from Thevenin (1990), the VIENNA Atomic Line Database (Piskunov et al. (1995), Ryabchikova et al. (1997), Kupka & Ryabchikova (1999), Kupka et al. (2000)), Yong et al. (2004), Schuler et al. (2006) and De Silva et al. (2007) were compiled. This initial linelist consisted of over 14,000 lines. To determine "good" lines (i.e. isolated and free from blending effects according to visual inspection) required searching for the lines in a high resolution solar spectrum. When a line was measurable , the equivalent width was recorded and marked for closer inspection. Lines which were not apparent in the solar spectrum were removed from the linelist. This reduced the line sample to 378 lines. In

order to guarantee that these lines were unaffected by blending effects, the MOOG spectral analysis program (Sneden, 1973) was used to compute synthetic spectra in 1 Å blocks surrounding allegedly "good" features using lists of all the lines in a given region from the Vienna Atomic Line Database (Kupka et al., 2000). If a line had closely neighboring features with MOOG-based relative strength parameters within an order of magnitude it was removed from consideration. In this manner, a final list of 145 Fe I lines and 11 Fe II lines was formed. These linelists are presented in Table 3.1 and Table 3.2. The equivelent widths listed are for measurements in a high resolution solar spectrum.

Table 3.1

Fe I Line List

Wavelength	Excitation Potential	log(gf)	Equivalent Width
Å	eV		mÅ
5505.881	4.42	-1.30	54.7
5506.778	0.99	-2.80	118.6
5522.447	4.21	-1.55	41.4
5536.580	2.83	-3.81	8.1
5539.280	3.64	-2.66	17.5
5543.936	4.22	-1.14	61.8
5546.500	4.37	-1.31	49.9
5546.991	4.22	-1.91	26.5
5553.578	4.43	-1.41	58.9
5554.882	4.55	-0.44	93.7
5557.977	4.47	-1.28	61.9
5560.207	4.43	-1.19	50.2
5562.706	4.43	-0.64	56.8
5574.389	4.42	-3.02	3.2
5576.089	3.43	-1.00	111.0
5577.030	5.03	-1.55	11.7
5579.335	4.23	-2.40	9.0
5583.968	4.19	-2.77	6.5
5587.574	4.14	-1.85	33.4
5607.664	4.15	-2.27	14.8
5617.186	3.25	-2.88	35.6
5621.603	5.11	-1.79	9.1
5646.684	4.26	-2.50	7.2
5651.469	4.47	-2.00	20.8
5652.318	4.26	-1.95	23.1

Table 3.1 – Continued

Wavelength	Excitation Potential	log(gf)	Equivalent Width
Å	eV		mÅ
5653.867	4.39	-1.64	35.8
5661.346	4.28	-1.74	22.4
5662.516	4.18	-0.57	82.8
5667.518	4.18	-1.58	49.2
5677.684	4.10	-2.70	6.0
5679.023	4.65	-0.92	54.4
5680.240	4.19	-2.58	9.3
5701.545	2.56	-2.22	77.4
5705.981	4.61	-0.53	91.1
5717.833	4.28	-1.13	56.3
5724.454	4.28	-2.64	7.3
5731.762	4.26	-1.30	56.9
5732.275	4.99	-1.56	14.3
5734.564	4.96	-1.57	6.1
5739.986	4.58	-2.06	6.7
5741.846	4.26	-1.85	31.4
5752.032	4.55	-1.18	53.2
5769.323	4.61	-2.26	7.1
5775.081	4.22	-1.30	56.6
5778.450	2.59	-3.48	20.7
5902.474	4.59	-1.81	13.0
5905.672	4.65	-0.73	61.0
5916.247	2.45	-2.99	52.6
5927.786	4.65	-1.09	41.5
5929.667	4.55	-1.41	37.1
5930.173	4.65	-0.23	83.7
5933.792	4.64	-2.23	8.2
5934.653	3.93	-1.17	71.1
5956.690	0.86	-4.60	52.7
5969.559	4.28	-2.73	3.2
6003.010	3.88	-1.12	81.4
6005.542	2.59	-3.60	22.1
6015.243	2.22	-4.68	5.2
6018.299	4.65	-2.08	9.5
6027.051	4.08	-1.09	64.5
6034.033	4.31	-2.42	9.5
6035.334	4.29	-2.59	5.8
6054.072	4.37	-2.31	8.7
6055.992	4.73	-0.46	70.4
6065.482	2.61	-1.53	113.7
6078.491	4.80	-0.32	80.9

Table 3.1 – Continued

Wavelength	Excitation Potential	log(gf)	Equivalent Width
Å	eV		mÅ
6078.999	4.65	-1.12	44.6
6083.660	3.88	-3.50	2.6
6085.259	2.76	-3.10	41.5
6098.245	4.56	-1.88	15.0
6102.171	4.83	-0.52	76.4
6105.131	4.55	-2.05	11.6
6120.249	0.91	-5.96	5.5
6127.907	4.14	-1.40	50.1
6151.617	2.18	-3.30	48.8
6157.728	4.08	-1.26	59.2
6159.368	4.61	-1.97	12.4
6165.360	4.14	-1.47	43.7
6170.504	4.79	-0.44	76.4
6173.336	2.22	-2.88	67.9
6187.987	3.94	-1.72	48.1
6213.429	2.22	-2.48	77.3
6219.280	2.20	-2.43	91.5
6220.776	3.88	-2.46	19.5
6226.730	3.88	-2.22	29.2
6232.641	3.65	-1.22	88.1
6240.645	2.22	-3.23	50.3
6246.317	3.60	-0.73	130.1
6252.554	2.40	-1.69	116.5
6256.360	2.45	-2.41	92.2
6265.130	2.17	-2.55	81.8
6271.280	3.33	-2.72	22.7
6290.974	4.73	-0.78	67.8
6293.924	4.83	-1.72	13.0
6322.685	2.59	-2.43	75.3
6335.328	2.20	-2.18	96.6
6336.820	3.68	-0.91	103.1
6344.148	2.43	-2.92	58.2
6380.743	4.19	-1.38	52.1
6392.538	2.28	-4.03	17.0
6393.612	2.43	-1.57	124.0
6408.018	3.69	-1.02	90.8
6411.647	3.65	-0.59	134.8
6469.193	4.83	-0.77	62.1
6494.498	4.73	-1.46	35.1
6494.980	2.40	-1.27	138.6
6496.467	4.79	-0.57	60.9

Table 3.1 – Continued

Wavelength	Excitation Potential	log(gf)	Equivalent Width
Å	eV		mÅ
6498.945	0.96	-4.70	44.0
6533.940	4.56	-1.38	52.4
6574.228	0.99	-5.02	26.7
6581.207	1.49	-4.68	19.4
6584.575	5.39	-1.34	3.7
6591.313	4.59	-2.07	9.5
6592.913	2.73	-1.47	110.2
6593.870	2.43	-2.42	81.2
6597.557	4.79	-1.07	46.5
6608.024	2.28	-4.03	18.4
6609.110	2.56	-2.69	66.9
6627.540	4.55	-1.68	25.4
6646.932	2.61	-3.99	10.2
6653.850	4.15	-2.52	9.9
6667.417	2.45	-4.40	4.0
6667.711	4.58	-2.11	7.8
6703.567	2.76	-3.16	40.4
6704.481	4.22	-2.66	6.9
6705.101	4.61	-1.39	47.0
6710.316	1.49	-4.88	16.5
6713.745	4.79	-1.52	20.4
6715.383	4.61	-1.64	28.7
6716.222	4.58	-1.92	15.5
6725.353	4.10	-2.30	17.8
6726.666	4.61	-1.13	47.2
6732.065	4.58	-2.21	8.1
6732.068	4.58	-2.17	8.1
6733.151	4.64	-1.58	26.7
6739.520	1.56	-4.79	11.7
6745.090	4.58	-2.16	8.8
6745.957	4.08	-2.77	6.4
6746.953	2.61	-4.35	4.0
6750.150	2.42	-2.62	73.1
6752.716	4.64	-1.30	35.5
6753.464	4.56	-2.29	5.6
6777.408	4.19	-2.82	7.9
6783.704	2.59	-3.98	11.7
6786.856	4.19	-2.07	24.0
6793.259	4.08	-2.33	12.8
7114.549	2.69	-4.01	7.9
7130.922	4.22	-0.79	90.1

Table 3.1 – Continued

Wavelength	Excitation Potential	log(gf)	Equivalent Width
Å	eV		mÅ
7142.517	4.96	-0.82	34.1
7284.835	4.14	-1.75	39.2
7285.273	4.61	-1.70	29.0
7802.473	5.09	-1.52	16.3
7807.909	4.99	-0.54	59.7
7820.803	4.29	-2.64	5.4
7844.555	4.83	-1.81	11.9
7879.748	5.03	-1.65	25.8

Table 3.2

Fe II Line List

Wavelength	Excitation Potential	log(gf)	Equivalent Width
Å	eV		mÅ
5991.380	3.15	-3.55	30.3
6084.110	3.20	-3.80	21.7
6147.741	3.89	-2.83	70.9
6149.249	3.89	-2.88	35.7
6238.392	3.89	-2.75	45.5
6247.557	3.89	-2.44	51.8
6369.462	2.89	-4.23	18.7
6416.919	3.89	-2.88	41.3
6442.950	5.55	-2.64	4.0
6446.400	6.22	-2.11	4.2
6456.380	3.90	-2.07	62.2

Linelists for other elements of interest have also been compiled from multiple sources (Thevenin (1990), King et al. (1998), De Silva et al. (2006)). These elements include Li, Na, Al, Ba, a selection of α elements (O, Mg, Si, Ca, Ti I and Ti II) and a selection of Fe peak elements (Cr, Mn and Ni). The lines are given in Table 3.3. The elements are denoted by atomic number and the given equivalent widths are again for measurements in the high resolution solar spectrum.

Table 3.3

Metals Line List

Wavelength	Element	Excitation Potential	log(gf)	Equivalent Width
Å	Atomic #	eV		mÅ
6154.230	11.000	2.10	-1.53	38.0
6160.750	11.000	2.10	-1.23	54.2
5711.090	12.000	4.35	-1.83	102.5
6698.670	13.000	3.14	-1.95	22.1
7835.310	13.000	4.02	-0.47	43.4
7836.130	13.000	4.02	-0.31	57.0
5665.560	14.000	4.92	-1.94	39.9
5690.430	14.000	4.93	-1.77	52.0
6142.480	14.000	5.62	-1.54	33.9
6145.010	14.000	5.62	-1.36	36.7
6155.130	14.000	5.62	-0.78	84.7
5868.570	20.000	2.93	-1.57	2.7
6161.297	20.000	2.52	-1.27	61.8
6166.439	20.000	2.52	-1.14	69.6
6169.040	20.000	2.52	-0.79	95.9
6169.560	20.000	2.53	-0.47	107.1
6455.600	20.000	2.52	-1.50	59.7
6464.680	20.000	2.52	-2.53	15.5
6499.650	20.000	2.52	-1.00	86.8
6572.800	20.000	0.00	-4.28	33.7
5877.657	22.000	3.32	-0.08	15.5
5978.541	22.000	1.87	-0.50	20.9
5999.658	22.000	2.24	-1.48	11.3
6064.626	22.000	1.05	-1.94	10.3
6126.216	22.000	1.07	-1.43	22.6
6258.102	22.000	1.44	-0.35	49.7
6258.706	22.000	1.46	-0.24	70.8
6261.098	22.000	1.43	-0.48	49.6
6336.099	22.000	1.44	-1.74	6.7
6668.376	22.000	3.58	0.20	4.7
6743.122	22.000	0.90	-1.63	17.6
7138.906	22.000	1.44	-1.70	6.4
7357.727	22.000	1.44	-1.12	23.9
6214.600	22.100	2.04	-3.46	7.1
6491.561	22.100	2.06	-1.79	43.8
6491.582	22.100	2.06	-2.15	44.6
6513.045	22.100	4.00	-1.31	3.2
6606.949	22.100	2.06	-2.79	8.9
6606.949	22.100	2.06	-2.79	9.5

Table 3.3 – Continued

Wavelength	Element	Excitation Potential	log(gf)	Equivalent Width
Å	Atomic #	eV		mÅ
7355.438	22.100	2.59	-1.91	15.2
7355.438	22.100	2.59	-1.91	17.6
6330.100	24.000	0.94	-2.99	26.9
6729.750	24.000	4.39	-0.66	4.2
6013.530	25.000	3.07	-0.25	86.8
6016.670	25.000	3.08	-0.10	95.8
6021.800	25.000	3.08	0.03	98.8
5846.990	28.000	1.68	-3.21	23.6
6086.280	28.000	4.26	-0.51	44.2
6175.370	28.000	4.09	-0.53	47.8
6327.600	28.000	1.68	-3.23	38.3
6378.260	28.000	4.15	-1.00	32.5
6414.590	28.000	4.15	-1.18	15.6
6482.810	28.000	1.93	-2.97	42.5
6532.880	28.000	1.93	-3.47	17.1
6598.610	28.000	4.23	-1.02	26.9
6635.140	28.000	4.42	-0.82	26.2
6643.640	28.000	1.68	-2.01	92.6
6767.780	28.000	1.83	-1.89	80.4
6772.320	28.000	3.66	-0.98	51.3
6842.040	28.000	3.66	-1.48	23.8
5853.690	56.100	0.60	-1.00	66.2
6141.730	56.100	0.70	-0.07	119.6
6496.910	56.100	0.60	-0.41	100.0
6300.310	8.000	0.00	-9.72	5.2
6363.790	8.000	0.00	-9.72	2.8
7771.940	8.000	9.15	0.37	70.9
7774.170	8.000	9.15	0.22	60.3
7775.390	8.000	9.15	0.00	48.8

Equivalent Widths

With an appropriate line sample, equivalent widths for the lines of interest were measured in each star using the spectral analysis tool SPECTRE. The lines in stellar spectra are characterized by a variety of broadening effects (instrumental, natural, pressure, doppler, rotational, van der Waals, etc.); however the most dominant of these, for the spectra in this

study, is the instrumental broadening. The magnitude of this instrumental broadening can be modeled by a Gaussian shape and, in practice, is determined by measuring clean, weak stellar lines in the observed spectra by fitting them with gaussian profiles using SPECTRE.

Final abundances were obtained from equivalent widths through use of the MOOG LTE Spectral analysis tool (Sneden, 1973). MOOG utilizes an input model atmosphere (described below) to solve the equations of LTE line formation for the sample of lines. It utilizes an intrinsic curve of growth approach to compute theoretical line profiles for each line (i.e. fine analysis), and force fits abundances to match the observed equivalent widths.

3.1.2 Model Atmospheres

For the late type (F, G and K) stars of our sample, an appropriate choice for model atmospheres, commonly utilized in the literature, are the 1D plane-parallel model atmospheres of Robert Kurucz (Castelli & Kurucz, 2004). Broadly, these model atmospheres break the photosphere of a star (the outer atmosphere where the majority of visible wavelength spectral lines are formed) into many, subsequent layers. Within a given layer the equations of hydrostatic equilibrium hold (pressure balances with gravity) and energy transport is through radiative processes. Perhaps the most essential assumption in these model atmospheres is that of local thermodynamic equilibrium (LTE). In LTE, the transfer equation is solved assuming a blackbody source function and the properties of a small volume of gas are determined by the thermodynamic equilibrium values determined from the local temperatures and pressures. Typically these model atmospheres are created based on the four fundamental physical parameters that are used to describe a star; temperature, surface gravity, metallicity, and microturbulent velocity.

3.1.3 Basic Physical Parameters

Determining the basic physical parameters for a star requires measuring equivalent widths of multiple lines of various excitation potentials for a single element. As mentioned, the element chosen for this sample, and indeed the most common element for other studies

of this type, is Fe due to the plethora of measurable optical Fe lines available. The determination of physical parameters as described below depends on the use of the comprehensive linelists for both Fe I and Fe II. Additionally, in discussing the determination of basic physical parameters, it is necessary to keep in mind the following general characteristics of the solar-type stars of this sample, as discussed in Gray (2005):

1) Singly ionized Fe (Fe II) is the dominant state (although note that this may not be true for the coolest stars of the sample).

2) Weak lines formed by an atom where most of the element is in the next higher ionization stage are insensitive to pressure changes which implies that Fe I is unaffected by pressure changes.

3) Weak lines that are formed by an ion where most of the element is in that same ionization stage are pressure sensitive, therefore Fe II lines are pressure sensitive.

Temperature

In the LTE approximation utilized herein, the distribution of atoms over their energy levels is characterized by the Boltzmann excitation equation:

$$\frac{N_n}{N} = \frac{g_n e^{-\frac{\chi_n}{kT}}}{u(T)},$$

where N_n is the number of atoms excited to the $n_{th.}$ level, N is the total number of atoms, g_n is the statistical weight, χ_n is the excitation potential of the level of interest, k is Boltzmann's constant, *u(T)* is the partition function (the sum of Boltzmann factors for an atom, which is hard-coded into MOOG) and ***T* is the excitation temperature**. This is the temperature that is spectroscopically derived. While NLTE effects are unlikely to be present in most of the star's in the sample, in general if they were present they may manifest themselves in overexcitation/overionization effects where abundances for two different ionization stages are different or different excitation potential lines yield different abundances. Such NLTE effects are discussed in more detail in Chapter 5.

The approach taken to determine this temperature relies on the fact that a star has a single abundance for any given element and that the Boltzmann excitation equation

describes how the energy levels of an atom are populated at a given temperature for a given excitation potential. Consider the large linelist for neutral Fe discussed above. This list contains measurements of line strengths (equivalent widths) for lines with a variety of excitation potentials. The relative populations of atoms responsible for forming a given line can be determined by solving the Boltzmann excitation equation for the line's excitation potential and a guess of the star's temperature, used to calculate a model atmosphere. From the relative populations determined with this characteristic temperature, the MOOG Spectral Synthesis tool uses the classical equations of LTE line formation to compute an abundance which fits with the strengths of the measured equivalent widths. Consider what happens if the assumed temperature is too low. There will be fewer electrons excited to higher energy states. With fewer electrons in higher states, the relative population of atoms for high excitation potential lines will be lower. Consequently the abundances for the higher excitation potential lines will have to be artificially increased to match the observed equivalent widths and abundances will increase as a function of excitation potential. Likewise, if the assumed temperature is too high, then there will be too many electrons excited to higher energy states and the higher excitation potential lines will be fit by abundances that are too low. Once a temperature is reached that yields a single abundance for all lines of a given element that is independent of the excitation potential, the correct temperature can be considered determined. All lines are unlikely to yield the exact same abundance, consequently the temperature is determined such that it minimizes any correlation between abundance and excitation potential, i.e. excitation balance. Once excitation balance has been achieved, there is a "two-for-one" deal where, by minizing the correlation in abundance versus excitation potential, the excitation temperature is obtained as well as the Fe abundance of the star! The approach is depicted in Figure 3.1. Practically, there is a complex interplay whereby the abundances from Fe I lines also show some sensitivity to variations in log g and microturbulence, consequently the solution for temperature using excitation balance must be reached in tandem with solutions for surface gravity and microturbulence.

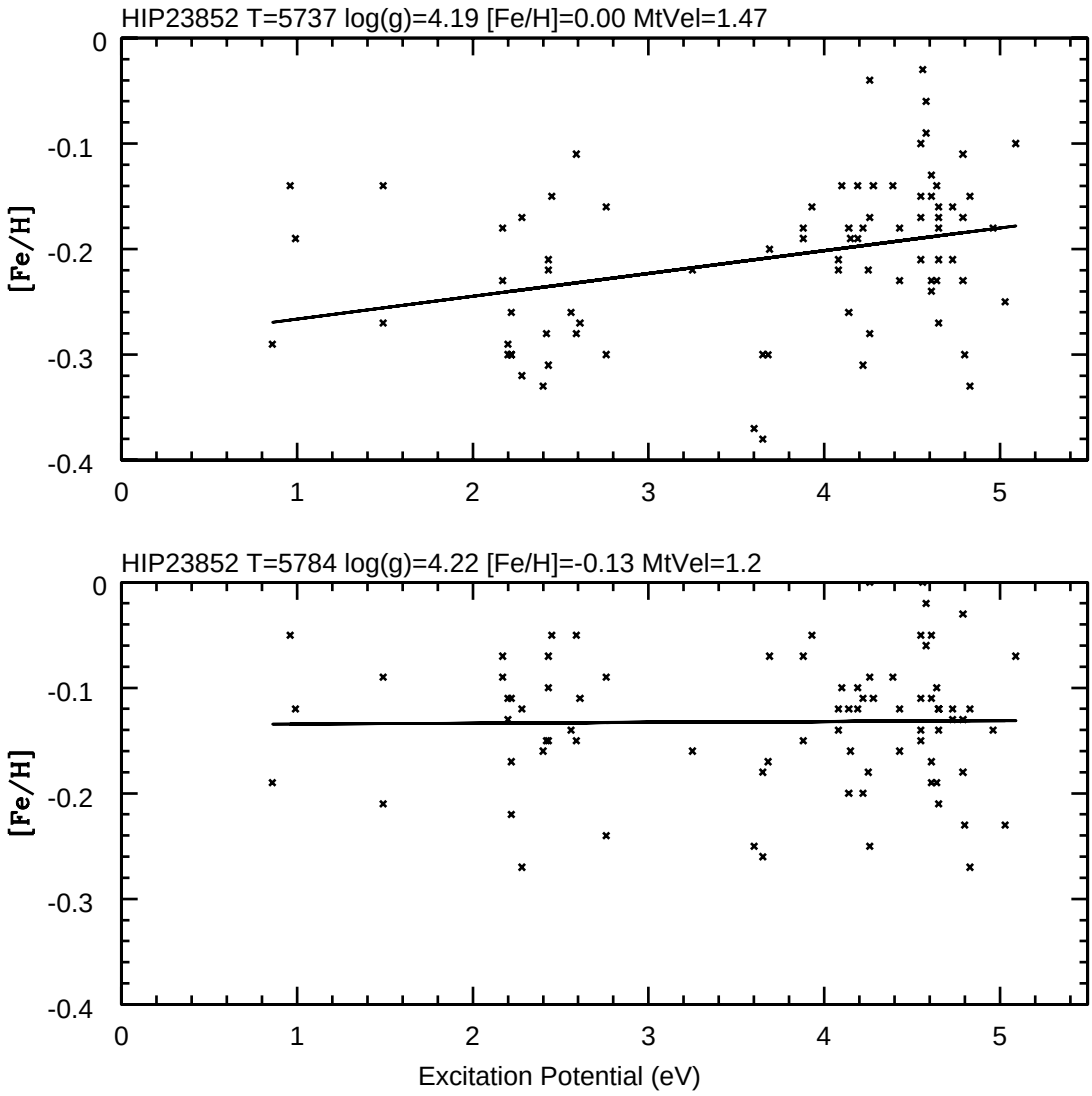

Figure 3.1 Plot of the excitation balance technique used to determine spectroscopic temperatures. The top panel gives the initial guess for basic physical parameters. Note the positive slope, which indicates that the higher excitation potential lines have enhanced abundances and the lower excitation potential lines have apparently lower abundances. This is due to a temperature which is too low. In this case, the enhanced abundances from the higher excitation potential lines are a side effect of the temperature being too low, consequently the number of electrons populating higher levels is too low and the abundance is enhanced in order to match the measured equivalent widths. The bottom plot has increased the temperature which yields an overall abundance independent of excitation potential. This is referred to as excitation balance.

Surface Gravity

The surface gravity is defined by the mass and radius of a star as $g = g_{\odot}\frac{M}{R^2}$ where $g_{\odot}$ is the surface gravity of the Sun, M is the mass of the star in solar masses and R is the radius of the star in solar radii. Typically the surface gravity is expressed in logarithmic form (logg, not to be confused with loggf, which is the line specific quantum mechanical transition probability). Physically, the surface gravity is a measure of the pressure at the surface of a star.

In this work, the surface gravities are determined via ionization balance, whereby abundances of the pressure sensitive Fe II lines are forced to match abundances from the pressure insensitive Fe I lines, achieved by adjusting the surface gravity in a model stellar atmosphere. Similar reasoning which underlies excitation balance can be applied to understand the process of ionization balance which depends on the ratio of ionized species to neutral species present in an atmosphere, given by the Saha ionization equation,

$$\frac{N_1}{N_0}P_e = \frac{(2\pi m_e)^{3/2}(kT)^{5/2}}{h^3}\frac{2u_1(T)}{u_0(T)}e^{\frac{-I}{kT}}$$

where N_1 is the number of ionized atoms, N_0 is the number of neutral atoms, P_e is the electron pressure (provided by the model atmosphere), u_1 is the partition function for ions (hard-coded into MOOG), u_0 is the partition function for neutral atoms (hard-coded into MOOG), m_e is the mass of an electron and h is Planck's constant. The relevant parameter in the Saha equation, which is dictated by the surface gravity, is the electron pressure.

With the correct Fe abundance and the excitation temperature both constrained by excitation balance of Fe I lines, the surface gravity can be determined using Fe II lines. With an assumed surface gravity, the equivalent width is converted into its respective abundance using the relative ionization populations from the Saha equation. If the surface gravity is too low, the pressure in the model atmosphere is likewise low. For a constant temperature (obtained from excitation balance) a lower pressure will increase the number of ions relative to neutrals according to the Saha equation. An increase in the number of ions will lead to an increase in the continuum opacity which is formed by the negative hydrogen ion for solar-type stars. An increase in continuum opacity increases continuum absorption, thus

decreasing line absorption. A surface gravity which is too low, therefore, results in weaker strengths for line profiles and yields lower abundances. Conversely, an assumed surface gravity which is too high overestimates the pressure, which will decrease the ionization ratio. This decreases the continuum opacity which yields stronger line profiles which in turn give higher abundances. The process for ionization balance, therefore, utilizes temperatures and abundances (from excitation balance) to fix these parameters in the Saha equation and Fe II, being the dominant ionization stage for solar-type stars, is sensitive to surface gravity (i.e. pressure) changes. The surface gravity is considered determined when the average abundance determined from the gravity sensitivity Fe II lines matches the abundance from Fe I lines. Recall that this ionization balance must be done simultaneously with determining the temperature and microturbulent velocity. The approach can be seen in Figure 3.2.

Metallicity

The metallicity is a measure of the metal content of a star, where a "metal" is taken to be any element other than hydrogen or helium. It is conventionally quoted in bracket notation, [Fe/H] which is defined as:

$$[\mathrm{Fe/H}] = \log\frac{\mathrm{N(Fe)}}{\mathrm{N(H)}}_{\star} - \log\frac{\mathrm{N(Fe)}}{\mathrm{N(H)}}_{\odot},$$

where quantities subscripted with a $\star$ represent the stellar parameters and those with $\odot$ are for the Sun and $\log N(\mathrm{X})$ is the logarithm of the number of atoms of element X. The metallicities given in this work are quoted in bracket notation where $\mathrm{Log}N(\mathrm{H})\equiv 12$. They have been determined using the abfind package in MOOG.

Microturbulent Velocity

The microturbulent velocity (ξ) is used to account for additional broadening observed in saturated spectral lines that is otherwise not adequately modeled with natural broadening, thermal broadening, pressure broadening or broadening by an instrumental profile. In this sense it is a"fudge factor". It is assumed to represent small non-thermal motions on scales that are less than a mean free path over which a photon travels in a stellar atmosphere. The microturbulence, therefore, represents motions smaller than the

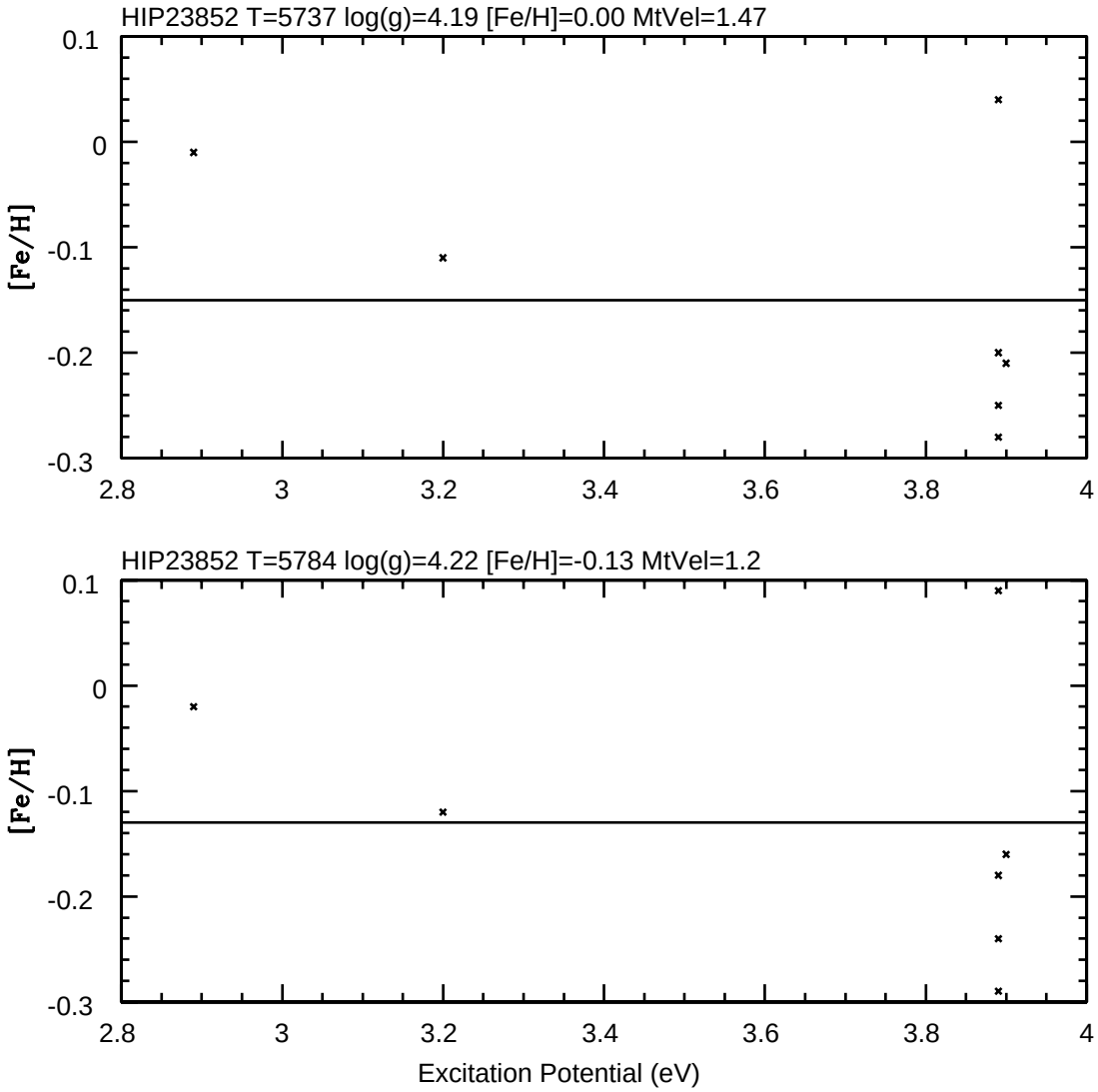

Figure 3.2 Plot of the Fe II abundance versus excitation potential for one of the stars of the sample. This depicts ionization balance as discussed in the text. The surface gravity of the model atmosphere in the top plot has not been adjusted in surface gravity to force the average abundance derived from Fe II lines to match the average abundance from Fe I lines. By adjusting the surface gravity of the model atmosphere, the abundances from Fe II lines are forced to match the abundance from Fe I lines. This is referred to as ionization balance.

size over which a line profile is formed. Consequently, microturbulent velocities can take photons which are emitted from the line center and move them to be absorbed in the line wing due to micro-scale motions within the line. This leads to a desaturation of the line core and a broadening of the line wings. Therefore, microturbulence both strengthens and broadens a spectral line profile. This is in contrast to macroturbulent broadening (e.g. natural, thermal, pressure, rotational or instrumental) which acts to "smear" out a line profile. The motions that smear these lines are on scales that are larger than the characteristic scales over which the lines form therefore line strengths (equivalent widths) are preserved. In the actual computations the microturbulent velocity is treated as an additional Gaussian broadening component, centered around an average speed, referred to as the microturbulent velocity (Mihalas, 1978). Typical values are between 1-3 kms^{-1}.

In this work the microturbulent velocity is determined by using equivalent width balance whereby all lines of Fe I are forced to yield the same abundance, regardless of equivalent width. Microturbulence becomes important in strong line profiles, which would otherwise be saturated, where a saturated line is one that has absorbed the maximum number of photons possible. Adding more atoms to the line (i.e. increasing the abundance) does not increase the line strength in a saturated line, consequently saturated lines are insensitive to abundance. By increasing the microturbulent velocity, absorbers are shifted to the line wings and more flux can be removed from the profile. The process is to consider a variety of Fe I lines with varying strength. Each of these lines should, as usual, yield the same abundance for a given star. Assuming that the temperature and surface gravity are determined from excitation and ionization balance, if the microturbulent velocity is too high, then abundances from strong lines will require too few absorbers to match the observed line strength. If the microturbulence is too low, the number of absorbing atoms required to match the line profile will be too large. The microturbulence can be considered correct when the abundance derived does not depend on the strength of the line (i.e. equivalent width balance). Equivalent width balance is shown in Figure 3.3.

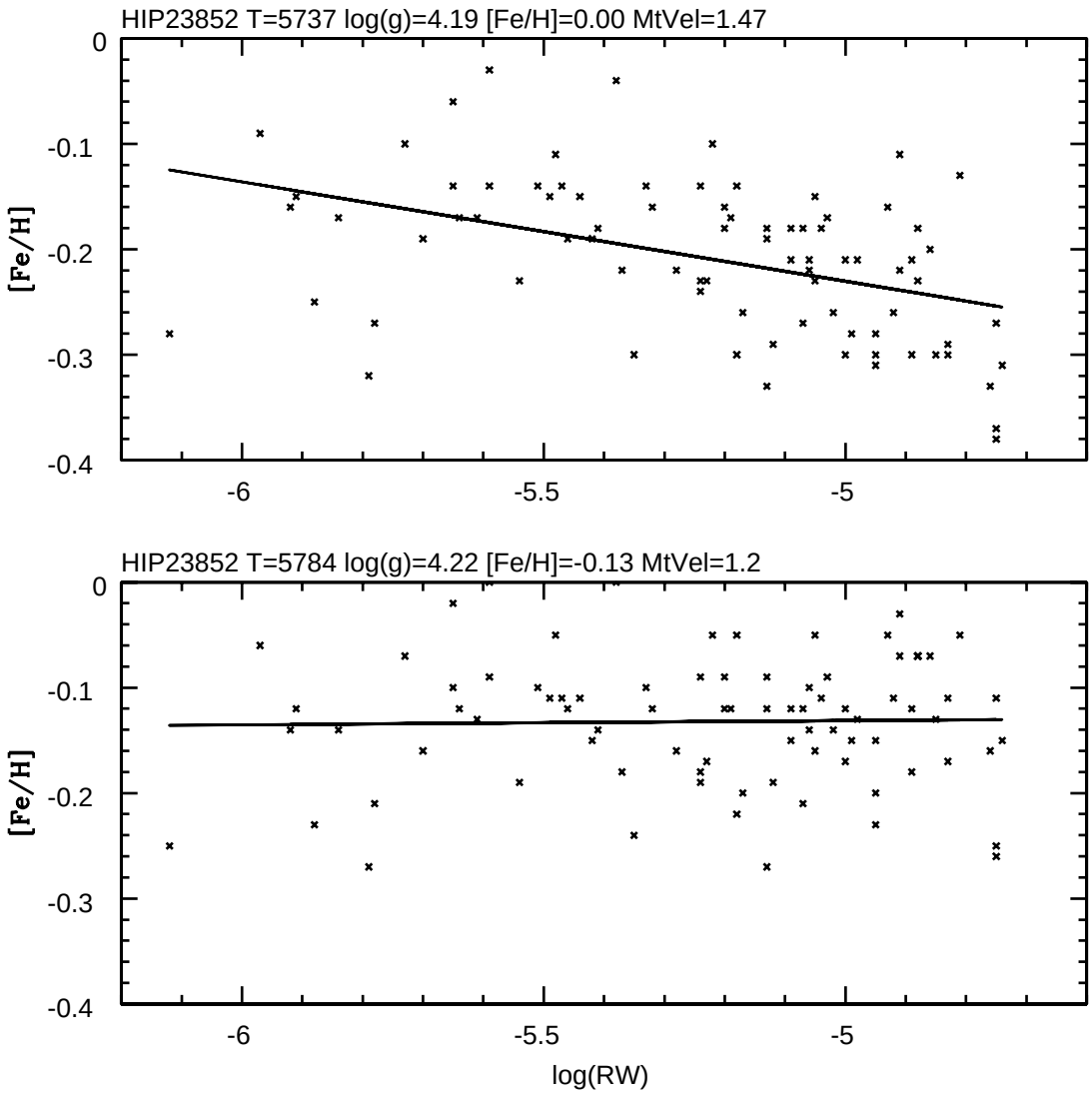

Figure 3.3 Plot of the equivalent width balance approach for determining microturbulent velocity. The [Fe/H] is plotted versus reduced equivalent width. In the top plot, notice that the microturbulence is loo high, consequently the abundance derived from strong lines is lower than from weak lines. By decreasing the microturbulent velocity, the correlation between [Fe/H] and line strength (log(RW)) is minimized and the microturbulence is considered determined. This is referred to as equivalent width balance.

3.1.4 Lithium

Abundances have been derived for lithium using spectral synthesis. This utilizes the synth driver of MOOG to synthesize a spectrum of the lithium line at λ=6707.79 Å using an updated version of the linelist from King et al. (1997) (private communication). Appropriate smoothing factors were determined by measuring clean, weak lines in the lithium region. These lines give a measure of the instrumental broadening with typical smoothing factors having Gaussian FWHMs of 0.20 mÅ. The lithium abundance is varied until a best fit is obtained from visual inspection. Respective uncertainties in lithium abundances have been determined by synthesizing lithium abundances for arbitrary changes in physical parameters of ΔT=150 K, $\Delta\log g$=0.12 cms^{-2} and $\Delta\xi$=0.60 kms^{-1}, and adding the resultant abundance differences in quadrature.

3.1.5 Oxygen

Oxygen abundances have also been determined for many of the stars in the sample. Abundances have been derived from the near-IR triplet at λ7771 Å, λ7774 Å and λ7775 Å using a standard equivalent width approach. Abundances derived from the triplet are known to be enhanced by NLTE effects, therefore appropriate corrections are applied, following Takeda (2003). Temperature dependent trends, whereby the two red features of the triplet yielded increased abundances as a function of decreasing temperature are noted here, and will be discussed later.

For the giant and subgiant stars of the sample, oxygen has also been derived from the forbidden line at λ6300.34 Å. This line is found to be free from NLTE effects from the work of Takeda (2003), and therefore is considered the ideal feature for deriving oxygen abundances. Care must be taken, however, as the λ6300.34 Å line is blended with a nearby Ni feature at λ6300.31 Å. This blend is treated using the blends driver of MOOG, following Schuler et al. (2006). In these analyses, the Ni abundance utilized to account for blending is the observed Ni abundance for the star.

There is also possible CN blending with a feature at 6300.265 Å and two features at 6300.482 Å with gf values of 5.78E-3, 6.82E-3 and 2.01E-3, respectively, taken from Davis & Phillips (1963). In order to explore the reality of these blending features, multiple oxygen syntheses of the λ6300 Å region were performed using a high resolution spectral atlas of the Sun (Kurucz, 2005) and the K giant, Arcturus (Hinkle et al., 2000). The CN features, if real, were found to be unimportant in the solar spectrum. Large variations in carbon abundances ($>$ 0.50 dex) appear to have little impact on the overall spectrum. For solar type dwarfs, the syntheses confirm that the strong blending features are the Ni isotopes at 6300.335 Å and 6300.355 Å. The situation appears to be dramatically different for cooler giants. In the high resolution spectral atlas for Arcturus, the CN blend, if real, appears to dominate over the Nickel blend. Oxygen syntheses were performed in order to calibrate the gf values of the CN molecules in the linelist to match the spectrum of Arcturus, but results are inconclusive. In particular, appropriate smoothing factors are difficult to determine as the ultra high resolution of the Arcturus atlas make Gaussian smoothing by an instrumental profile inappropriate. In an attempt to accurately reflect the smoothing in the spectral atlas, broadening was done using a convolution of a macroturbulent broadening of 5.21 $\pm$ 0.2 kms^{-1} (Gray, 1981) and a rotational broadening characterized by vsin(i)=2.4 $\pm$ 0.4 kms^{-1} (Gray, 1981) with a limb darkening coefficient of 0.9 (from Gray (2005)). With this smoothing, the spectrum for Arcturus in the forbidden oxygen region was fit by increasing the CN features gf values by $\sim$0.40 dex, while assuming a [C/Fe]=-0.06 as found by Smith et al. (2002). In attempting to apply this calibrated linelist to synthesize the forbidden line region for one of the giants in our sample (HIP17792; chosen because its physical parameters were similar to those of Arcturus) no reasonable abundance of carbon yielded a satisfactory fit. This may suggest that the gf values in the linelist need to be more well constrained. In light of the ambiguous results, it is concluded that an accurate determination of the carbon abundance is essential for proper treatment of any CN blending feature that may exist. It is suggested that a spectroscopic analysis of cool giants with appropriate wavelength coverage to allow measurement of a precise carbon abundance would allow for

calibration of the forbidden oxygen linelist, which would be a project of not insignificant interest. Unfortunately the wavelength coverage of the observed spectra does not include any appropriate carbon features to allow definitive conclusions as to the reality of the CN blending features found in Davis & Phillips (1963). In light of the unresolved nature of this CN blending, abundances reported herein do not include it. Final oxygen abundances for the forbidden line were derived using the blends driver without the CN features. The results will be discussed later.

3.2 Practical Abundance Analysis

3.2.1 Initial Parameters: Photometric

The color-T_{eff}-[Fe/H] calibrations of Ramírez & Meléndez (2005) were used to determine photometric temperatures from Johnson $B-V$, Tycho B_T-V_T, Johnson/2MASS $V-J_2$, $V-H_2$ and $V-K_2$. The color indices for 8 stars were outside of the calibrated ranges; consequently photometric temperatures were not derived. Uncertainties in the photometric temperatures were conservatively taken as the standard deviation of the temperatures derived from each of the respective colors. With the availability of high quality Hipparcos Parallaxes, physical surface gravities were calculated from:

$$log\frac{g}{g_\odot} = log\frac{M}{M_\odot} + 4log\frac{T_{eff}}{T_{eff,\odot}} + 0.4V_o + 0.4B.C. + 2log\pi + 0.12$$

where M is the mass in solar masses from Yale-Yonsei isochrones (Demarque et al., 2004), photometric temperatures were used for T_{eff}, bolometric corrections were taken from Gray (2005), V_o is the apparent magnitude and π is the parallax. Initial microturbulent velocities were found from the calibrations of Allende Prieto et al. (2004) who derived a calibration for calculating microturbulence as a function of effective temperature and surface gravity.

These photometric parameters provide the initial guesses for physical parameters when deriving the final spectroscopic values. Additionally, the photometric calibrations provide reasonable estimates to compare to spectroscopically derived results.

3.2.2 Final Parameters: Spectroscopic

The linelists discussed in Section 4.1.1 acted as target lists for measuring lines in each of the stars in the sample. The typical star contained ∼80 of the 145 good Fe I lines that were measurable in the solar spectrum. Upon examining the equivalent widths, several of the stellar linelists showed correlations between excitation potential and reduced equivalent width. Consider the effect that this correlation would introduce into the physical parameters. If the linelist used in enforcing excitation balance and equivalent width balance is correlated, then these correlations will be imposed onto the temperatures and microturbulent velocities, resulting in potentially spurious determinations of physical parameters.

Consequently, two linelists for the Fe I lines were formed; a correlated and an uncorrelated sample.

Final basic physical parameters for the sample were derived using a modification to the standard techniques of excitation/ionization balance. The following approach was utilized for 29 of the 34 stars in the sample. The remaining 5 stars would not converge to acceptable solutions with this approach so an alternative technique was developed as described below. In all the approaches described below, a differential analysis was used where the same lines were measured in a solar spectrum and in the stellar spectra. Final abundances were then determined by subtracting the solar abundance from the stellar abundance in a line by line fashion.

The first technique utilized the uncorrelated line sample in a classical approach of excitation and ionization balance. In this approach, temperatures of input model atmospheres were adjusted to remove any correlation in abundances with respect to excitation potential. In equivalent width balance, abundances were required to show no correlation with line strength to determine the microturbulent velocity. Finally the abundance from Fe II lines was forced to match the abundance from Fe I lines to determine surface gravity. This approach required simultaneously adjusting temperatures, surface gravities, metallicities and microturbulent velocities to converge to a common solution. Use of the uncorrelated line sample, as described above, is necessary to assure a unique solution. This approach will be referred to as the "classical" approach.

The second approach used the correlated line sample. Hipparcos physical surface gravities were used to set the surface gravity. The Fe II abundances, being sensitive to the surface gravity, are therefore set by this gravity. The temperature was adjusted to force the mean abundance from Fe I lines to match that from Fe II lines. The microturbulent velocity was adjusted until the abundance from Fe I lines had no dependence on reduced equivalent width. The advantage of this approach is that it does not require simultaneous solutions requiring excitation balance and equivalent width balance, allowing use of the full,

correlated line sample. This approach will be referred to as the "physical surface gravity" approach.

When comparing results from the classical and physical surface gravity approaches it was apparent that the results for the microturbulent velocity in most cases were identical. For this reason, a third approach was used for finding the final basic physical parameters. The microturbulent velocities from the "classical" approach and the "physical surface gravity" approach were averaged to yield a final value. Again, for all of the stars the microturbulent velocities in the two approaches were identical within uncertainties. The correlated line sample was used to determine the temperature and surface gravity using excitation/ionization balance. This approach will be referred to as the "fixed microturbulence" approach. For the remainder of the work, the results from the "fixed microturbulence" approach were used for the physical parameters of these 29 stars. The parameters in this technique, thus, are all derived from spectroscopic measurements and are formed from the most complete linelist available for a given star.

3.2.3 Final Parameters: Photometric/Spectroscopic Hybrid Alternative

The coolest stars in the sample (HIP105341-dwarf, hip114155-giant and hip5027-dwarf) had an insufficient number of Fe II lines for determining the surface gravity spectroscopically . Consequently, Hipparcos-based physical surface gravities were used to set the gravity, and the temperature and microturbulence were iterated to eliminate correlations in [Fe/H] versus excitation potential (excitation balance) and [Fe/H] versus the reduced equivalent width (equivalent width balance). Using the nomeclature described above, this is basically the "classical" approach with a fixed surface gravity.

Finally, one of the stars in the sample (Hip 5027) had a microturbulence correlation which could not be removed without utilizing unreasonable surface gravities. For this star, the surface gravity was set based on Yale-Yonsei isochrones (Demarque et al., 2004). The microturbulent velocity was set to zero and the temperature was determined from excitation balance. While this is not unprecedented, for example Gray (2005) quotes typical

microturbulent velocities between 0 and 1.5 kms^{-1} for dwarfs stars, it does indicate the semblant nature of microturbulence as a real parameter. While the small scale motions that microturbulence attempts to mimic are undoubtedly occuring, their treatment as additional Gaussian broadening convolved with the well constrained thermal broadening is deficient, although the treatment does adequately reproduce observations in most cases.

The final basic physical parameters (T_{Spec}, logg, microturbulent velocity (ξ) and [Fe/H]) are presented in Table 3.4.

Table 3.4

Basic Physical Parameters

HIP	T_{spec}	Log(g)	χ	[Fe/H]
	K	cms^{-2}	kms^{-1}	
102531	6238 ± 59	3.80 ± 0.16	1.85 ± 0.05	0.07 ± 0.04
103983	5750 ± 56	4.52 ± 0.20	1.16 ± 0.06	0.02 ± 0.05
105341[a]	4005 ± 88	4.67 ± 0.28	0.83 ± 0.60	-0.05 ± 0.19
11033	4510 ± 69	2.40 ± 0.30	1.60 ± 0.08	0.12 ± 0.04
112222	6369 ± 100	4.10 ± 0.26	1.69 ± 0.08	0.04 ± 0.07
112447	6095 ± 100	3.75 ± 0.25	1.82 ± 0.16	-0.34 ± 0.08
113622	4295 ± 86	2.10 ± 0.25	1.52 ± 0.13	0.00 ± 0.08
114155[a]	4348 ± 75	1.34 ± 0.25	2.19 ± 0.08	-0.58 ± 0.07
114924	6179 ± 40	4.36 ± 0.12	1.59 ± 0.05	0.06 ± 0.03
12784	4701 ± 54	2.68 ± 0.07	1.49 ± 0.10	0.09 ± 0.13
13701	4675 ± 30	2.71 ± 0.07	1.37 ± 0.08	-0.03 ± 0.03
14501	5785 ± 57	4.44 ± 0.20	1.24 ± 0.03	-0.08 ± 0.04
17792	4416 ± 32	2.09 ± 0.20	1.50 ± 0.03	-0.52 ± 0.06
23852	5778 ± 38	4.22 ± 0.23	1.22 ± 0.06	-0.14 ± 0.06
29525	5710 ± 31	4.57 ± 0.08	1.28 ± 0.09	-0.03 ± 0.03
29843	6130 ± 60	4.11 ± 0.15	1.52 ± 0.08	0.12 ± 0.08
33671	6040 ± 55	4.40 ± 0.15	1.38 ± 0.08	-0.21 ± 0.04
34440	4757 ± 39	2.43 ± 0.21	1.46 ± 0.08	-0.15 ± 0.04
3455	4860 ± 35	2.53 ± 0.07	1.49 ± 0.05	0.00 ± 0.03
3559	5800 ± 38	4.07 ± 0.05	1.27 ± 0.05	-0.18 ± 0.03
36732	4667 ± 62	2.54 ± 0.20	1.44 ± 0.09	0.10 ± 0.06
3992	4772 ± 53	2.58 ± 0.13	1.59 ± 0.06	-0.15 ± 0.04
40023	5290 ± 37	3.77 ± 0.06	1.21 ± 0.06	-0.05 ± 0.03
41484	5855 ± 39	4.41 ± 0.15	1.17 ± 0.05	0.08 ± 0.03
42499	4994 ± 32	4.41 ± 0.20	0.59 ± 0.19	-0.56 ± 0.10
4346[a]	3820 ± 200	1.39 ± 0.30	1.33 ± 0.17	0.24 ± 0.18
43557	5816 ± 42	4.52 ± 0.10	1.15 ± 0.12	-0.03 ± 0.04

Table 3.4 – Continued

HIP	T_{spec}	Log(g)	χ	[Fe/H]
	K	cms^{-2}	kms^{-1}	
45617	4855 ± 55	4.35 ± 0.10	1.01 ± 0.10	-0.12 ± 0.02
5027[b]	4398 ± 79	4.70 ± 0.29	0.00 ± 0.30	-0.08 ± 0.17
50505	5655 ± 41	4.42 ± 0.14	1.16 ± 0.10	-0.14 ± 0.03
5286	4683 ± 74	4.56 ± 0.25	0.54 ± 0.24	0.29 ± 0.07
53229	4690 ± 34	2.61 ± 0.20	1.47 ± 0.05	-0.10 ± 0.15
53465	4570 ± 65	2.50 ± 0.30	1.30 ± 0.08	-0.08 ± 0.07
6732	4665 ± 42	2.45 ± 0.10	1.58 ± 0.06	-0.03 ± 0.04

[a] Surface gravities for these stars are physical, calculated as discussed in the test.

[b] Surface gravity for this star is physical, calculated as discussed in the text. The microturbulence was set to 0.

Uncertainty Estimates

There are numerous uncertainties which must be accounted for in spectroscopic abundance analysis work. The transition probabilities in this work have been determined experimentally, observationally by forcing agreement for a given line when compared with a high resolution solar spectral atlas and theoretically calculated. The typical uncertainty for the observed and theoretically calculated log(gf)'s can be as high 0.1 dex and this accuracy can be a not insignificant source of error; however, by performing a line-by-line differential analysis the uncertainties due to transition probabilities cancel each other out in the stars and the Sun, minimizing this source of error.

The uncertainty in physical parameters underlies the uncertainties in the abundances. Errors in the temperature were determined by adjusting the temperature solution until the correlation between [Fe/H] and excitation potential (excitation balance) reached a 1-sigma linear correlation coefficient for the given number of lines. The uncertainty in microturbulent velocity was determined in the same manner, by adjusting the microturbulence until the linear correlation coefficient for [Fe/H] versus equivalent width (equivalent width balance) resulted in a 1-sigma deviation. For Hip5027, which would not converge to

a unique solution for microturbulence, an uncertainty in microturbulence of 0.20 kms^{-1} was adopted.

The uncertainties in the spectroscopically determined surface gravities require a deeper treatment. Since gravity is calculated by eliminating the difference in iron abundance derived from [Fe I/H] and [Fe II/H], the uncertainty in surface gravity is the quadratic sum of the the uncertainty in [Fe I/H] and [Fe II/H], respectively. These abundances, in turn, have sensitivities that depend on the basic physical parameters, including surface gravity; thus the uncertainty is dependent on itself. Proper uncertainty calculations, therefore, require an iterative procedure described here. The errors in [Fe I/H] and [Fe II/H] are a combination of the measurement uncertainties and the uncertainties in the physical parameters. The line measurement uncertainties in Fe I and Fe II were estimated as the standard deviation of the abundances from all Fe I and Fe II lines, respectively. Abundance sensitivities for arbitrary changes in temperature ($\pm$ 150 K), surface gravity ($\pm$ 0.12 dex) and microturbulence ($\pm$ 0.60 kms^{-1}) were determined by adjusting each parameter individually and recording the resultant difference in abundance. To determine abundance uncertainties the abundance differences must be properly normalized by the respective parameter's uncertainty. For example, in HIP3455 the total temperature uncertainty was found to be 35 K. The final abundance uncertainty introduced by the arbitrary temperature change would, therefore, be equal to the difference in abundance multiplied by $\frac{35K}{150K}$, where 35 K is the temperature uncertainty and 150 K is the arbitrary temperature change introduced to determine the temperature sensitivity. For the first calculation the uncertainties in temperature and microturbulent velocity were determined as above and the uncertainty in surface gravity was unknown, consequently its contribution to abundance uncertainty was initially ignored. Adding the measurement errors in [Fe I/H] and [Fe II/H] in quadrature with the physical parameter abundance uncertainties from temperature and microturbulence yields a first estimate for the uncertainty in the surface gravity. This gravity uncertainty can then be added in quadrature to the line measurement uncertainty, the temperature uncertainty and the microturbulent uncertainty to yield a final uncertainty for the surface gravity. The

surface gravity in the model atmosphere was adjusted until the difference in abundance between [Fe I/H] and [Fe II/H] was equal to their quadrature added uncertainties. The difference between this gravity and the spectroscopically derived gravity provides the final uncertainty in surface gravity.

A sample table of the parameter changes and their final resultant [Fe I/H] sensitivities on a given star is presented in Table 3.5. For the cases where the physical surface gravity was utilized, the uncertainty was estimated by propagating the uncertainties in the temperature, mass, apparent magnitude, parallax and bolometric corrections.

Table 3.5

Sample Abundance Sensitivity for [Fe/H]

Star	Parameter	Abundance Sensitivity
HIP3455	ΔT = $\pm$150	$\mp$0.02
	Δlog g = $\pm$0.12	$\mp$0.01
	$\Delta\zeta$ = $\pm$0.60	$\pm$0.02
	Δ <[Fe/H]>	$\pm$0.01
	Total Uncertainty in [Fe/H]	$\pm$0.03
HIP3559	ΔT = $\pm$150	$\mp$0.03
	Δlog g = $\pm$0.12	$\mp$0.00
	$\Delta\zeta$ = $\pm$0.60	$\pm$0.01
	Δ <[Fe/H]>	$\pm$0.01
	Total Uncertainty in [Fe/H]	$\pm$0.03
HIP103983	ΔT = $\pm$150	$\mp$0.04
	Δlog g = $\pm$0.12	$\mp$0.02
	$\Delta\zeta$ = $\pm$0.60	$\pm$0.01
	Δ <[Fe/H]>	$\pm$0.01
	Total Uncertainty in [Fe/H]	$\pm$0.05

Uncertainties in abundances were found by introducing arbitrary changes in T, microturbulence and surface gravity (Δ T=150 K, Δ ξ=0.60 kms^{-1}, and Δlogg=0.12 cms^{-2}). The uncertainties introduced by each of these parameter changes was added in quadrature to obtain a total parameter-based uncertainties. Measurement uncertainties were taken as

the uncertainty in the weighted mean for all lines of a given element. For elements with only a single line available, the standard deviation of all Fe I abundances was utilized as an estimate of the line measurement uncertainty. The final uncertainties in the abundances were determined by adding the parameter-based abundance uncertainties with the measurement uncertainties in quadrature.

3.2.4 Physical Parameter Comparisons:

Temperatures: Spectroscopic Versus Photometric

The temperatures for the stars in the sample were determined from photometric calibrations as well as through spectroscopic excitation balance. Do these temperatures agree? In Figure 3.4 the spectroscopic temperature is plotted versus the photometric temperature. The line represents perfect agreement between the two temperatures. Stars which lay above the line have spectroscopic temperatures which are warmer than photometric ones and stars below the line have photometric temperatures which are warmer. It can clearly be seen that the temperatures from the two techniques are equivalent within their respective uncertainties. Spearman and pearson correlation coefficients of 0.97 and 0.99, respectively, for photometric versus spectroscopic temperatures show excellent agreement in the two temperatures. There is a slight indication that spectroscopic temperatures may be systematically higher, with 66 % of the stars lying above the line, however the effects on the abundance analysis are negligible and do not change any conclusions.

Surface Gravity: Spectroscopic Versus Physical

The surface gravity was determined from Hipparcos data (i.e. physical surface gravities) and spectroscopically via ionization balance. How well do the parameters agree? In Figure 3.5, the spectroscopic surface gravity is plotted versus the physical surface gravity. The line shows the trend for the gravities being equal. The agreement between the two gravities is quite good, with spearman and pearson correlation coefficients of 0.95 and 0.99 respectively. Within their respective uncertainties, the surface gravities are equal.

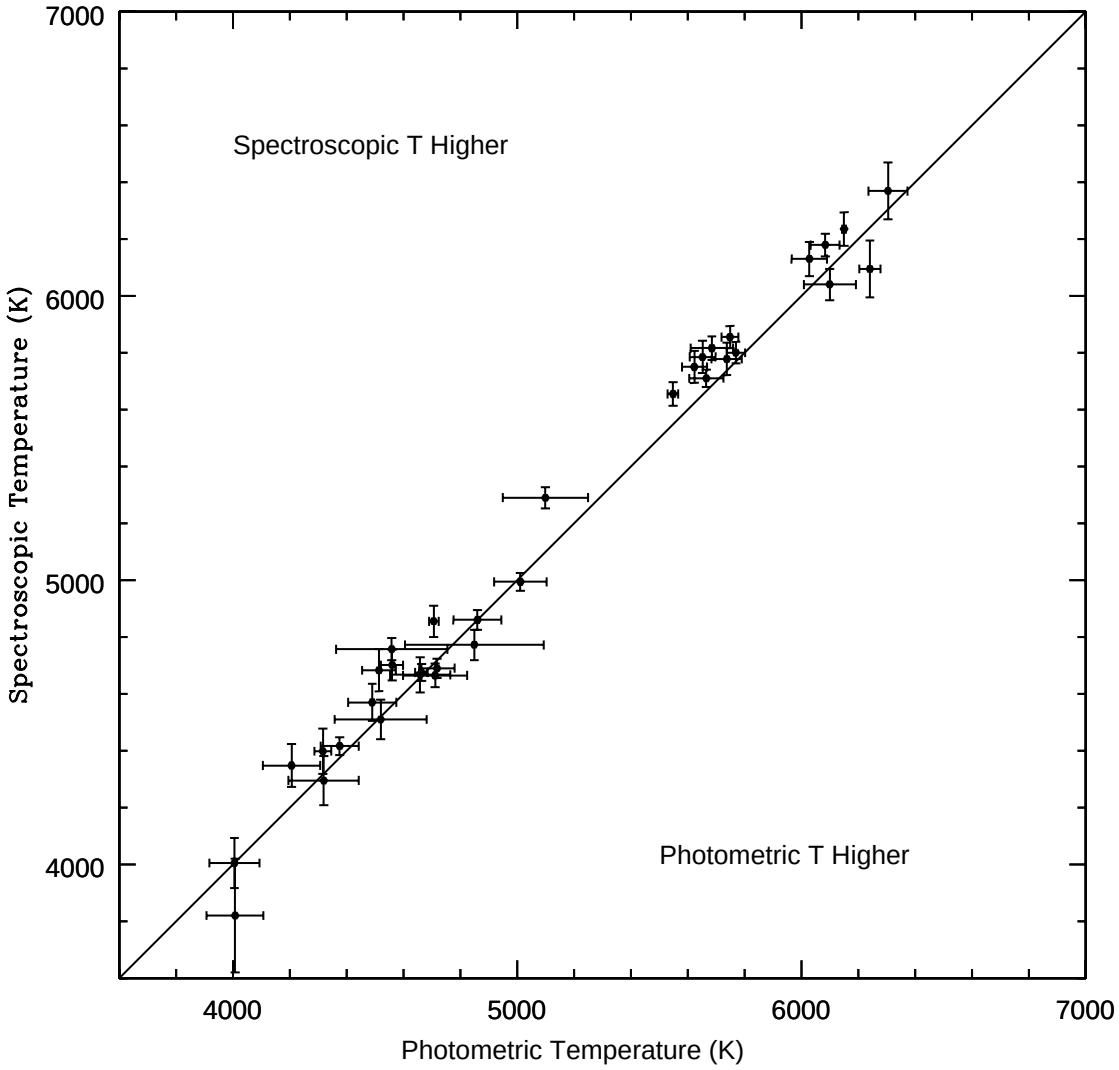

Figure 3.4 The spectroscopic temperatures are plotted versus photometric temperatures. The line is plotted to show perfect agreement between the temperature values. In general, the agreement between the temperatures is excellent, with spearman and pearson's correlation coefficients of 0.97 and 0.99, respectively.

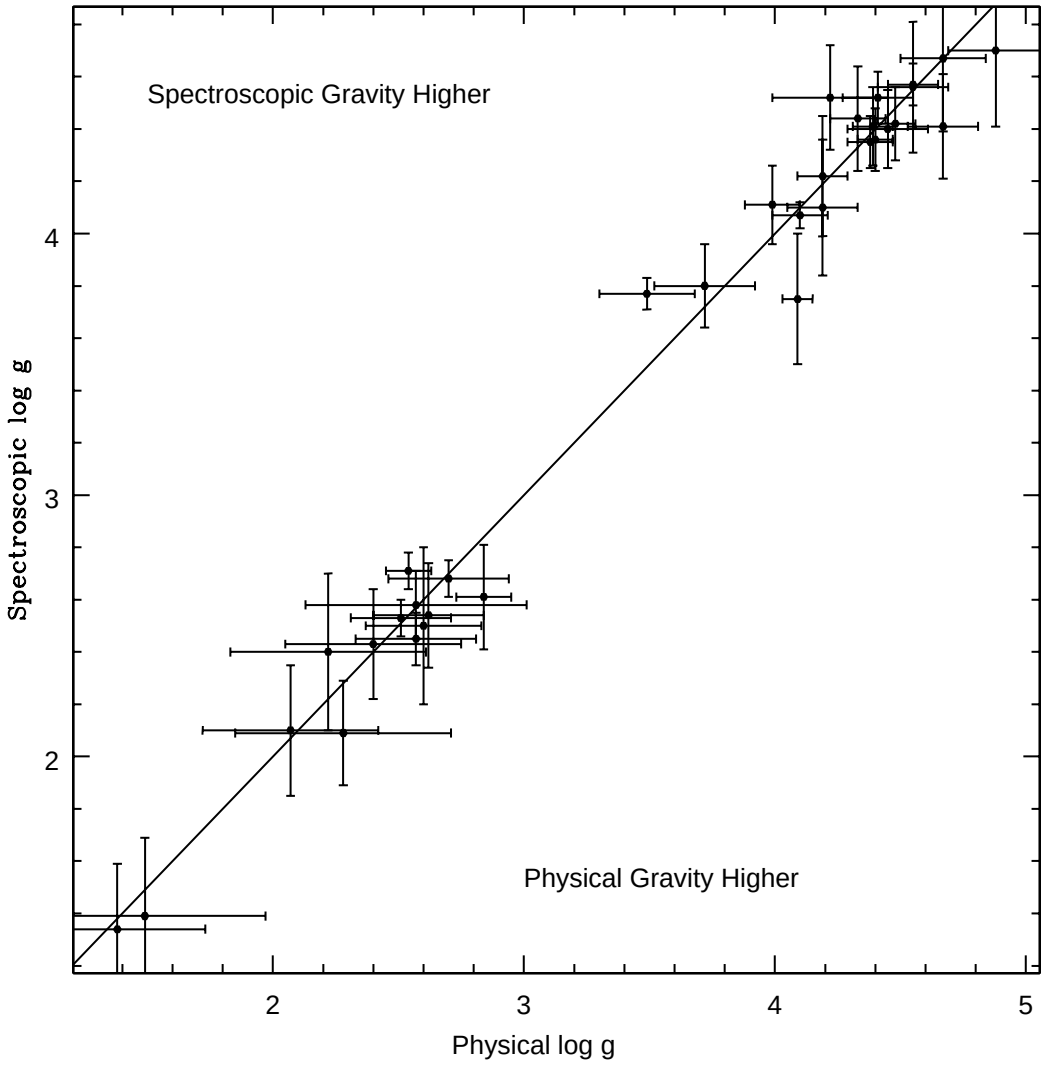

Figure 3.5 The spectroscopic surface gravities are plotted versus physical surface gravities. The line is plotted to show perfect agreement between the gravity values. In general, the agreement between the gravities is excellent, with spearman and pearson's correlation coefficients of 0.95 and 0.99, respectively.

3.3 Abundance Results

With the necessary tools developed, the question of interest can finally be explored. The primary goal of the dissertation is to determine if the kinematically defined Wolf 630 Moving Group represents a stellar population which is traced by a distinct evolutionary sequence of a single age and chemical composition. As a first step, the sample stars have been plotted in the HR diagram (Figure 3.6) to determine if they are coincident with a single evolutionary sequence. The sequence traced by the majority of stars coincides with a Yale-Yonsei isochrone (Demarque et al., 2004) of 2.7 $\pm$ 0.5 Gyr with an assumed solar metallicity. In attempting to qualitatively use ages as a constraint for establishing membership in a distinct evolutionary sequence, it will be assumed that the isochrones which fit the majority of the sample provides a reasonable estimate of the age range of a coeval group, if it indeed exists.

The abundance results are presented in both Table format, and as smoothed histograms. Metallicities ([Fe/H]) are given in Table 3.4, α elements are presented in Table 3.6, Fe peak elements are given in Table 3.7, abundances of Na, Al and Ba are shown in Table 3.8 and lithium is given in Table 3.12. Oxygen abundances were also derived, but they are presented and discussed separately. In order to visually present the abundance results, the metallicity distribution of the entire sample is presented in the form of a "smoothed histogram" in Figure 3.7 (distributions for the full sample for each element are shown in Chapter 7). This distribution has been generated by characterizing each stellar abundance by a gaussian centered on its abundance with standard deviation equal to the abundance uncertainty. Each gaussian is normalized to give a total area of 1. The normalized distributions are summed to yield a final smoothed histogram. In this manner, the distributions include uncertainties in abundances, making them useful for a visual examination of the complete sample to discern if any stars yield abundances that deviate from the sample as a whole. . The distribution is clearly not smooth. It is dominated by a near-solar metallicity peak and possesses a small peak at [Fe/H]$\sim$-0.50 and a "bump" at [Fe/H]$\sim$+0.30. The metal weak peak in particular shows that there are stars in the sample with metallicities lower than

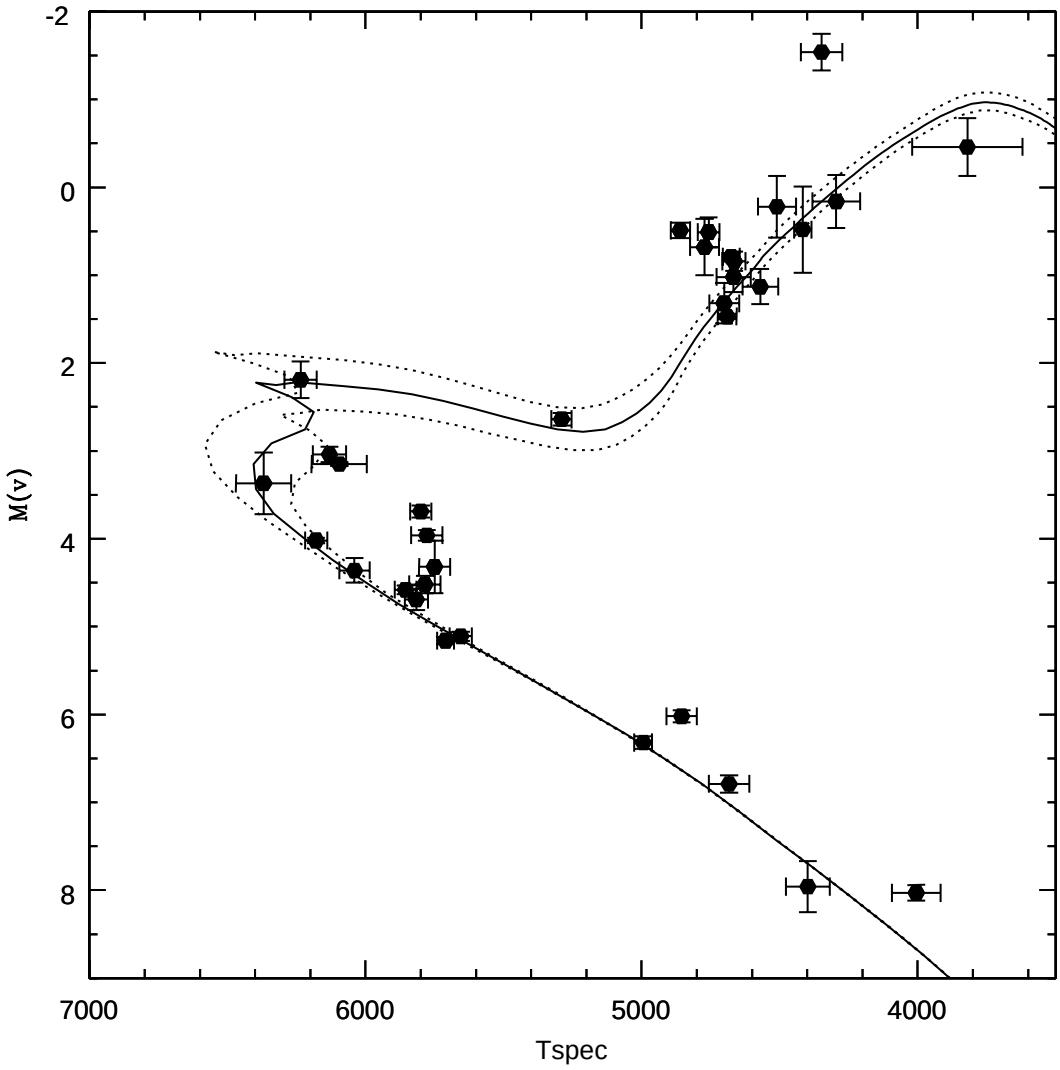

Figure 3.6 The HR diagram for the sample. Notice the reasonably good fit obtained with an isochrone age of 2.7 $\pm$ 0.5 Gyr. The stars which appear to lie above the main sequence will be explored below in constraining their membership in a chemically homogeneous Wolf group.

the dominant group metallicity, even within uncertainties. It is clear that **the Wolf 630 kinematic moving group is not characterized by a single chemical composition**. The strong peak, centered on [Fe/H]∼-0.03, however, suggests the possibility that there is a distinct chemical signature that **dominates** the group. The goal now becomes establishing a distinct subsample which is consistent with a single chemical abundance ([Fe/H]≈-0.03) and an apparent age of 2.7 Gyr, as implied by Figure 3.6.

Table 3.6

Alpha Elements

HIP	[Mg/H]	[Si/H]	[Ca/H]	[Ti/H]	[Ti2/H]
102531	0.13 ± 0.08	0.16 ± 0.08	0.08 ± 0.06	0.07 ± 0.08	0.01 ± 0.08
103983	-0.04 ± 0.09	0.02 ± 0.06	0.06 ± 0.08	0.03 ± 0.09	-0.06 ± 0.26
105341	0.00 ± 0.12			-0.17 ± 0.15	
11033	0.24 ± 0.12	0.40 ± 0.13	0.13 ± 0.14	0.04 ± 0.17	
112222	0.11 ± 0.11	0.04 ± 0.10	0.10 ± 0.08	0.06 ± 0.09	-0.01 ± 0.12
112447	-0.21 ± 0.12	-0.24 ± 0.17	0.17 ± 0.07	-0.24 ± 0.15	-0.41 ± 0.11
113622	0.18 ± 0.13	-0.01 ± 0.09	0.09 ± 0.14	0.04 ± 0.17	
114155				-0.51 ± 0.24	
114924	0.17 ± 0.10	0.10 ± 0.06	0.06 ± 0.05	0.08 ± 0.13	
12784	0.28 ± 0.12	0.04 ± 0.04	0.04 ± 0.15	0.18 ± 0.20	
13701	0.11 ± 0.09	0.07 ± 0.12	0.12 ± 0.12	-0.01 ± 0.11	-0.11 ± 0.08
14501	0.06 ± 0.11	-0.13 ± 0.15		0.01 ± 0.10	-0.05 ± 0.11
17792	-0.12 ± 0.08	-0.28 ± 0.16	0.16 ± 0.12	-0.15 ± 0.11	-0.24 ± 0.10
23852	0.03 ± 0.08	-0.04 ± 0.03	0.03 ± 0.10	-0.03 ± 0.08	0.11 ± 0.05
29525	-0.05 ± 0.07	-0.06 ± 0.06	0.06 ± 0.07	-0.06 ± 0.08	-0.08 ± 0.07
29843	0.13 ± 0.07	0.12 ± 0.04	0.04 ± 0.08	0.03 ± 0.09	0.09 ± 0.06
33671	-0.13 ± 0.08	-0.17 ± 0.04	0.04 ± 0.08	-0.18 ± 0.08	-0.25 ± 0.14
34440	0.09 ± 0.08	0.01 ± 0.08	0.08 ± 0.12	-0.20 ± 0.09	-0.06 ± 0.14
3455	0.17 ± 0.20	-0.13 ± 0.14	0.14 ± 0.10	0.00 ± 0.09	-0.06 ± 0.17
3559	-0.10 ± 0.07	-0.16 ± 0.03	0.03 ± 0.07	-0.12 ± 0.09	-0.18 ± 0.07
36732	0.30 ± 0.11	0.06 ± 0.21	0.21 ± 0.10	-0.02 ± 0.24	
3992	-0.01 ± 0.10	-0.07 ± 0.13	0.13 ± 0.11	-0.15 ± 0.15	-0.02 ± 0.11
40023	-0.01 ± 0.07	0.02 ± 0.09	0.09 ± 0.12	0.00 ± 0.13	0.04 ± 0.08
41484	0.04 ± 0.07	0.04 ± 0.02	0.02 ± 0.05	0.05 ± 0.06	-0.01 ± 0.04
42499	-0.14 ± 0.13	-0.37 ± 0.08	0.08 ± 0.14	-0.26 ± 0.06	-0.15 ± 0.12
4346	0.30 ± 0.15	0.80 ± 0.20	0.20 ± 0.14	0.43 ± 0.22	
43557	-0.08 ± 0.06	-0.05 ± 0.05	0.05 ± 0.08	-0.03 ± 0.10	-0.07 ± 0.09
45617	-0.17 ± 0.10	-0.28 ± 0.10	0.10 ± 0.16	-0.13 ± 0.22	
5027	-0.23 ± 0.10	-0.20 ± 0.20	0.20 ± 0.18	-0.06 ± 0.17	0.09 ± 0.17

Table 3.6 – Continued

HIP	[Mg/H]	[Si/H]	[Ca/H]	[Ti/H]	[Ti2/H]
50505	-0.06 ± 0.08	-0.16 ± 0.04	0.04 ± 0.08	-0.07 ± 0.09	0.00 ± 0.09
5286	0.27 ± 0.10	0.25 ± 0.11	0.11 ± 0.19	0.27 ± 0.15	0.37 ± 0.00
53229	-0.04 ± 0.09	-0.01 ± 0.20	0.20 ± 0.07	-0.15 ± 0.10	-0.03 ± 0.08
53465	0.13 ± 0.11	0.00 ± 0.19	0.19 ± 0.22	-0.10 ± 0.22	0.22 ± 0.09
6732	0.10 ± 0.10	-0.10 ± 0.14	0.14 ± 0.13	-0.01 ± 0.12	

Table 3.7

Fe Peak Elements

HIP	[Cr/H]	[Mn/H]	[Ni/H]
102531	-0.02 ± 0.09	-0.14 ± 0.05	0.05 ± 0.05
103983	-0.06 ± 0.11	-0.25 ± 0.17	-0.02 ± 0.08
105341		-0.20 ± 0.12	
11033	-0.01 ± 0.10		0.23 ± 0.19
112222	-0.01 ± 0.13	-0.25 ± 0.09	0.05 ± 0.13
112447	-0.35 ± 0.15	-0.75 ± 0.15	-0.28 ± 0.14
113622	0.03 ± 0.19	0.03 ± 0.20	0.22 ± 0.26
114155	-0.61 ± 0.20	-0.62 ± 0.09	-0.62 ± 0.14
114924	0.21 ± 0.07	-0.18 ± 0.09	0.06 ± 0.06
12784	-0.02 ± 0.14	0.24 ± 0.09	0.16 ± 0.22
13701	-0.11 ± 0.05	-0.02 ± 0.11	-0.04 ± 0.10
14501	-0.11 ± 0.11	-0.31 ± 0.07	-0.12 ± 0.08
17792	-0.60 ± 0.05	-0.54 ± 0.11	-0.44 ± 0.14
23852	-0.20 ± 0.08	-0.44 ± 0.09	-0.19 ± 0.06
29525	0.03 ± 0.07	-0.14 ± 0.05	-0.09 ± 0.04
29843	0.09 ± 0.09	0.03 ± 0.07	0.11 ± 0.09
33671	-0.33 ± 0.07	-0.61 ± 0.08	-0.27 ± 0.12
34440	-0.31 ± 0.05	-0.05 ± 0.08	-0.11 ± 0.08
3455	-0.04 ± 0.20	0.00 ± 0.09	0.04 ± 0.09
3559	-0.29 ± 0.07	-0.50 ± 0.04	-0.24 ± 0.09
36732	-0.03 ± 0.15	0.28 ± 0.11	0.29 ± 0.10
3992	-0.18 ± 0.12	-0.17 ± 0.08	-0.11 ± 0.09
40023	-0.08 ± 0.08	-0.13 ± 0.07	-0.10 ± 0.07
41484		0.00 ± 0.06	0.00 ± 0.05
42499	-0.61 ± 0.03	-0.72 ± 0.06	-0.77 ± 0.11
4346	0.44 ± 0.11	0.45 ± 0.14	0.54 ± 0.23
43557	-0.08 ± 0.07	-0.19 ± 0.06	-0.10 ± 0.06
45617	-0.13 ± 0.10	-0.17 ± 0.07	-0.24 ± 0.09
5027	±	-0.26 ± 0.11	-0.18 ± 0.07

Table 3.7 – Continued

HIP	[Cr/H]	[Mn/H]	[Ni/H]
50505	-0.18 ± 0.09	-0.26 ± 0.07	-0.21 ± 0.10
5286	0.39 ± 0.19	0.18 ± 0.11	0.31 ± 0.10
53229	-0.28 ± 0.10	-0.11 ± 0.13	0.01 ± 0.18
53465	-0.14 ± 0.09	-0.05 ± 0.19	0.01 ± 0.13
6732	-0.10 ± 0.12	0.04 ± 0.10	0.03 ± 0.13

Table 3.8

Other Abundances

HIP	[Na/H]	[Al/H]	[Ba/H]
102531	0.18 ± 0.03	0.07 ± 0.08	-0.01 ± 0.13
103983	0.05 ± 0.05	-0.03 ± 0.06	0.10 ± 0.11
105341	-0.43 ± 0.09	0.01 ± 0.19	
11033	0.23 ± 0.18	0.25 ± 0.13	
112222	0.16 ± 0.12	-0.05 ± 0.09	-0.07 ± 0.13
112447	-0.23 ± 0.11	0.17 ± 0.09	-0.46 ± 0.12
113622		0.05 ± 0.22	-0.04 ± 0.21
114155	-0.05 ± 0.08	-0.07 ± 0.11	
114924	0.20 ± 0.12	0.07 ± 0.06	-0.07 ± 0.11
12784	0.18 ± 0.12	0.19 ± 0.07	0.01 ± 0.14
13701	-0.05 ± 0.12	0.07 ± 0.12	
14501	-0.01 ± 0.09	0.14 ± 0.14	-0.19 ± 0.12
17792		-0.12 ± 0.04	-0.59 ± 0.11
23852	-0.21 ± 0.03	-0.01 ± 0.07	-0.31 ± 0.08
29525	-0.10 ± 0.04	-0.12 ± 0.03	0.10 ± 0.05
29843	0.16 ± 0.06	0.09 ± 0.08	0.05 ± 0.14
33671	-0.25 ± 0.05	-0.32 ± 0.08	-0.12 ± 0.07
34440	-0.02 ± 0.04	-0.02 ± 0.04	-0.19 ± 0.15
3455	0.20 ± 0.20	0.07 ± 0.07	
3559	-0.29 ± 0.06	-0.18 ± 0.04	-0.29 ± 0.05
36732	0.24 ± 0.13	0.16 ± 0.17	-0.03 ± 0.17
3992	0.07 ± 0.08	0.11 ± 0.15	0.04 ± 0.14
40023	0.00 ± 0.05	-0.01 ± 0.15	-0.17 ± 0.08
41484	0.05 ± 0.04	0.01 ± 0.04	0.08 ± 0.06
42499	-0.42 ± 0.14	-0.32 ± 0.08	
4346	0.36 ± 0.16	0.40 ± 0.08	
43557	-0.07 ± 0.04	-0.04 ± 0.03	-0.03 ± 0.09
45617	-0.09 ± 0.11	-0.13 ± 0.04	-0.25 ± 0.19
5027	-0.41 ± 0.14	-0.25 ± 0.09	-0.05 ± 0.13

Table 3.8 – Continued

HIP	[Na/H]	[Al/H]	[Ba/H]
50505	-0.16 ± 0.03	-0.12 ± 0.04	-0.26 ± 0.07
5286	0.26 ± 0.12	0.19 ± 0.17	
53229	0.07 ± 0.08	0.03 ± 0.09	
53465	-0.01 ± 0.14	0.12 ± 0.05	0.06 ± 0.13
6732	0.02 ± 0.10	0.14 ± 0.07	-0.13 ± 0.11

Table 3.9

Lithium

HIP	LogN(Li)
3559	2.45 ± 0.03
5027	≤ -0.20
5286	≤ 0.70
14501	≤ 0.30
23852	2.00 ± 0.04
29525	2.03 ± 0.02
29843	≤ 1.60
33671	2.61 ± 0.05
41484	1.93 ± 0.04
42499	≤ 1.09
43557	≤ 1.50
45617	≤ 0.60
50505	≤ 0.50
102531	1.90 ± 0.07
103983	1.90 ± 0.07
105341	≤ -0.25
112447	2.30 ± 0.07
114924	2.75 ± 0.06
112222	≤ 1.22

3.4 A Note on Field Star Contamination

Since moving groups are observed against a foreground and background of random field stars, it is prudent to first compare the metallicity distribution of the sample to that of a

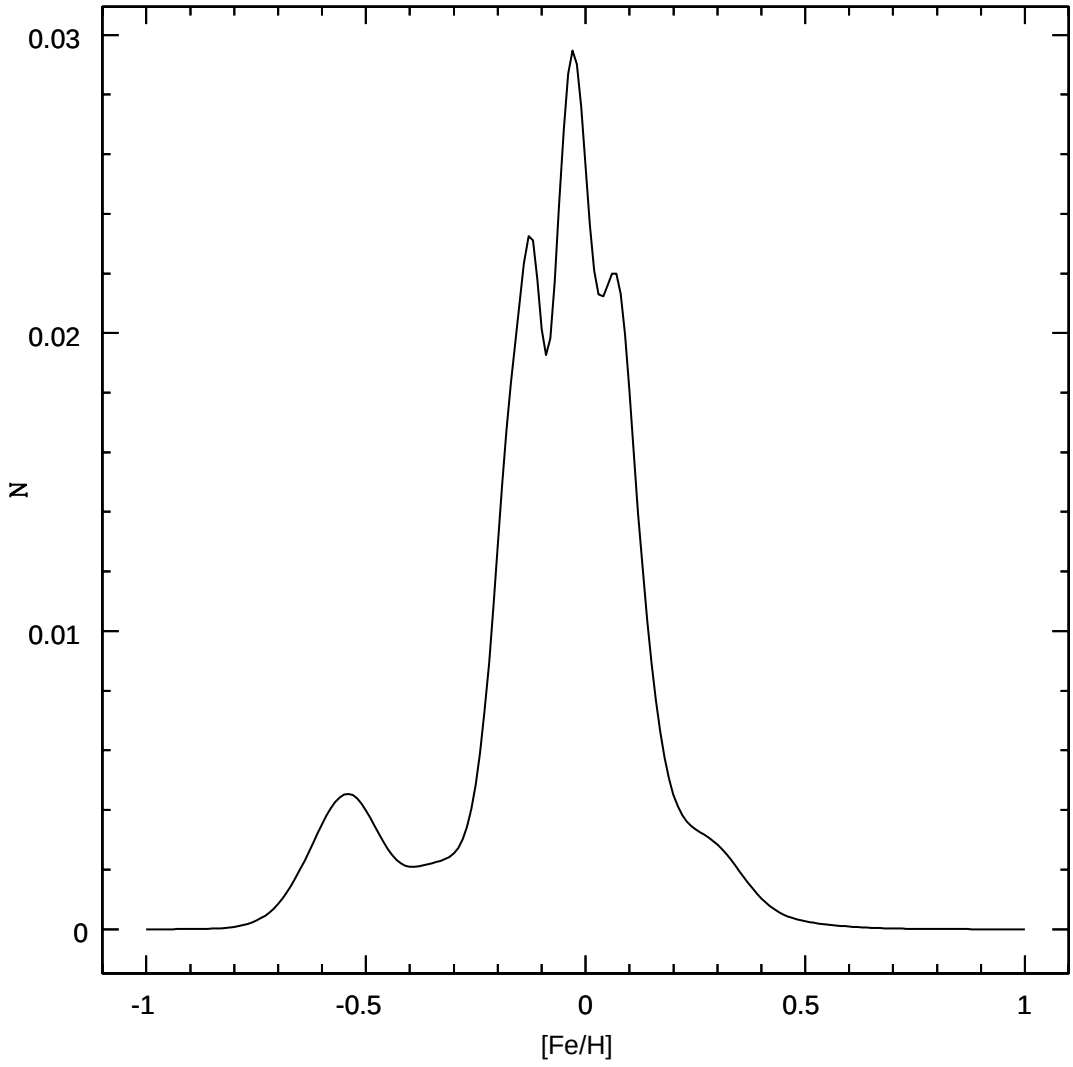

Figure 3.7 The metallicities of each individual star are plotted as gaussians with central peaks at a given star's metallicity and σ equal to uncertainty in the [Fe/H]. The gaussians are normalized to unit area and summed to yield the smoothed abundance histograms. The peak at [Fe/H]$\sim$-0.50 is from 3 low metallicity stars and the bump at [Fe/H]$\sim$0.30 is from 2 high metallicity stars. This is discussed in more detail in the text.

random population of field stars to determine the probability that the observed distribution would be observed from a random field star sample. To this end, the volume limited study of the solar neighborhood of Nordström et al. (2004) provides a sample to represent the photometric metallicity distribution of field stars.

In order to compare the distributions, a KS-Test between the Wolf 630 sample and the Nordstrom sample has been performed. The distributions can be found in Figure 3.8. The KS test results in rejecting the hypothesis of the Wolf moving group and a random field star sample being drawn from the same parent population with 95 % confidence.

As an additional comparison, 10000 random samples of 34 stars each have been drawn from the Nordstrom catalog. KS tests were performed to compare the Wolf 630 sample with each of the random 34 field star samples. The results of these tests are presented in a histogram in Figure 3.9. The number of KS tests between the dissertation sample and a random field star sample is plotted on the yaxis while the resultant probability is given on the xaxis. Notice that over 50 % of the KS tests yield a probability of 10 % or lower for the Wolf sample being drawn from a random field star sample and over 80 % of the tests yield a probability of 80 % or lower for the Wolf sample being drawn from a random sample.

These results support the conclusion that the Wolf 630 sample is not a random selection of field stars under the reasonable assumption that the Nordstrom sample is representative of the field.

3.5 Approach to Chemically Tagging

Having established that the entire sample cannot be characterized by a single chemical abundance and the metallicity distribution of the Wolf sample is not likely to be drawn from a random selection of field stars. The focus is now to link populations of stars together according to common abundances and identify a dominant chemical signature, with the goal of identifying a subsample of stars that represents an evolutionary sequence of a single chemical composition and age. The basic approach taken is to:

1) Eliminate stars that are clearly outliers, using arguments based on extreme abundances,

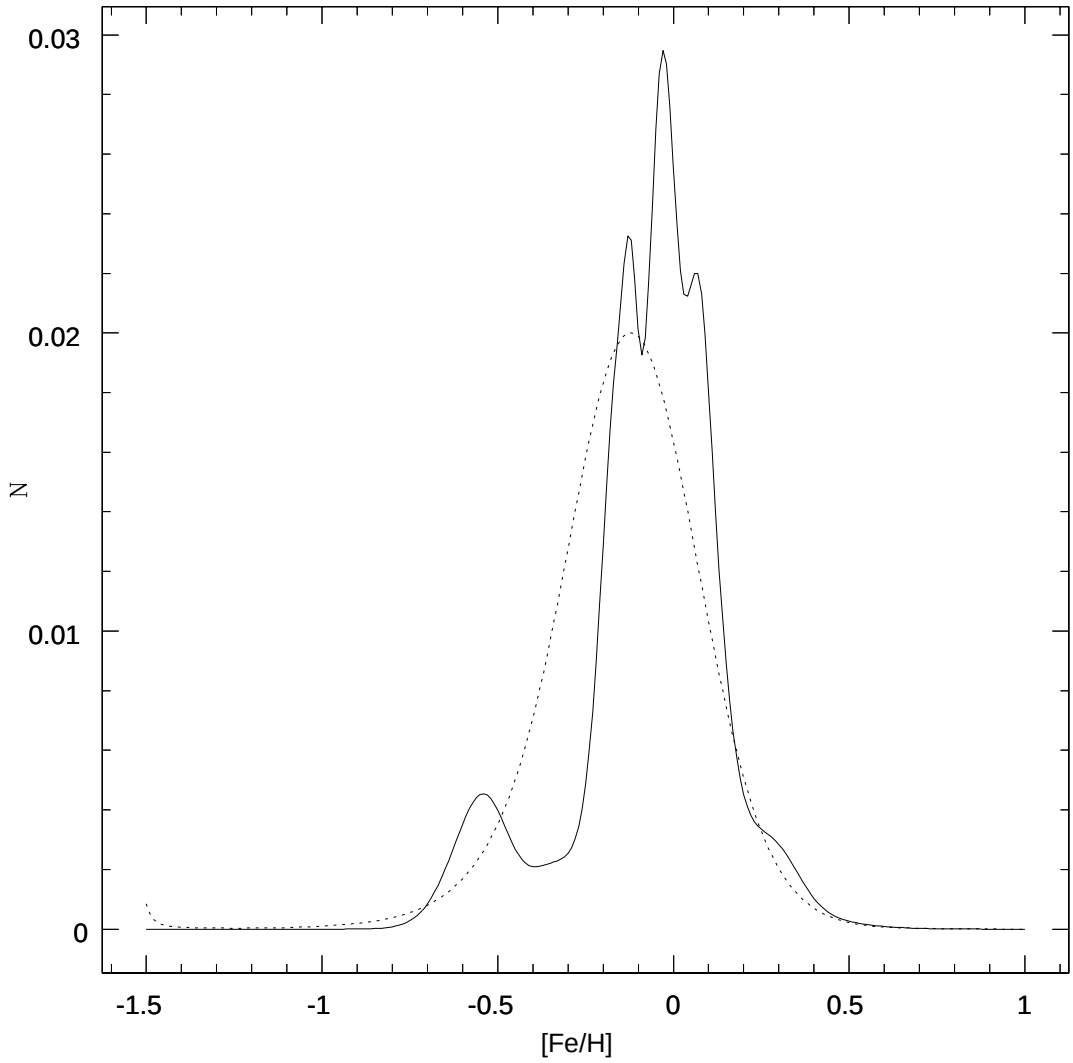

Figure 3.8 A smoothed metallicity histogram for the Nordstrom sample of 14000 field stars (dotted line) for comparison to the Fe/H histogram of the Wolf 630 sample (solid line). The histograms are compared with a KS test, yielding a KS probability of 5 % for the histograms being drawn from the same parent population.

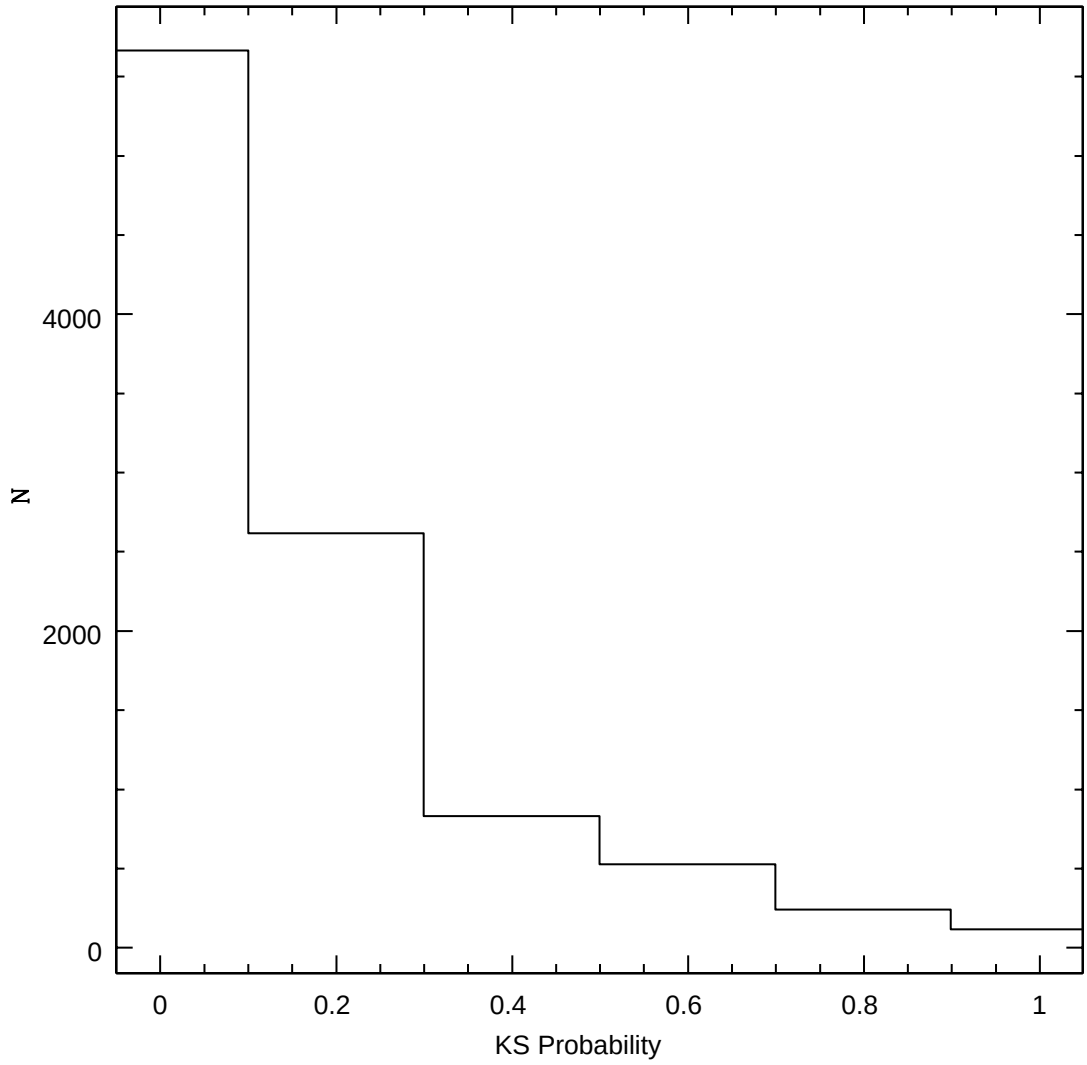

Figure 3.9 The 14000 field star sample of Nordstrom was used to generature metallicity distributions for 10000 random field star samples, each of 34 stars. A KS test was performed to compare each random field star sample with the Wolf 630 sample. The resultant KS probability for each test is plotted in histogram form.

evolutionary state (inferred from HR Diagram positions, lithium abundance, chromospheric acitivities and surface gravities) or a combination thereof. These members will be classified as unlikely members of a homogeneous group.

2) Establish a subsample that is characterized by a dominant [Fe/H], if it exists. Stars with an [Fe/H] in range of this dominant metallicity will be classified as either "possible" or "likely" members of a chemically dominant subset. The final distinctions between "possible" and "likely" will be made based on evolutionary status and additional abundance information inferred from lithium, alpha elements and iron peak elements. Particular interest is paid to the metallicity, [Fe/H], as it is considered the most well determined abundance, primarily due to the quality and size of the Fe line sample.

The quantitative constraint adopted for determining consistency with a dominant abundance was to require that a star's abundance, within its uncertainty, rests within an abundance band centered on the weighted mean abundance of stars in the sample. The width of this band is conservatively taken to be 3 times the uncertainty in the weighted mean. These plots were generated in an iterative fashion where whenever a star was determined to be an "unlikely" member of a dominant chemical group it was removed from the plot and a new weighted mean and band size was found. In this manner, a common abundance for the sample was converged to for each element in the sample. A sample of the full sample band plot is given in Figure 3.10. There are outliers that clearly don't rest within the dominant abundance band. With these "unlikely" members removed, the group abundance is found to converge to a single value. With the exception of Figure 3.10, the final band plots, comprised of the possible and likely members are presented here. A sample final abundance band is presented in the text in Figure 3.11, where [Fe/H] is plotted versus temperature. The solid line gives the weighted mean [Fe/H] while the dotted lines give the 3-σ uncertainties in this mean, i.e. the abundance band. Similar plots for all other elements are presented in chapter 7.

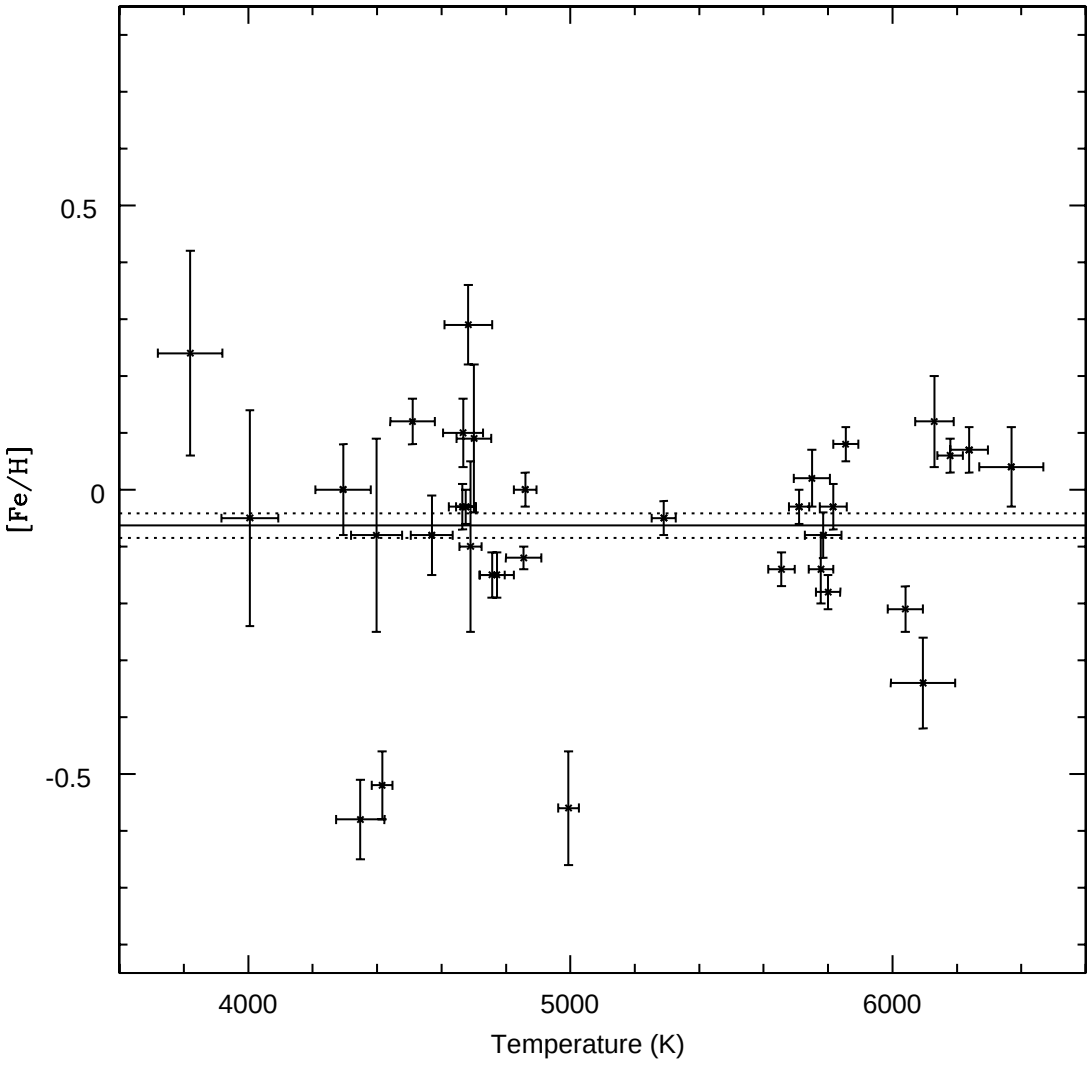

Figure 3.10 The [Fe/H] for the full sample of stars is plotted versus temperature. The solid line gives the weighted mean of the sample while the dotted lines are 3-σ deviations from this mean. If a star rests within the dotted lines (i.e. the abundance band) within its respective uncertainty, then it is considered homogeneous with the dominant sample. Those stars which rest far outside the abundance band in the full sample plot are iteratively removed as unlikely members until convergence to a dominant abundance is achieved.

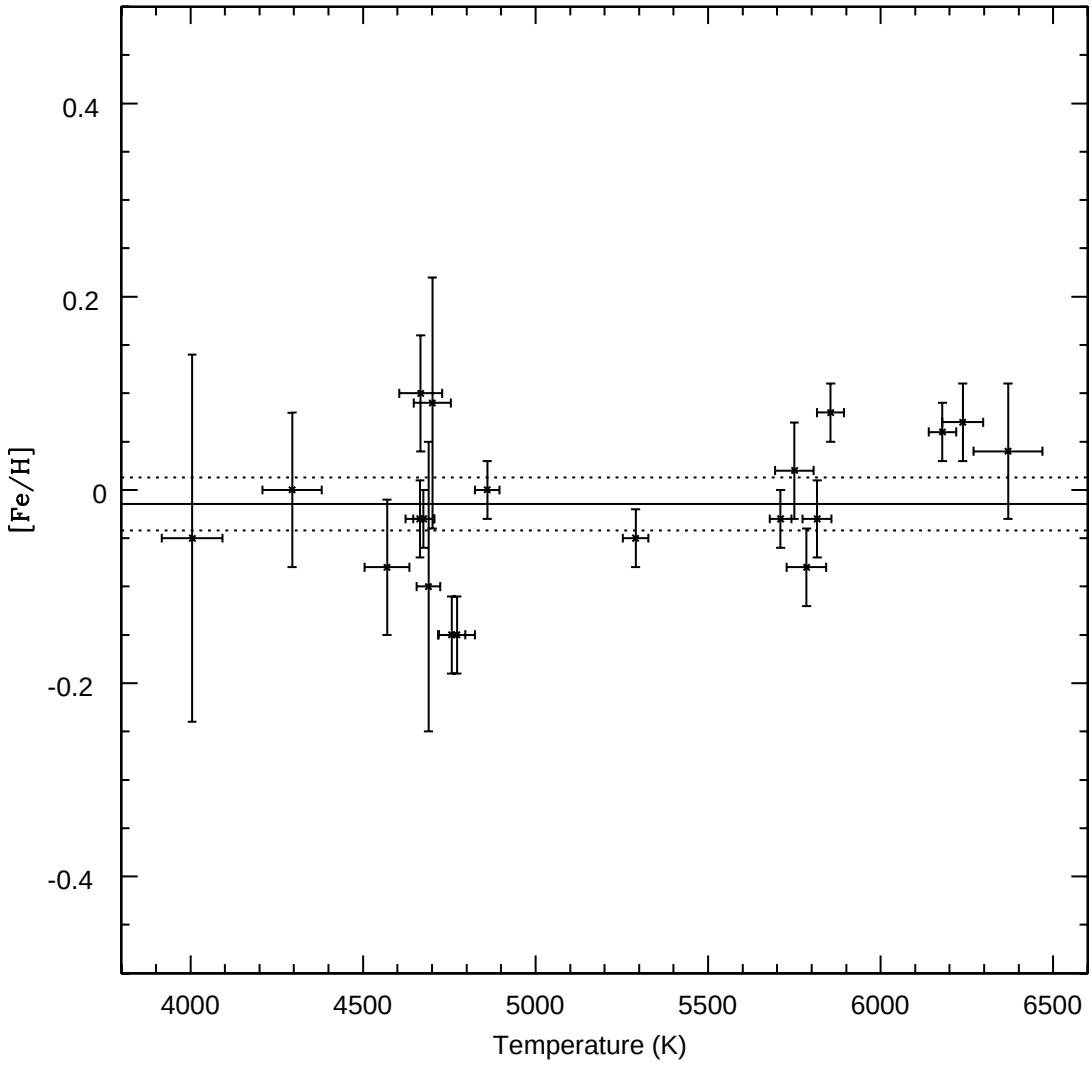

Figure 3.11 The [Fe/H] for the stars that are labeled possible or likely members of a dominant homogeneous sample are plotted versus temperature. The solid line gives the weighted mean of the sample while the dotted lines are 3-σ deviations from this mean. If a star rests within the dotted lines (i.e. the abundance band) within its respective uncertainty, then it is considered homogeneous with the dominant sample.

3.5.1 Unlikely Members

The first step was to remove the stars which were clearly atypical of the overall group and therefore begin converging to a dominant chemical signature. In establishing these "unlikely" members, the smoothed abundance distributions provide a useful visual tool in pinpointing stars with possibly extraneous abundances. Consider Figure 3.7 and notice the relatively clear peak at [Fe/H]=-0.53. A similar peak appears across multiple element distributions, including Cr, Mn, Ni and Ba. Upon inspecting the abundances, the same four stars appear to be responsible for all of these low abundance peaks/enhancements, and indeed the four stars were found to lie outside of the group abundance bands. They are identified in the discussion of individual stars.

Continuing a visual examination of the smoothed [Fe/H] distribution, the other possible feature of note that may reveal stars with extraneous abundances, compared to the group trend, is the bump at [Fe/H]$\sim$0.30. The bump appears as a similar enhancement in Ni, Cr, Mn, Al, Na and Mg. Inspecting the abundance band plots showed that these enhancements were signatures of two metal rich stars in the sample, also identified in the individual star discussions.

This visual analysis from examining the abundance distributions served as a guide for identifying the clearly unlikely members. The full analysis examined each star individually, utilizing abundances and information on evolutionary status (inferred from chromospheric activities, isochrone ages and surface gravities) to classify each star in its appropriate category (unlikely, possible or likely). Abundance information alone is used to constrain giant star membership in a dominant chemical group, as their evolutionary status is well determined. Greater care was necessary in analyzing the dwarfs and subgiants, as their evolutionary statuses were less clear than the giant stars. Many of the dwarfs lay above the main sequence, leading to the question of if they are pre main sequence objects. The warmer dwarfs that reside above the main sequence are not only possibly pre-main sequence stars, but could also potentially be subgiants. Consequently a diagnostic will be needed to constrain evolutionary status for these dwarf and subgiant stars. Since the lithium abundances

will be utilized for this purpose for many of the individual stars below, the presentation of the results (Figure 3.12) are described here to avoid unnecessary repetition. The figure gives the absolute lithium abundance versus effective temperature for a sample of dwarf stars in the Pleiades, Hyades, NGC752 and M67. The lithium abundances of the sample stars are plotted with each cluster: filled hexagons are dwarfs, filled triangles are upper limits for dwarfs, open hexagons are subgiants and open triangles are upper limits for subgiants. General ages are given for each of the respective clusters, with the Pleiades trend being used as a baseline to indicate that a star is likely to be young (i.e. if a star has a lithium abundance which rests in the Pleiades lithium abundance trend it is likely a young star). These abundances will be extremely valuable in constraining the evolutionary status of stars which appear to be on the pre-main sequence (i.e. dwarf stars above the ZAMS).

HIP 3559: T=5800 logg=4.07 ξ=1.27 [Fe/H]=-0.18

This star resides above the ZAMS in the HR diagram leading to the question of if it is a pre-main sequence dwarf, or a post-main sequence subgiant. Ca II H and K measurements indicate an inactive chromosphere (logR'$_{HK}$=-5.16). From this, the activity-age calibrations of Mamajek & Hillenbrand (2008) suggest an age of 9.4 $\pm$ 2.7 Gyr, indicating the HR diagram position is not a result of being a PMS star. Indeed, Holmberg et al. (2007) derive an ischrone age, from Padova isochrones (Girardi et al. (2000), Salasnich et al. (2000)), of 7.6 Gyr; again, clearly not PMS. Fitting the position of this star using Yale-Yonsei isochrones, it appears to lie near the turnoff for a 6.8 $\pm$ 0.4 Gyr isochrone. In addition, the spectroscopic surface gravity (log(g)=4.07) is consistent with subgiant status. In order to determine if the lithium abundance (logN(Li)=2.45) is consistent with a subgiant abundance a rough consistency check has been utilized. The basic approach to determine the viability of a subgiant having the observed abundance is to first obtain a reasonable estimate of the lithium abundance this star may have possessed as a ZAMS dwarf and compare the amount of lithium dilution that is observed with theoretical calculations. In order to obtain an estimate of the dwarf abundance that this star may have possessed, an estimate of the

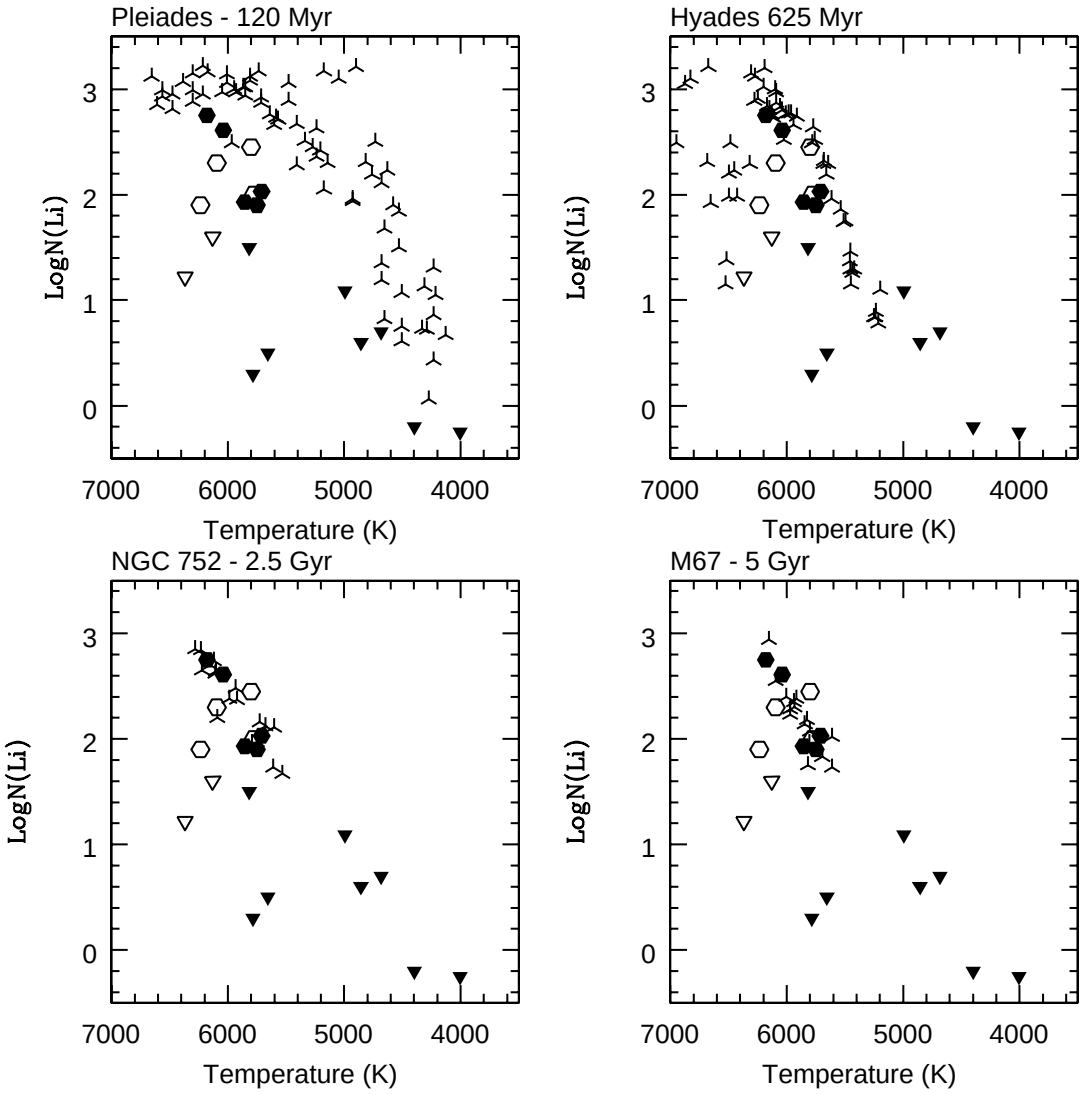

Figure 3.12 Lithium abundances for the Pleiades (top left-King et al. (2000)), the Hyades (top right-Balachandran (1995), NGC752 (bottom left-Sestito et al. (2004)) and M67 (bottom right-Jones et al. (1999) and the Wolf 630 stars of this dissertation (filled points are for dwarfs, open points are for subgiants and hexagons and triangles are detections and upper limits, respectively). Specific abundances for individual stars are discussed in more detail in the text.

star's temperature during its dwarf stage of evolution must first be obtained. Assuming that the star is a 6.8 Gyr subgiant, the isochrone yields a mass of 1.10 ± 0.2 $M_{\odot}$. Since the mass uniquely determines its subsequent evolution (ala the Russell-Vogt theorem), the mass provides a diagnostic for describing the star at any age. Treating the Pleiades age as an estimate for representing a ZAMS population, a dwarf-like temperature of 6158 K for a star of this mass was determined from a Yale isochrone of 120 Myr (the approximate age of the Pleiades). Therefore, an estimate of the lithium abundance that HIP 3559 may have possessed as a dwarf is found by finding the lithium abundance of a Pleiades dwarf with a temperature of 6158 K. This yields an approximate abundance of logN(Li)∼3.00, which is consistent with predicted lithium dilution calculations for a 1.11 $M_{\odot}$ at an age of ∼ 6.8 Gyr, performed using the Clemson-American University of Beirut stellar evolution code. HIP3559 is therefore removed from consideration as a member of a 2-3 Gyr Wolf group. Instead, it is assumed that this is an ∼ 6.8 Gyr subgiant.

HIP 4346: T=3820 logg=1.39 ξ=1.33 [Fe/H]=0.24

The absolute metallicity of [Fe/H]=0.24 ± 0.18 is high compared to the group trend, and indeed rests outside of the abundance band for the full sample. It is one of the stars responsible for the metallicity bump at [Fe/H]=0.30 in Figure 3.7. In investigating the other abundances, this star is clearly metal rich across all elements. Within the uncertainties, it does not match the abundance bands for any elements. Considering this clear metal richness across all abundances, this star is considered an unlikely member of a dominant Wolf 630 moving group.

HIP 5027: T=4398 logg=4.70 ξ=0.00 [Fe/H]=-0.08

Hip 5027 has an Fe abundance which is consistent with inclusion into a chemically homogeneous group. Examining the abundances of other elements, Na, Al, Mn, Ni, Mg and Si all rest outside of the abundance band for the full sample. Examining the lithium upper limit of logN(Li) ≤ -0.20 perhaps places the star in the trend traced by the Pleiades, however the significant spread in lithium abundances as a function of decreasing temperature and

the low sample of stars populating the cool end of the Pleiades lithium abundances make a firm conclusion difficult to draw. With the majority of elements disagreeing with the overall abundance trends of the entire sample, this star is classified as an unlikely member of a chemically dominant group.

HIP 5286: T=4683 logg=4.56 ξ=0.54 [Fe/H]=0.29

HIP 5286 is a member of the metallicity "bump" at [Fe/H]=$\sim$0.30 in Figure 3.7. In examining the HR diagram, HIP 5286 rests above the main sequence. The lithium upper limit of logN(Li)$\leq$0.70 which places the star clearly outside of the Pleiades trend suggesting that it is not a young, PMS star. Coincidence with the other open cluster trends is uncertain as the literature lithium abundances do not extend to sufficiently cool temperatures, indicating the need for lithium abundance determinations in cool stars in intermediate age open clusters. Examining the abundances, HIP 5286 is clearly a metal rich star with [Fe/H]=0.29 $\pm$ 0.07, well outside of the dominant abundance band. Indeed, this metal richness is confirmed across all abundances. Noting the metal richness across multiple elements, this star as an unlikely member of a chemically dominant group.

HIP 11033: T=4510 logg=2.40 ξ=1.60 [Fe/H]=0.12

The metallicity of HIP 11033 ([Fe/H] = 0.12 $\pm$ 0.04) places this star outside of the metallicity band used to constrain homogeneity in abundance. In examining abundances for other elements, this star is seen to reside outside of the homogeneous bands for Al, Mg and Si and it barely resides inside the band for Na. There were no abundances determined for Mn, Ba, Ti 2. This leads HIP 11033 to be labeled as an unlikely member of a dominant chemical group.

HIP 17792: T=4416 logg=2.09 ξ=1.50 [Fe/H]=-0.52

The metallicity of HIP 17792 is low, being -0.52 $\pm$ 0.06. It is one of the stars comprising the low metallicity bump in Figure 3.7. This low metallicity extends across all the Fe peak elements. The Al abundance ([Al/Fe]=0.40) is of note in that this star

shows similar enhancements to those seen by Schuler et al. (2009) in a sample of Hyades giants. This points, to a pattern of high Al abundances for giant stars. Making note of the anomalous Al abundance, the low abundances of Fe and Fe peak elements lead to the conclusion that this star is an unlikely candidate for being part of a homogeneous Wolf 630 subsample.

HIP 23852: T=5778 logg=4.22 ξ=1.22 [Fe/H]=-0.14

This star appears to reside above the ZAMS leading to the question of it is a pre-main sequence dwarf or subgiant. The literature suggests an isochrone age of 8.8 Gyr for the star (determined from Padova isochrones) (Nordström et al., 2004). Subsequent fitting with Yale isochrones places this star on the turnoff of an isochrone with an age of 7.9 $\pm$ 0.07 Gyr. The spectroscopic surface gravity of the star (log(g)=4.22) is not inconsistent with a subgiant classification. Using a stellar mass of 1.08 $M_{\odot}$, inferred by assuming subgiant status on an isochrone of 7.9 Gyr, the ZAMS temperature of a star with this mass would have been 6052 K. The ZAMS lithium abundance, inferred from the Pleiades trend of Figure 3.12, logN(Li)=3.00, suggests a factor of 10 lithium depletion, not inconsistent with theoretical calculations. The lithium abundance of logN(Li)=2.00, assuming that this is a dwarf star, appears consistent with the trend traced by M67 which may imply the star is a 5-6 Gyr dwarf, but certaintly not a pre-main sequence star. It seems more likely that the position of HIP 23852 above the main sequence is a result of this star being a 7.9 Gyr subgiant. Regardless of evolutionary state, the metallicity lays outside of the abundance band used for judging homogeneity of the sample. The Fe peak elements, Na, Al and Ba all reside outside of the dominant abundance bands. This star is, therefore, not considered a member of a chemical moving group.

HIP 29843: T=6130 logg=4.11 ξ=1.52 [Fe/H]=0.12

Hip 29843 has an upper limit lithium detection of logN(Li)$\leq$ 1.60. Assuming the star is a group member, an isochrone mass of 1.43 $\pm$ 0.02 $M_{\odot}$ is found. Using this mass to determine the ZAMS temperature of the star yields a T_{ZAMS}=6678 K. This temperature,

when compared to the lithium plots of Figure 3.12, would have placed this star in the well established lithium dip when it was a dwarf. Currently, as a subgiant that has emerged from the lithium dip, the lack of lithium suggests that the deepening convection zone in the subgiant has not brought lithium back to the surface. This appears consistent with the findings of Balachandran (1990) who similarly saw little diffusion of lithium to the surface in subgiants emerging from the lithium dip in M67. The metallicity of the star ([Fe/H]=0.12 ± 0.08) appears to be somewhat high compared to the peak of the sample, and, indeed it rests outside of the metallicity band. This star also resides outside of the abundance bands for Si, Na, Cr and Mn. The lack of clear homogeneity across multiple elements lead HIP 29843 to be considered an unlikely member of a dominant metallicity sample.

HIP 33671: T=6040 logg=4.40 ξ=1.38 [Fe/H]=-0.21

The metallicity of HIP 33671 is [Fe/H]=-0.21 ± 0.04. This places the star well outside of the apparent dominant metallicity band. The metal poor nature applies across all other elements, with the star not resting within any abundance bands. HIP 33671 is unlikely to be part of a dominant chemical Wolf group.

HIP 42499: T=4994 logg=4.41 ξ=0.59 [Fe/H]=-0.56

HIP 42499 is a member of the apparently metal weak peak in the full sample metallicity distribution (Figure 3.7). An upper limit lithium abundance of logN(Li)$\leq$1.09 potentially places this star in the Hyades trend, however the chromospheric activity (logR'$_{HK}$=-4.98) is much lower than the activity trend for the Hyades, suggesting it is older than the Hyades. With an [Fe/H]=-0.56 ± 0.10 and consistent metal deficiency evinced across all elements this star is classified as an unlikely member of a chemically dominant group.

HIP45617 T=4855 logg=4.35 ξ=1.01 [Fe/H]=-0.12

Examining the HR diagram position, the star appears to reside above the main sequence. The lithium upper limit (logN(Li) $\leq$ 0.60) shows that the star does not reside within the Pleiades lithium abundance trend, suggesting it is it not on the pre-main sequence. The

activity of logR'$_{HK}$=-4.60, from the Ca II H and K survey of the solar neighborhood of D. Soderblom (private communication), would place the star below the activity trend of the Hyades, qualitatively suggesting that a Hyades age would be a reasonable lower limit, again suggesting that the residence above the main sequence is not a result of being a pre-main sequence star. The surface gravity is somewhat low for a dwarf star. A possible explanation is that overionization, as observed in many cool cluster dwarfs, is yielding spuriously low surface gravities. With a greater number of atoms in ionized states, the gravity would have to be artificially lowered to obtain ionization balance. This, however, seems unlikely in that excellent agreement is seen between the spectroscopic gravity (log g=4.35) and the physical gravity (log g=4.38). It is noted that the surface gravity is, perhaps, unusually low. The star's [Fe/H]=-0.12 ± 0.02 is inconsistent with it being a member of the dominant metallicity distribution. Additionally, it does not appear to lay well within the abundance bands for any other elements. The poor agreement with the dominant abundance trends of the overall sample lead to HIP 45617 being considered an unlikely member of a chemical group.

HIP 50505: T=5655 logg=4.42 ξ=1.16 [Fe/H]=-0.14

This star clearly resides along the main sequence, with a low lithium upper limit of logN(Li)≤0.50, consistent with the star being an older main sequence denizen. The star is clearly metal poor ([Fe/H]=-0.14 ± 0.03) when compared with the group mean metallicity. In examining all other elements, the star rests outside of the group abundance bands for Fe, the Fe peak elements and for Si. The tightly constrained metallicity and the consistently low abundances across all Fe peak elements lead to classification of this star as unlikely to be a group member.

HIP 112447: T=6095 logg=3.75 ξ=1.82 [Fe/H]=-0.34

This star has a distinctly low [Fe/H]=-0.34 ± 0.08, making it a member of the metal poor peak of Figure 3.7. Examining the abundances derived for other elements shows that this star is similarly metal poor in all abundances. It clearly distinguishes itself

with abundances that lay below the abundance bands defined for all elements. With this strong evidence for HIP 112447 being metal poor, it is classified as an unlikely member of a chemically dominant group.

HIP 114155: T=4348 logg=1.34 ξ=2.19 [Fe/H]=-0.58

The [Fe/H] of HIP 114155 is clearly low with a metallicity of -0.58 ± 0.07. The star shows low abundances of all elements with each [X/H] consistently lower than -0.50 dex, with the exception of [Na/H] and [Al/H]. The enhanced abundances relative to the metallicity ([Na/Fe]=0.53 ± 0.08 and [Al/Fe]=0.51 ± 0.11) can be compared with determinations of these elements in other giant stars. In a recent in depth analysis of Hyades dwarfs and giants, Schuler et al. (2009) found enhancements in Na and Al of between 0.20 and 0.50 dex in giants when compared with dwarfs and when compared to standard solar models. This perhaps points to a pattern of anomalously large Na and Al abundances in population I giants, likely a side effect of NLTE effects, discussed in more detail in chapter 5. However, in establishing group membership, the distinctly low metal abundances across multiple elements suggest that hip114155 is an unlikely member of a chemical group.

3.5.2 Possible Members

HIP 3992: T=4772 logg=2.58 ξ=1.59 [Fe/H]=-0.15

HIP 3992 has an [Fe/H]=-0.15 ± 0.04. This places it outside of the metallicity band that appears to dominate the sample. However, all other abundances rest inside their respective abundance bands. This would suggest the star is chemically consistent with the overall group. Considering the discrepancy in [Fe/H] from the mean [Fe/H] of the group, this star is not considered a likely member. The homogeneity across all other elements however, would imply that it is still possibly a member of a chemical group, neglecting the [Fe/H].

HIP 34440: T=4757 logg=2.43 ξ=1.46 [Fe/H]=-0.15

Fe, Ti and Cr for this star lay outside of the respective abundance bands. The other elements all reside within the bands which are consistent with homogeneity. Considering that Fe is considered the dominant abundance discriminant for the group and this star does not show [Fe/H] consistency with the group, this star is only considered a possible member.

HIP 12784: T=4701 logg=2.68 ξ=1.49 [Fe/H]=0.09

The uncertainty associated with the metallicity of HIP 12784 ([Fe/H]=0.09 $\pm$ 0.13) places it within the dominant metallicity band. The star resides outside of the abundance bands for Mn, Mg, Al, Na and Ni, although enhanced Al and Na are possibly demonstrating high abundances as a result of NLTE effects. Considering that it is not homogeneous in these elements, but is homogeneous across all other elements including Fe which is considered the most robust descriptor of chemical homogeneity, this star is considered a possible member of a chemical group.

HIP 36732: T=4667 logg=2.54 ξ=1.44 [Fe/H]=0.10

Fe, Mn, Ni, Na and Mg all appear slightly enriched when compared to the dominant metallicity bands. While the other elements have abundances within the metallicity trend of the overall sample, the lack of agreement for [Fe/H] with the whole sample and the consistent overabundances relative to their respective abundance bands for Mn, Ni, Na and Mg suggest this star be classified as only a possible member of a chemically dominant sample.

HIP 41484: T=5855 logg=4.41 ξ=1.17 [Fe/H]=0.08

The metallicity of HIP 41484 is supersolar compared to the group ([Fe/H]=0.08 $\pm$ 0.03). This supersolar trend, however, does not seem consistent across the other elements. The abundances derived for all other elements agree with the abundance bands used to constrain homogeneity. The lithium abundance of logN(Li)=1.93 $\pm$ 0.04 places the star below the lithium trend of the Pleiades, indicating it is not likely a pre-main sequence star.

The lithium abundance is within the limits for resting within the trend of the Hyades, suggested a lower age limit of approximately Hyades age, although the lithium abundance is likewise coincident with the trend of NGC 752 and M67, making age information inconclusive. Considering the homogeneity across multiple elements, but recalling that [Fe/H] is the key indicator for establishing abundance agreement across the whole sample, this star is considered a possible member of a dominant group.

HIP 53229: T=4690 logg=2.61 ξ=1.47 [Fe/H]=-0.10

The metallicity of HIP 53229 ([Fe/H]=-0.10 $\pm$0.15) can be associated with the dominant metallicity band of the group, within its respective uncertainty. Examining the other abundances, Cr is the only element that does not appear within the abundance bands for the group. Homogeneity is observed across all the other elements, although note that the homogeneity in Mg, Al, Ti, Ti2 and Na could be a side effect of the non-trivial uncertainties which are as high as 0.20 dex. Considering the possibly illusory effect of uncertainties resulting in homogeneity and that the overall [Fe/H] is not in close agreement with the mean group metallicity without the significant uncertainty associated with it, this star is considered a possible member of a chemically dominant sample.

HIP103983: T=5750 logg=4.52 ξ=1.16 [Fe/H]=0.02

The status of this star is somewhat of an enigma. While an isochrone fit is consistent with placement on the subgiant branch of an 8.5 $\pm$ 0.11 Gyr isochrone, the surface gravity of log(g)=4.52 suggests a dwarf luminosity class. Note the significant uncertainty in the surface gravity measurement (0.20 dex). In examining the literature, Valenti & Fischer (2005) find a surface gravity of 4.37, consistent with the lower limit of the spectroscopic gravity derived here. Further comparing surface gravity estimates, the physical surface gravity derived for this star is logg=4.22 $\pm$ 0.23, which would be consistent with subgiant status. The lithium abundance, logN(Li)=1.90 $\pm$ 0.07 places this star within the lower end of the lithium trend observed in both NGC 752 and M67. This would suggest consistency with a 2-3 Gyr age for a dwarf, but definitive age conclusions based on the lithium are impractical considering

the scatter and overlap in lithium abundances in both NGC 752 and M67. If the star were indeed a subgiant, does the lithium abundance yield different conclusions? The mass of an 8.5 Gyr subgiant with a temperature of 5750 K would be 1.05 $M_{\odot}$. This yields a ZAMS temperature, T_{ZAMS}=5754 K, which coincides with a Pleiades lithium abundance of logN(Li)=3.00 in the so-called "lithium plateau", suggesting the star would have been a good preserver of lithium, not inconsistent with the observed lithium of logN(Li)=1.90. The evolutionary status of this star, consequently, remains elusive. Examining the abundances, the star has an [Fe/H]=0.02 $\pm$ 0.05, which is consistent with it being a member of a chemically dominant subgroup with a characteristic metallicity near -0.03. The α and Fe peak elements, likewise, yield abundances that reside within the respective abundance bands that are used to characterize homogeneity. Considering the uncertainty with whether this star is possibly a 2-3 Gyr dwarf or a 8.5 Gyr subgiant, it is considered a possible member of a group.

HIP 105341: T=4005 logg=4.67 ξ=0.83 [Fe/H]=-0.05

This star is the coolest dwarf in the sample. The chromospheric activity (logR'$_{HK}$=-4.552) from Gray et al. (2006) suggests this is a relatively active star, which may be consistent with PMS status, although it is not inconsistent with a main sequence age. The activity derived age, using the updated age/activity relation of (Mamajek & Hillenbrand, 2008) results in an age estimate of 0.852 Gyr $\pm$ 0.25 Gyr, which dates the star as residing on the MS. While this activity/age estimate would suggest the star does not belong in a 2-3 Gyr Wolf group, the quoted error only includes uncertainty based on the calibration relationship. Furthermore, activity based ages, while useful in a statistically significant sample size, should not be considered robust enough to constrain individual field star ages well enough to eliminate pre-main sequence status for this star. The lithium upper limit (logN(Li)$\leq$-0.25) would plausibly place the star in the lithium trend traced by the Pleiades in Figure 3.12. This is also possibly indicative of HIP105341 being a pre-main sequence star. In examining the abundance information for the star, the metallicity of [Fe/H]=-0.05

$\pm$ 0.19 is consistent with this being a member of a dominant chemical group centered on [Fe/H]=-0.03. Further exploring the abundances it appears to reside within the dominant abundance groups for each element, with the exception of Na and Ni. In fact, the Ni abundance of [Ni/H]=0.33 is unusually large compared to the rest of the sample. Considering that the abundances of Mn, Mg, Ti, Al and Fe all rest within the respective abundance bands, but noting that the evolutionary state of the star (i.e. pre-main sequence or main sequence) remains uncertain this star is considered a possible member of a chemically defined Wolf group.

HIP 114924: T=6179 logg=4.36 ξ=1.59 [Fe/H]=0.06

With an [Fe/H]=0.06 $\pm$ 0.03, hip114924 appears to reside outside of the dominant metallicity sample. It also appears to reside outside of the homogenous bands for Cr and Na. For all other elements, it resides inside the homogeneous bands. The lithium abundance, logN(Li)=2.75 $\pm$ 0.06 is the highest in the sample. Examining the placement in Figure 3.12, the star resides along the lower envelope of the so-called lithium plateau. This would suggest that hip114924 is a good preserver of lithium; in this case, the Li is not a sensitive discriminant of age. Considering that its [Fe/H] is not consistent with the metallicity band of the group, but that multiple other elements do appear consistent with their respective abundance bands, this star is considered a possible member of the chemically dominant group.

3.5.3 Likely Members

HIP 3455: T=4860 logg=2.53 ξ=1.49 [Fe/H]=0.00

This star has an [Fe/H]=0.00 $\pm$ 0.03 that is consistent with the dominant group metallicity. In examining the other elements, it resides within every abundance band, suggesting its classification as a likely member of a homogeneous subsample.

HIP 6732: T=4665 logg=2.45 ξ=1.58 [Fe/H]=-0.03

This star has a metallicity ([Fe/H]=-0.03 $\pm$ 0.04) which matches closely with the weighted average of the group. Examining the other elements, the abundances all appear to reside within the respective group metallicity bands, with Cr, Ba and Ti yielding abundances within 0.05 dex of the average group abundance. The homogeneity demonstrated across all elements and the agreement of [Fe/H] with the mean group abundance suggest that HIP 6732 is a likely member of a chemically homogeneous group.

HIP 13701: T=4675 logg=2.71 ξ=1.37 [Fe/H]=-0.03

This star clearly resides within the dominant [Fe/H] band. Indeed, its abundance is nearly identical to the weighted mean of the sample. It appears consistent with the metallicity bands for all elements. This homogeneity with the rest of the sample leads to classifying HIP 13701 as a likely group member.

HIP 14501: T=5785 logg=4.44 ξ=1.24 [Fe/H]=-0.08

According to the [Fe/H]=-0.08 $\pm$ 0.04, HIP 14501 resides inside of the dominant metallicity band. In fact, it resides in the metallicity bands for all elements and, in many cases, the average abundance of each element nearly matches with the weighted mean used to characterize the abundance trend of the sample. This star is, therefore, an ideal candidate for being a likely member.

HIP 29525: T=5710 logg=4.57 ξ=1.28 [Fe/H]=-0.03

This star appears to reside nicely along the main sequence of the fitted isochrones in Figure 3.6. The lithium abundance (logN(Li)=2.03 $\pm$ 0.02) places the star within the abundance trends traced by NGC 752, perhaps consistent with membership in a 2-3 Gyr group. The metallicity ([Fe/H]=-0.03 $\pm$ 0.03) firmly places this star within the abundance band that dominates the sample. The abundances of Na and Al are outside of their respective abundance bands but all other elements are within the bands. Considering the strong

agreement suggested by the [Fe/H] matching the weighted mean of the sample, this is an ideal candidate for likely membership in a chemically dominant group.

HIP 40023: T=5290 logg=3.77 ξ=1.21 [Fe/H]=-0.05

HIP 40023 has a metallicity which is within the metallicity band of the sample. Indeed, its abundances across multiple elements fit inside the respective metallicity bands regardless of their uncertainties. This suggests a high level of chemical homogeneity both internally, and with respect to the sample. The small spread in abundances for the star itself, and the small spread in abundances relative to the overall abundance bands, lead to classification of this star as a likely member of a chemically homogeneous group.

HIP 43557: T=5816 logg=4.52 ξ=1.15 [Fe/H]=-0.03

The [Fe/H] of HIP 43557 matches almost exactly with the mean abundance for the entire subsample. Mg, Na and Si for this star do not appear to lay within their respective abundance bands. However, the average abundances for Ti, Ti2, Cr and Ba all rest near the group mean abundances irrespective of their uncertainties, suggesting a high degree of homogeneity. Considering that the [Fe/H] agrees well with the mean metallicity and that the average abundances of multiple elements are close to the respective mean abundances for the group, HIP 43557 is considered a likely group member.

HIP 53465: T=4570 logg=2.50 ξ=1.30 [Fe/H]=-0.08

The metallicity of HIP 53465 ([Fe/H]=-0.08 $\pm$ 0.07) is consistent with this star being a member of a chemical subgroup. While abundaces with respective uncertainties of Al and Ti 2 are found to lay outside of the group abundance bands, the remaining elements show a high degree of homogeneity. In most elements, the absolute abundance derived lays within the abundance band regardless of uncertainty. With the agreement of these abundances with the overall apparent abundance trends and the agreement of [Fe/H] with the mean group [Fe/H], this star is considered a likely member of a chemically dominant group.

HIP 102531: T=6238 logg=3.80 ξ=1.85 [Fe/H]=0.07

The metallicity of HIP 102531 ([Fe/H]=0.07 $\pm$ 0.04) is barely outside of the 3-σ cutoff for the apparent dominant metallicity trend of the whole sample. The abundances of other elements, however, place this star within the abundance bands for Al, Ba, Ca, Mg, Mn, Ni, Si, Ti and Ti 2. Therefore, based on abundance information, this star appears to lay within a dominant chemical subsample for the group. The lithium abundance appears unique in Figure 3.12. It is the warmest star in the sample that has lithium and can be seen to lay significantly beneath any trend traced by any of the plotted open cluster dwarf abundances. From the HR diagram, this star lies along the turnoff of a 2.7 Gyr isochrone. An mass of 1.5 $\pm$ 0.1 $M_{\odot}$ is derived from this isochrone. In comparing this star with Figure 11 of Balachandran (1995), who plot lithium abundances for open clusters versus stellar mass, the lithium abundance for the derived mass appears to be between the trends for M67 and NGC 752, consistent with the estimated isochrone age of 2.7 Gyr. Recognizing that the [Fe/H] of this star is less barely outside of the metallicity cutoff for homogeneity with the sample and that the remaining elements predominantly suggest this star is part of an overall homogeneous sample, it is classified as a likely member of a chemical group

HIP 112222: T=6369 logg=4.10 ξ=1.69 [Fe/H]=0.04

HIP 112222 has a slightly enhanced [Fe/H]=0.04 $\pm$ 0.07 when compared to the overall group, yet it rests within the dominant metallicity band within its respective uncertainty. In examining the other elements, Hip112222 rests inside the abundance bands for every other element, with the exception of Mn. The location at the turnoff of a 2.7 Gyr isochrone is consistent with the upper limit lithium abundance of logN(Li) $\leq$ 1.22. Its placement in homogeneous abundance bands across multiple elements lead to this star being considered a likely member of a dominant metallicity group.

HIP 113622: T=4295 logg=2.10 ξ=1.52 [Fe/H]=0.00

With a metallicity of [Fe/H]=0.00 $\pm$ 0.08, this star rests comfortably inside the dominant metallicity band. The Ni abundance of [Ni/H]=0.29 is uncharacteristically high

for the sample, but the uncertainty of 0.26 dex is signficant, which can bring the star into close agreement with the Nickel metallicity band. Furthermore, HIP 113622 is consistently within the metallicity bands for all other elements. Consequently, it is classified as a likely member of a dominant group.

3.6 Final Membership

With the considerations above, the 34 stars in the sample have been classified as unlikely, possible and likely members of a common chemical, temporal and kinematic assemblage. There were a total of 14 stars removed from group membership due to classification as unlikely members. If the remaining 20 stars classified as possible and likely are considered to represent a chemically distinct group, then out of the original kinematically defined sample, ∼60 % remain members of a kinematically AND chemically related group.

The final evolutionary sequence traced by the possible and likely members is presented in Figure 3.13, with possible members plotted in red and likely members plotted in green. The group is reasonably well traced by an evolutionary sequence of $\sim$ 2.7 Gyr (solid line) with lower and upper limits of 2.2 Gyr and 3.2 Gyr (dashed lines). Particular attention has been paid to fit the isochrone to the two likely subgiant members that reside around the turnoff (HIP 112222 and HIP 102531), as fitting the turnoff is that standard approach for age-dating open clusters with isochrone fitting. Examining the dwarf members, HIP 41484, HIP 103983, HIP 105341, HIP 14501 and HIP 43557 have positions that place them slightly above the main sequence, however, based on lithium abundances, none of the stars are believed to be pre-main sequence objects. The notable exception is HIP 103983, which is possibly an ∼8.5 Gyr subgiant, as discussed above. The subgiant members of the group all appear to lay along the plotted isochrone, within their uncertainties. For the giant stars, HIP 3992, HIP 34440 and HIP3455 appear to lay within a "clump" indicating that they are red giant branch clump stars. The remaining members all lay on the best fit isochrone within their respective uncertainties. This leads to the conclusion that the

chemical subgroup identified can be characterized by a distinct evolutionary sequence of 2.7 ± 0.5 Gyrs.

The final UV kinematic phase space plot is presented in Figure 3.14, where possible members are again red and likely members are green. For the full sample, the UV RMS velocity dispersion is UV_{RMS}=13.0 kms^{-1}. In the final subsample of group members, UV_{RMS}=13.43 kms^{-1}, therefore the velocity dispersion remains relatively constant for the two groups. The kinematic identity has not been drastically altered by the requirement of chemical coherence to establish group membership.

Table 3.10

Membership Status

HIP	T_{spec}	[Fe/H]
	K	
UNLIKELY		
3559	5800 ± 38	-0.18 ± 0.03
4346*	3820 ± 200	0.24 ± 0.18
5027**	4398 ± 79	-0.08 ± 0.17
5286	4683 ± 74	0.29 ± 0.07
11033	4510 ± 69	0.12 ± 0.04
17792	4416 ± 32	-0.52 ± 0.06
23852	5778 ± 38	-0.14 ± 0.06
29843	6130 ± 60	0.12 ± 0.08
33671	6040 ± 55	-0.21 ± 0.04
42499	4994 ± 32	-0.56 ± 0.10
45617	4855 ± 55	-0.12 ± 0.02
50505	5655 ± 41	-0.14 ± 0.03
112447	6095 ± 100	-0.34 ± 0.08
114155*	4348 ± 75	-0.58 ± 0.07
POSSIBLE		
3992	4772 ± 53	-0.15 ± 0.04
12784	4701 ± 54	0.09 ± 0.13
34440	4757 ± 39	-0.15 ± 0.04
36732	4667 ± 62	0.10 ± 0.06
41484	5855 ± 39	0.08 ± 0.03
53229	4690 ± 34	-0.10 ± 0.15
103983	5750 ± 56	0.02 ± 0.05
105341*	4005 ± 88	-0.05 ± 0.19

Table 3.10 – Continued

HIP	T_{spec} K	[Fe/H]
114924	6179 ± 40	0.06 ± 0.03
PROBABLE		
3455	4860 ± 35	0.00 ± 0.03
6732	4665 ± 42	-0.03 ± 0.04
13701	4675 ± 30	-0.03 ± 0.03
14501	5785 ± 57	-0.08 ± 0.04
29525	5710 ± 31	-0.03 ± 0.03
40023	5290 ± 37	-0.05 ± 0.03
43557	5816 ± 42	-0.03 ± 0.04
53465	4570 ± 65	-0.08 ± 0.07
102531	6238 ± 59	0.07 ± 0.04
112222	6369 ± 100	0.04 ± 0.07
113622	4295 ± 86	0.00 ± 0.08

The weighted mean abundances of the final possible and likely members of a dominant chemical group are presented in Table 3.11. The quoted errors are the uncertainties in the weighted mean. In order to establish the homogeneity of the subsample a reduced chi-squared statistic is presented for each element. This statistic is calculated from:

$$\chi^2_\nu = \frac{\Sigma_{i=0}^{N} \frac{([X/H]_i - [X/H]_{mean})^2}{\sigma_i^2}}{N-1}$$

where $[X/H]_i$ is the abundance of each star, $[X/H]_{mean}$ is the group mean and σ_i is the uncertainty in the individual stellar abundance. Performing this test for warm stars (T≥ 5000 K) in the Hyades cluster sample data from Schuler et al. (2006), yields a χ^2_ν of 1.303. For a set of 7 stars from Schuler et al. (2003), the reduced chi-squared yields a value of 1.818. Note that the cool stars were removed from the calculation as they are believed to be impacted by overexcitation/ionization effects. With these open clusters assumed to be chemically homogeneous, an approximate reduced chi-squared of order 2 provides a rough quantitative indication of homogeneity. The χ^2_ν is presented for the full sample of 34 stars

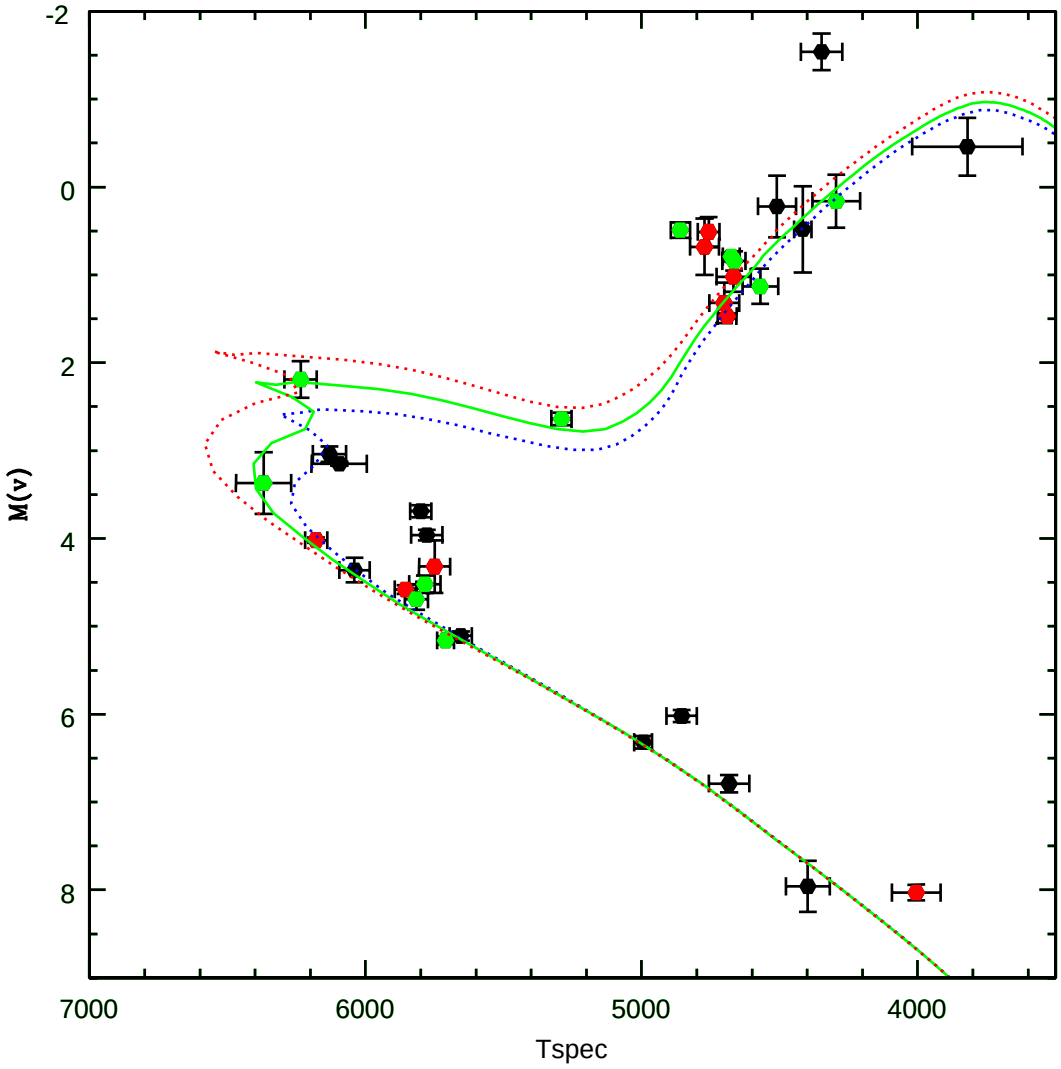

Figure 3.13 The HR diagram of the final candidate members of a common chemical group with the distinct UV kinematics of the classical Wolf 630 group. Green points are likely members while red points are possible members. Unlikely members are plotted as small points. The best fit Yale isochrone of 2.7 Gyr is a solid line with lower and upper limit isochrones of 2.2 and 3.2 Gyr , determined based on positions of extreme locations for stars near the turnoff.

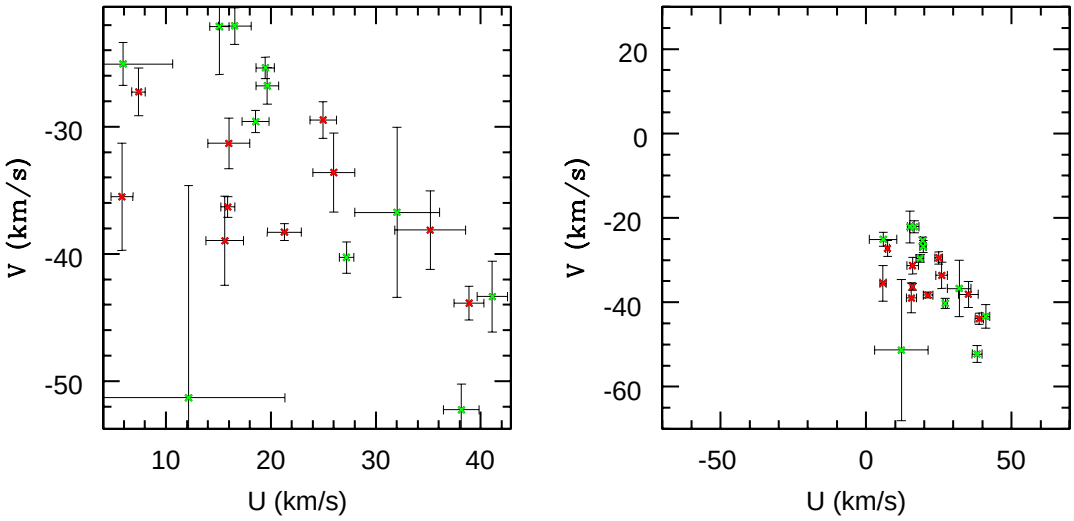

Figure 3.14 Plot of the U and V kinematics for the sample with likely members plotted in red and possible members in green.

($\chi^2_\nu all$), the final sample of 20 possible and likely group members ($\chi^2_\nu group$) and the 11 likely members ($\chi^2_\nu likely$). The decrease in reduced chi-squared between the full sample and the chemically distinct subsample demonstrates that chemically discrepant stars have been removed. Notable exceptions, with reduced chi-squared values greater than ~ 2, are found in abundances from Ni and Al. Discussion of Al and Na discrepancies is reserved for a later section.

Considering the reduced chi-squared for other homogeneous open cluster samples is comparable to the reduced chi-squared for the possible and likely members of the sample across multiple elements, the chosen sample is considered to represent a chemically consistent group with a weighted average metallicity of [Fe/H]=-0.01 ± 0.02 (uncertainty in the weighted mean). **U**sing precise chemical tagging of the 34 star sample of the Wolf moving group, a single evolutinary sequence of 2.7 ± 0.5 Gyr and [Fe/H]=-0.01 ± 0.02 has been identified for a subsample of 20 stars.

Table 3.11

Group Abundances

Element	[X/H]	$\chi^2_{\nu all}$	$\chi^2_{\nu group}$	$\chi^2_{\nu probable}$
Al/H	-0.01 ± 0.01	4.71	2.46	2.96
Ba/H	0.00 ± 0.02	3.82	1.12	1.60
Ca/H	0.09 ± 0.02	0.42	0.45	0.13
Cr/H	-0.10 ± 0.02	12.54	2.78	0.43
Fe/H	-0.01 ± 0.01	10.40	2.77	1.06
Mg/H	0.04 ± 0.02	2.12	1.60	1.11
Mn/H	-0.11 ± 0.02	10.39	2.67	1.59
Na/H	0.02 ± 0.01	7.46	4.70	4.97
Ni/H	-0.03 ± 0.02	4.09	1.92	1.31
Si/H	0.02 ± 0.02	4.82	0.77	0.84
Ti/H	-0.01 ± 0.02	1.46	0.67	0.21
Ti2/H	-0.01 ± 0.02	2.72	0.77	1.28

CHAPTER 4

DYNAMICAL EVOLUTION

4.1 Galactic Disk Potential

In order to dynamically study the formation and evolution of moving groups, NBody simulations of sample open clusters orbiting in the Galaxy have been performed using the NEMO Stellar Dynamics Toolbox (Teuben, 1995). The tidal forces acting on an orbiting open cluster are an essential component in this dynamical modeling. As such, a suitable potential which accurately reflects the Milky Way forms the basis for further study. The model used below is a modified version of that from Flynn et al. (1996), who model the Galaxy as a 6 component structure. In this dissertation, the Milky Way is modeled as a 3 component structure; a bulge, a disk and a dark matter halo with respective parameters chosen to reproduce the rotation curve of the Galaxy.

4.1.1 Bulge

The bulge is treated as a Plummer sphere potential of the form:

$$\Phi_{Bulge}(R) = \frac{-GM_{Bulge}}{\sqrt{R^2+R_{Bulge}^2}}$$

This is modeled using the plummer2 potential function from NEMO. The relevant input parameters of bulge mass and bulge radius are 1.6×10^{10} $M_\odot$, and 2700 parsecs respectively.

4.1.2 Disk

The galactic disk is modeled as a Miyamoto-Nagai potential of the form:

$$\Phi_{Disk}(R,z) = \frac{-GM_{Disk}}{\sqrt{R^2+[a+\sqrt{(z^2+b^2)}]^2}}$$

The shape parameters for the disk (a and b) are used to set the length and height of the disk, respectively. The disk is generated with the miyamoto potential from NEMO. For this model, the relevant parameters are a=5810 pc, b=300 pc and the M_{disk}=6.0×10^{10} $M_\odot$.

4.1.3 Halo

The dark matter halo is modeled as a spherical logarithmic potential using the NEMO potential, halo. The form of this potential is:

$\Phi_{Halo} = \frac{1}{2} V_c ln(r^2 + r_o^2)$

where V_c is the circular velocity at large radii (used to flatten the rotation curve at large radii), r is $\sqrt{R^2 + z^2}$ and r_o is the core radius. In this model V_c=220 kms^{-1} and r_o is the solar galactocentric radius of 8500 pc.

4.1.4 Rotation Curve

The particular potentials and their respective constants have been chosen so as to recreate the observed rotation curve of the Milky Way (Clemens, 1985). The rotation curve for the potential used to model the galaxy in this dissertation is presented in Figure 4.1. The curve qualitatively agrees with the observed rotation curve of the Milky Way (Clemens, 1985) with negligible differences in numerical values; therefore, due to the exploratory nature of the dynamical simulations to be conducted, the potential formulation described is considered suitable.

4.2 Models of Open Clusters

Observations of open clusters show that they exhibit a broad range of physical parameters. Commonly utilized parameters for describing the physical extent of open clusters include the core radius (the radius at which the stellar luminosity of the cluster has dropped by 50 %), tidal radius and total mass.

In this dissertation, open clusters are modeled by Plummer spheres (generated in NEMO with the mkplummer option) with core radii, tidal radii and total masses that represent a range of young observed open clusters. In Table 4.1, ages, radii and masses are presented for a sample of young open clusters from Piskunov et al. (2007). The 3 clusters were chosen to represent a range of cluster masses and radial extents that generally describe a sparse cluster, an average cluster and a rich cluster. Additionally, the parameters for the modeled open clusters that are generated to match the observed cluster parameters

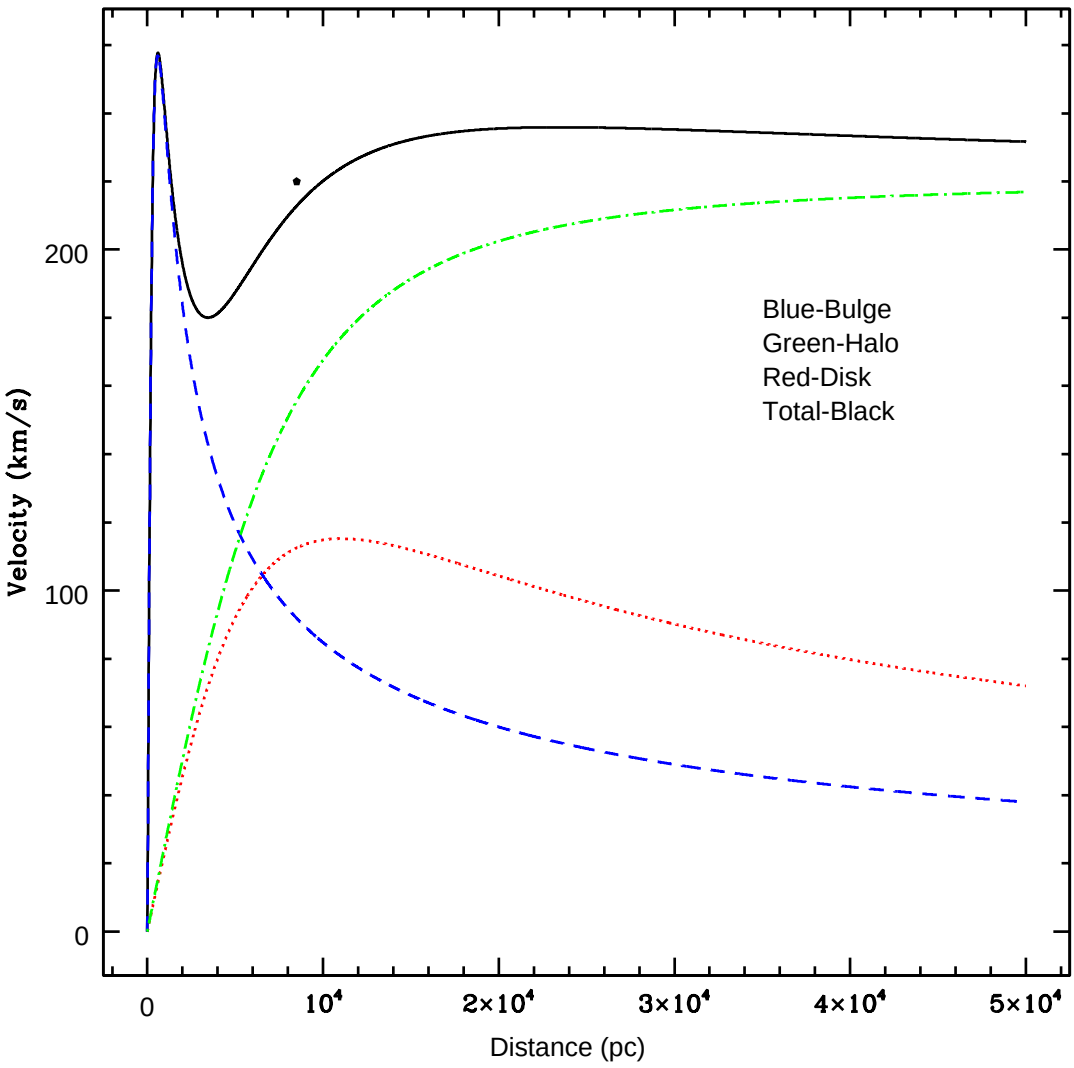

Figure 4.1 The rotation curve for the model galactic potential utilized in NEMO dynamic simulations. To first order, it matches with observed rotation curves for the Milky Way. The position of the Sun (R=8500 pc and V_C=220 kms^{-1} is plotted as a star.

are presented. The 90 % Radius is the radius that contains 90 % of the total mass of the cluster, and is used as the "tidal radius". Finally, a Salpeter-like mass function has been used to describe the mass function of stars in the model clusters.

Table 4.1

Observed and Model Open Clusters

Observed Cluster	Age	Core Radius	Tidal Radius	Mass	Model Cluster	Core Radius	90 % Radius
	Myr	pc	pc	M_{odot}	Model Cluster	pc	pc
NGC 1039	263	0.9	5.9	71	Sparse	0.89	6.3
NGC 1893	6.61	3.7	15.5	505	Average	3.69	15.4
NGC 663	13.8	3.1	15.3	923	Rich	3.10	15.5

4.3 Giant Molecular Clouds

One of the dominant forces believed to be responsible for rapidly dissolving an open cluster are interactions with large bodies in the galactic disk (Spitzer, 1958). The primary candidate for these bodies are giant molecular clouds (Wielen, 1985). In order to dynamically study the global effects of GMCs on open cluster evolution over several galactic orbits, a suitable distribution of GMCs has been developed. In this approximation, the radial distribution of the surface density of molecular H_2 from Sanders et al. (1984) was taken as a first order estimate of the distribution of Giant Molecular Clouds. In order to recreate this surface density distribution, 5000 equal mass point particles, each of 2×10^5 $M_\odot$, have been radially distributed and randomely distributed azimuthally. The total mass in GMCs of $1{\times}10^9$ $M_\odot$ is consistent with the total mass of H_2 in the Galactic disk (Carroll & Ostlie, 1996). With the radial and azimuthal distribution generated, the clouds were also evenly spread in the z-direction using $z(R) = 36e^{0.08R}$ pc, determined from the half-width of CO emission from Sanders et al. (1984). It is noted that the cloud distribution reproduces the well-established molecular ring between approximately 4.0 and 8.0 kpc. Plots of the XY spatial distribution and the height versus radius are presented in Figure 4.2 and Figure 4.3, respectively.

4.4 Stellar Dynamics with NEMO

In order to study the dynamical evolution of open clusters, the NEMO Stellar Dynamics Toolbox is utilized to simulate gravitational interactions for a cluster in a galactic disk potential studded with massive test particles used to represent giant molecular clouds. The basic approximations and assumptions described above are summarized below:

1) The galactic potential of the Milky Way is treated using a 3 component model consisting of a bulge, a disk and a halo. (described above)

2) Open clusters are modeled as plummer spheres with radii and masses representative of a “sparse”, “average” and “rich” cluster, as given in Table 4.1. (described above)

3) Giant Molecular Clouds are treated as point particles with masses of $2{\times}10^5$ $M_\odot$.

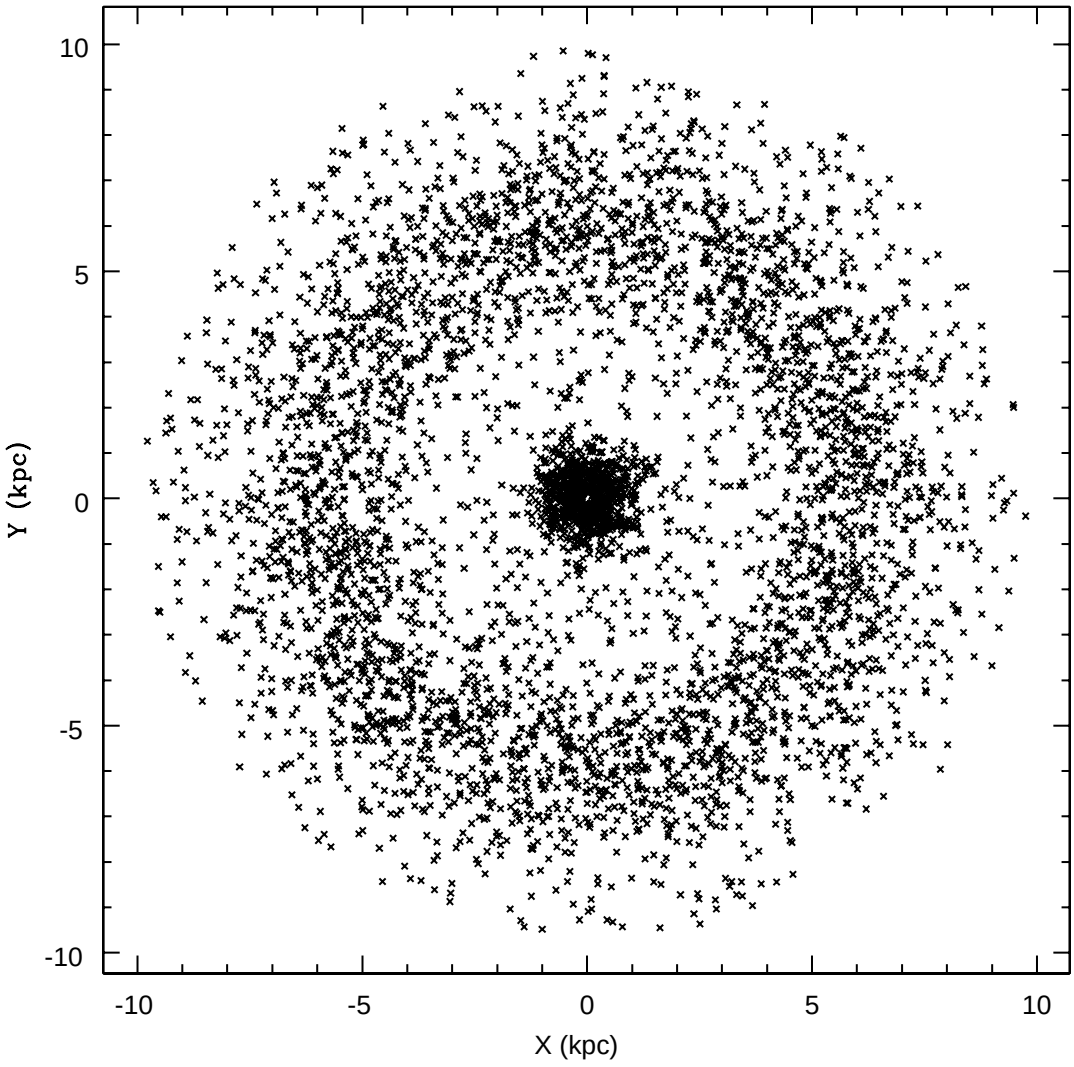

Figure 4.2 The spatial distribution of the molecular cloud distribution in the XY plane of the galaxy. The Sun resides at a position of 8.5 kpc from galactic center.

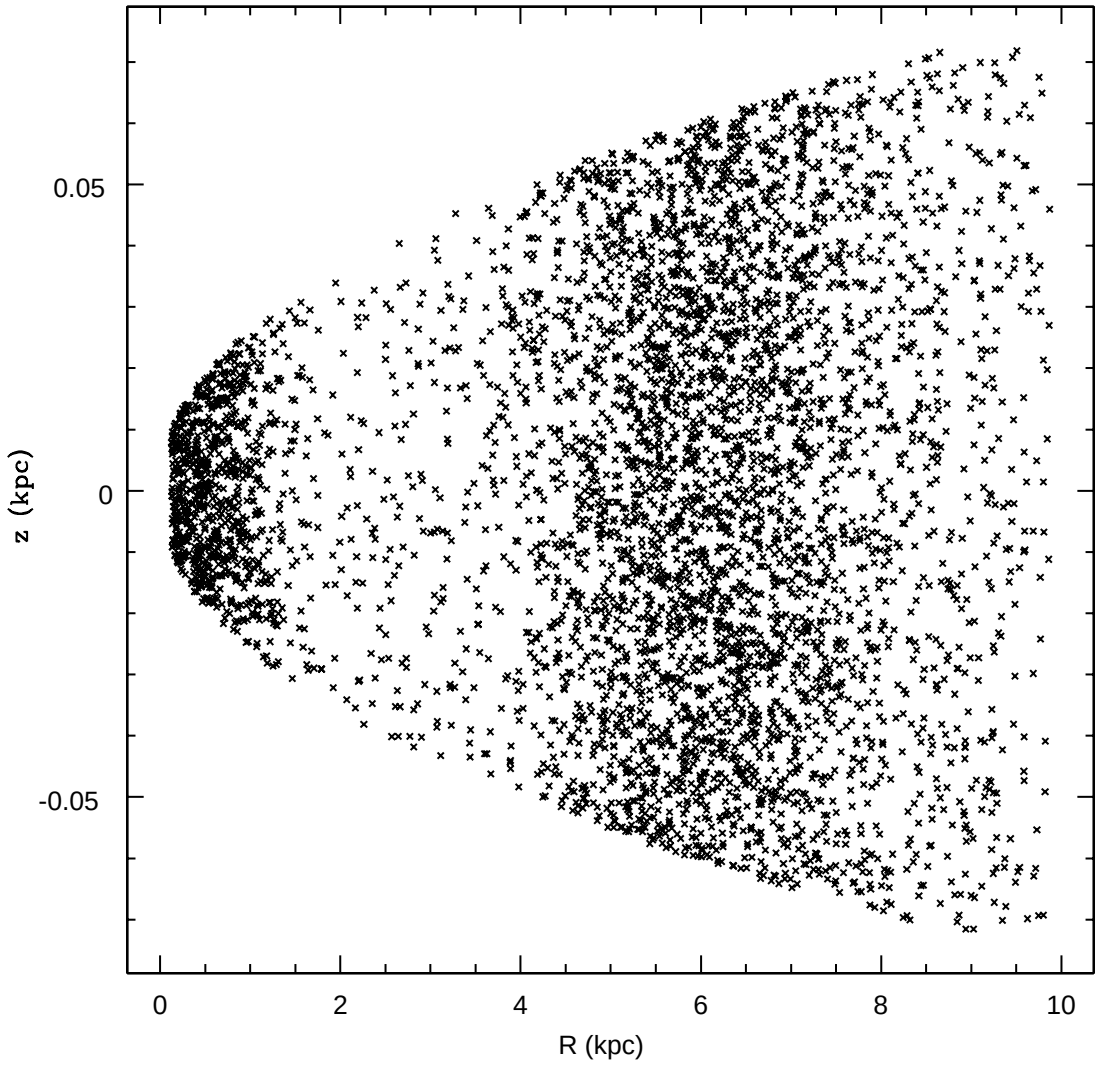

Figure 4.3 The height of molecular clouds used in the NEMO modeling. It is based on a power law dependence for galactic CO emission, as found in Wielen (1985). The height above the galactic plane, Z, is plotted versus the radial distance from the galactic center in kpc.

4) The radial distribution of Giant Molecular Clouds is traced by the distribution of molecular H_2 as given in Sanders et al. (1984), assuming azimuthal symmetry. (described above)
5) Each initial open cluster is started at the solar galactocentric radius of 8.5 kpc. All clusters possess internal velocity dispersions of order 1 kms^{-1} (comparable to the dispersions observed in open clusters from Table 1.1) and an initial circular velocity of 220 kms^{-1}. (described above)
6) The clusters are dynamically evolved for multiple galactic orbits.

The goals of these simulations are to:

1) Determine if dissolved open clusters can maintain a common kinematic identity after several galactic orbits. The target age for a moving group to maintain its velocity cohesion for this study is approximately 3 Gyr, an upper limit to the age suggested by the evolutionary sequence traced by the chemically homogeneous group identified above.
2) Perform a cursory examination as to whether an open cluster can dissolve into a kinematic structure with the distinct U and V values of the Wolf 630 group.

4.5 Kinematic Results

The reality of moving groups as dissolved open clusters relies on a cluster retaining a common kinematic identity after losing spatial association. The results of the NEMO NBODY simulations described above are utilized to explore the viability of this kinematic coherence. In the following discussion, it is important to recall that the streams shown have been isolated from the field stars of the Galactic disk. They would actually be observed against a background of field stars of which they would appear to be members. In essence, from the perspective of an astronomer, the moving groups that are formed appear as random field stars, a point which will be returned to later.

Details of the simulations have already been described, but pertinent information will be repeated here for convenience. Each model run for the sparse, average and rich cluster consisted of placing a model open cluster at a galactocentric radius of 8.5 kpc in a galactic potential populated with giant molecular clouds. The initialized velocities of the

clusters and the molecular clouds were chosen to yield circular orbits. The simulations were run for a total time of 3.0 Gyr, an upper limit to the age of the chemical subgroup identified from the kinematically defined stellar sample of this dissertation. The results of these simulations are presented in Figures 4.4 and 4.5.

4.5.1 UV Kinematics

Results for the sparse, average and rich cluster model are presented in Figure 4.4 at a time step of 3.0 Gyr. The spatial positions are presented in column 1 of the figure with X and Y positions for every star in the cluster plotted. Notice the clear stellar streaming of the dissolved cluster around the galaxy. The kinematics for all the members of each model cluster (sparse-top, average-middle, rich-bottom) are presented in the center column of Figure 4.4. Notice that the kinematics maintain a relatively tight group even after the spatial cohesion has been lost. Quantitatively, the initial RMS velocity dispersions of the clusters (determined from the quadratic sum of RMS velocity dispersions in U and V) were 0.69 kms^{-1}, 0.72 kms^{-1} and 0.72 kms^{-1} for the sparse, average and rich clusters. The final velocity dispersions of the resultant structures of column 2 in Figure 4.4 are 7.63 kms^{-1}, 6.69 kms^{-1} and 5.95 kms^{-1}. This provides a quantitative indication that **moving group structures can maintain kinematically linked to ages of 3.0 Gyr**, comparable to the upper limit for the age derived for the chemically homogeneous, kinematic group identified in this dissertation.

In order to confirm the viability of a dissolved cluster maintaining a distinct, observable group an estimate of the kinematic structure that a dissolved cluster would present for a solar neighborhood region must be obtained. For this purpose, any stars within a 800 pc cube, centered on a radius of 8500 pc in a dense region of a stellar stream are considered to represent the solar neighborhood. For convenience, this solar neighborhood is approximately identified as a green box in the spatial streams shown in column 1 of Figure 4.4. The kinematics of the stars inside of this green solar neighborhood cube (column 3 of Figure 4.4) give a demonstration of the UV kinematics in the solar neighborhood. Notice that a

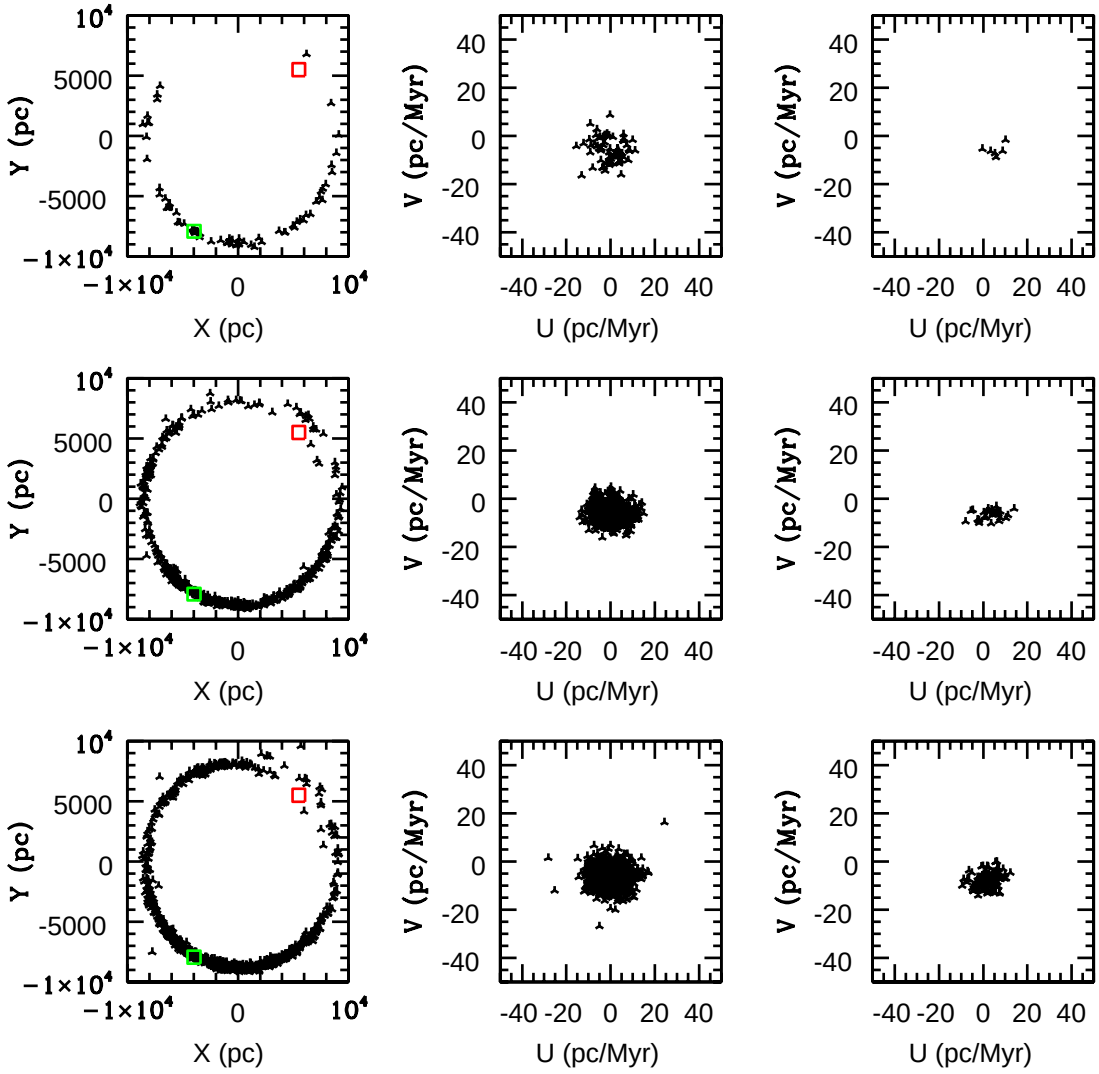

Figure 4.4 The results of NEMO simulations for model open clusters are plotted. Each model run consisted of placing a model open cluster (sparse-top row, average-middle row and rich-bottom row) at a galactocentric radius of 8.5 kpc in a galactic potential studded with giant molecular clouds. The plots give the results at a time of 3.0 Gyr. The spatial streaming (left column) plots the X and Y positions of each star in the cluster. A densely populated solar neighborhood region is shown as a green box and a low stellar number density region is shown as a red box. The solar neighborhood in this plot, is treated as a cube with sides of length 800 pc. The UV kinematics of all the stars in the cluster are plotted in the middle column. Finally, the UV kinematics in the solar neighborhood are plotted in the right column.

sparsely populated open cluster (top row) is unlikely to give a recognizable moving group, an average cluster (middle row) results in a moving group of ∼40 stars, and a rich cluster (bottom row) results in a group of ∼100 members, for the chosen solar neighborhood region of the stellar stream. This demonstrates that both average and rich open clusters can form observable moving groups in the solar neighborhood, under appropriate conditions.

The temporal streaming also contributes to the observability of a moving group. The time evolution of the stellar streaming for the "average" open cluster is shown in Figure 4.5. Notice that younger moving groups will have much higher stellar densities, making their kinematic groups more richly populated, but only in situations where the Sun rests inside the dense portion. For an older group, the streams will be significantly larger, almost spreading throughout the entire solar orbit by an age of 3 Gyr. The Sun resting inside of a dense area of the stream for an older group becomes more probable with the extended streams that an old group presents; however, the initial cluster must be richly populated to distribute significant numbers of stars along the respective stream.

4.5.2 Conditions for Observable Moving Groups

The results of these NBODY simulations demonstrate the necessary conditions for forming a moving group that is observable in the solar neighborhood. Kinematic cohesion for a dissolved cluster has been demonstrated. While spatial association is clearly not retained (evinced in the stellar streaming), the kinematics maintain a common identity with dispersion comparable to that observed in the Wolf moving group.

With the kinematic cohesion well established, the conditions for observability of a moving group appear to be: 1) The solar position in the moving group stream. This is the single most important factor for identifying an observationally useful moving group. If the Sun rests in a sparsely populated region of a dissolved cluster's stream (red box of Figure 4.4), it will not be recognizable. 2) For a young group, the streaming will not be as great, leading to greater densities of stars within the streams, even in less well populated initial clusters. The lower spatial extent of the stream limits the possible solar positions to allow

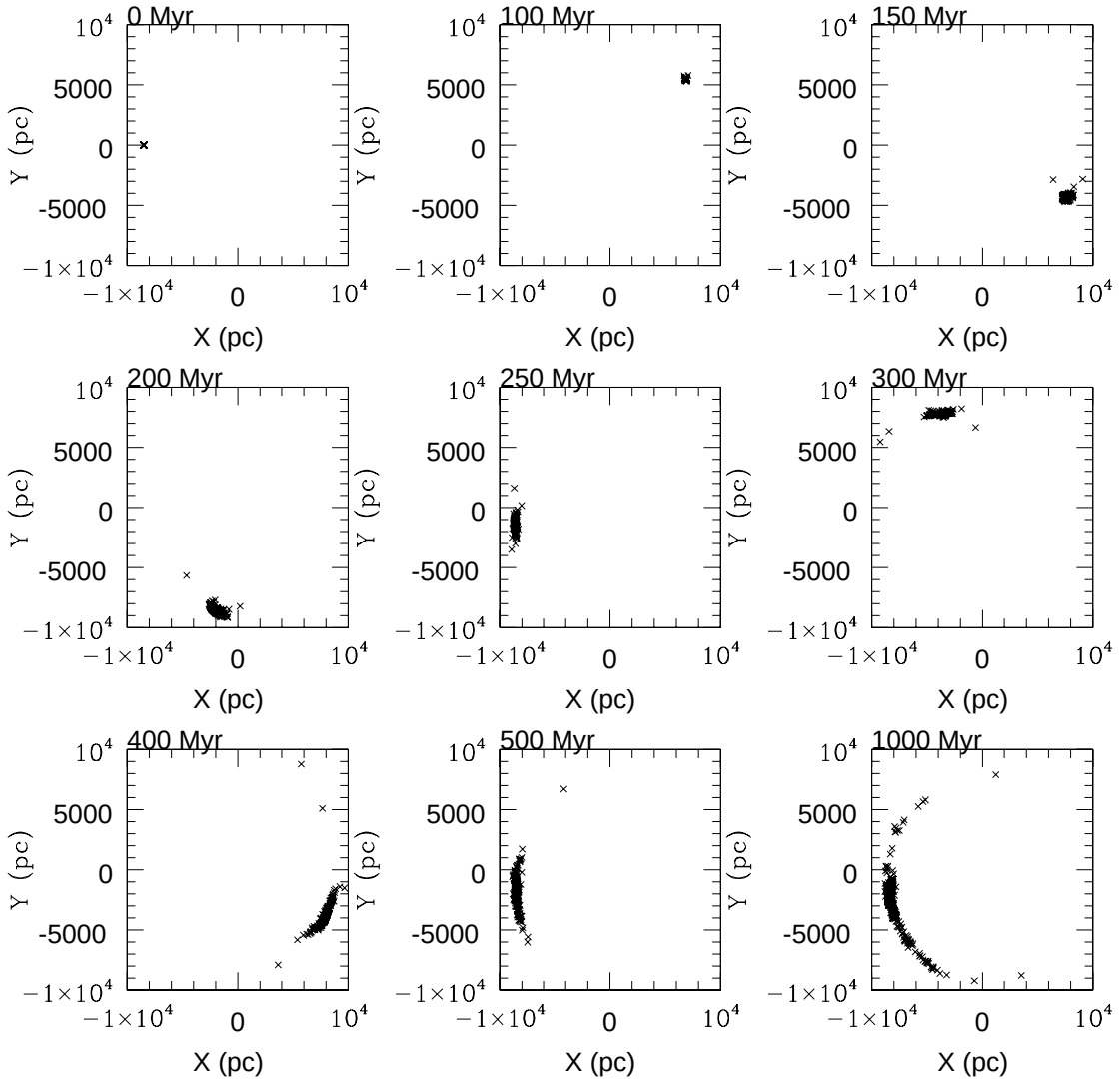

Figure 4.5 The spatial streaming for the average cluster is shown as a function of time. The X and Y coordinates for the average cluster are plotted for various timesteps, labeled at the top of each respective window. The time steps have been chosen to sample the streaming across a range of ages.

identification of a group, however the greater stellar number densities if the Sun rests at a suitable location should yield a distinct, well populated moving group. 3) For an old group, the solar position is not as critical as for younger groups. Of primary importance for an older moving group are the characteristics of the initial cluster that has dissolved, particularly the number of members. For a sparsely populated open cluster, the entensive streaming suggests that no appropriate solar position will yield a solar neighborhood structure that would be recognizable as a distinct moving group. When considering an average cluster, the proper solar position can yield a discernible group. Finally, for a rich cluster, there are significant densities at multiple positions along a stream to give the solar position significant leeway for allowing identification of a distinct moving group.

The ideal progenitors for moving groups, then, are likely to be either average or rich open clusters. Average dissolved open clusters, while offering fewer possibilities for stellar number density coinciding with the solar position, can be considered good candidates due to the greater numbers of average open clusters. A dissolved rich open cluster offers the ideal situation for yielding observable moving groups at a variety of possible solar positions; however rich open clusters are somewhat more rare than average clusters.

4.5.3 Making the Wolf 630 Group

The above simulations yielded distinct structures in the UV kinematic plane. Is it possible to recreate a group with the kinematics of Wolf 630 through an appropriate choice of initial conditions? Consider the distinct kinematics of the group, in particular V=-33 kms^{-1}, the defining velocity of the group. An examination of initial conditions for an average cluster orbiting in the cloud studded galactic potential described above has been conducted and suggests that with the appropriate choice of initial conditions, a cluster can be dissolved to yield kinematics similar to those of the group of interest.

For this simulation, the average cluster from above was initialized at a galactocentric radius of 8.0 kpc with an initial circular velocity of 200 kms^{-1} and a U velocity of -20 kms^{-1} (necessary to move the cluster out to a solar radius orbit). These results are presented in

Figure 4.6. The top panels show the spatial streaming (left column) and the kinematics of all the stars in the stream (right column). There are a the variety of kinematic structures that could be identified, dependent on the position in the stream. The bottom panel identifies the stars with the distinct V velocity of the Wolf 630 group and the spatial positions of these stars. If the Sun rests within this stream, then there would be a population of stars at the representative velocity of the Wolf group. This cursory examination demonstrates that with an appropriate choice of initial conditions, the kinematic plane can be populated by a dissolved open cluster at the representative velocity of the Wolf moving group.

4.5.4 Field Star Contamination

An additional factor for distinguishing a moving group in the solar neighborhood is their mingling with field stars. If a group is in a region of phase space that is well populated by field stars, then the likelihood of a moving group overdensity being distinct will be reduced. The possibility of identifying a distinct kinematic structure, in this case, would need to rely on the members of the kinematic space possessing a unique abundance that is distinguishable from the field. For example, HR 1614 populates a region of phase space that is occupied by many field stars. The super-solar metallicity, however, clearly identifies it as a distinct population of a dissolved open cluster. For the Wolf 630 moving group, the metallicity as determined in this dissertation ([Fe/H]$\sim$-0.01) is close to the metallicity peak of the solar neighborhood ([Fe/H]$\sim$-0.10). Consequently, the distinct kinematics being in a sparsely populated position of phase space are what make this group distinct. Thus distinct abundance, distinct kinematics or, ideally, a combination thereof are additional necessary constraints for successfully discerning a moving group superimposed against a field star background.

In order to roughly describe the possible field star contamination in the group, a simple model of the Milky Way disk was generated. In order to create this model, an exponential disk was filled with 100000 stars, each of 1 $M_{\odot}$. A characteristic scale length of 3.0 kpc and scale height of 0.2 kpc were chosen (Updike et al. (2009)). The exponential

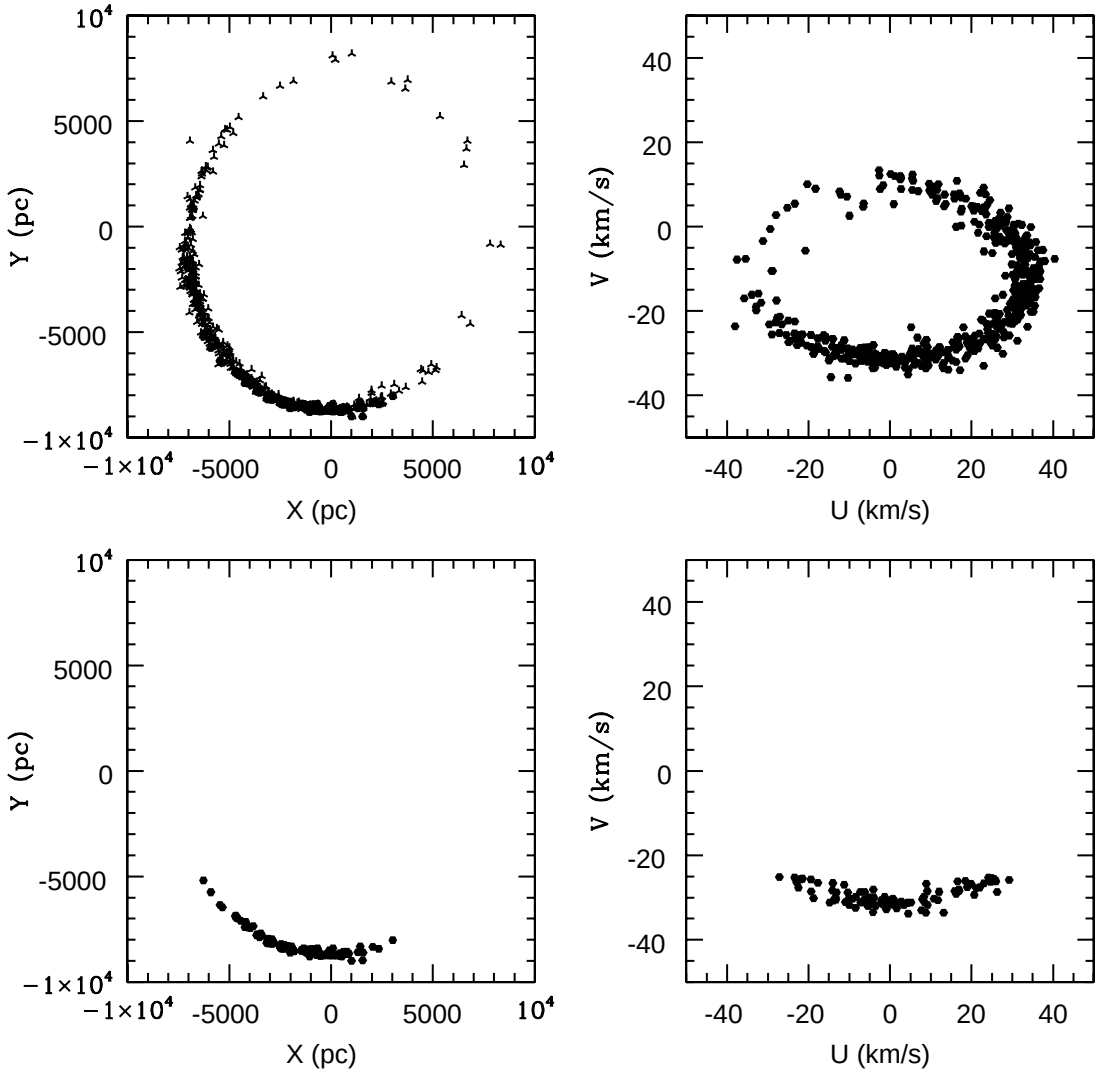

Figure 4.6 Initial parameters for creating a moving group with the distinct V velocity of the Wolf 630 moving group have been explored. The average cluster was dynamically evolved in the galactic potential with the giant molecular cloud distribution described above. The results presented were for an initial galactocentric radius of 8000 pc, with initial U and V velocities of -20 kms^{-1} and 200 kms^{-1}, respectively. The left plot shows the resultant stream of stars at a solar radius of 8500 pc. The right plot shows the UV plane for a solar neighborhood sized cube, with the distinct velocity of Wolf 630.

disk was studded with the molecular cloud distribution utilized above. All the particles (stars and clouds) were initialized to circular orbits in the Milky Way potential model used above. The exponential disk was allowed to dynamically evolve for 3.0 Gyr. Computational limitations prevented simulations with a larger number of particles.

The results of the simulation are presented in Figure 4.7. The right column shows the X and Y positions of stars within a ring that is 800 pc in width, centered on the solar galactocentric radius of 8500 pc. The kinematics for all the stars in the ring are considered to be representative of the solar neighborhood. This is different than previous solar neighborhood plots where the solar neighborhood was treated as a local density cube inside of a larger stellar stream. Here the interest is in forming a global picture of the structure that field stars would show near the Sun consequently seeking out local density enhancements is unnecessary. Qualitatively, the results show some consistency with observations of the velocity distribution in the solar neighborhood. In particular, there appears to be a systematic shift towards a negative V velocity and a slight elongation in the U direction, which is qualitatively consistent with a similar shift and stretching seen by studies of velocity structures in the solar neighborhood (Skuljan et al., 1999). Notice that a few stars could be considered to populate the region of phase space characteristic of the Wolf 630 moving group (U=23 kms^{-1}, V=-33 kms^{-1}). Considering that the initial disk was populated with $1{\times}10^5$ stars, roughly 5 orders of magnitude less than the total number of stars in the Milky Way, it seems possible that a not insignificant population of field stars could be found in the Wolf 630 area of phase space. These initial results are promising and encourage further exploration. In order to properly address the field star contamination a Milky Way model which contains a greater number of particles should be run to more adequately sample the phase space stellar density of the solar neighborhood. Additionally, the model should be run for a longer time to sample the disk over its entire lifetime of 10 Gyrs, and, potentially, open cluster models could be run inside of this disk to explore if observed moving groups can be recreated and identified within a disk of field stars.

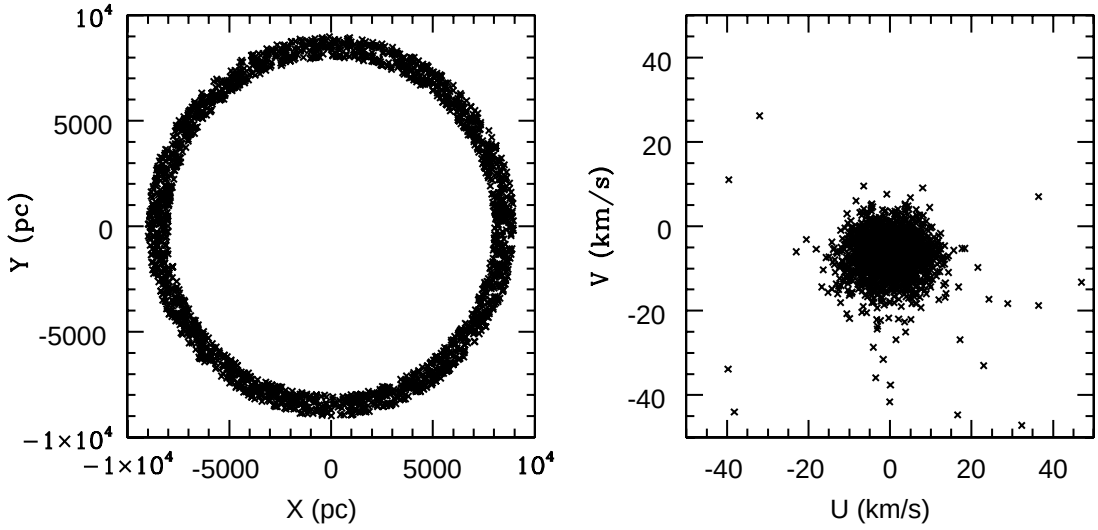

Figure 4.7 An exponential disk model of the Milky Way, composed of 100000 equal mass stars was run to examine the contamination of the Wolf 630 Moving Group by field star interlopers. The left plot shows the spatial positions for a stars within a ring of 800 pc in width, centered on the solar galactocentric radius of 8500 pc. All the stars within the ring are taken to represent the kinematics of the solar neighborhood, which are plotted in the right column. The features to note in the kinematic UV plane are the overall shift of velocities towards negative V and the slight elongation of velocity in the U direction, both qualitatively in line with observations of velocity structures in the solar neighborhood (Skuljan et al., 1999). Notice also that field stars are able to populate the kinematically distinct region occupied by the Wolf moving group, suggesting that population by field stars is occuring.

CHAPTER 5

CHEMICALLY TAGGING

5.1 Open Clusters and Moving Groups: Chemically Tagging the Disk

The primary goals of the dissertation, to establish if the kinematically defined Wolf moving group coincided with a chemically and temporally distinct group and to explore basic models of the dynamic evolution of a moving group, have been accomplished. In addition to these results, a cursory examination of some of the applications for chemically tagging the galactic disk using nearby moving group members and field stars are now explored.

5.1.1 Na and Al Abundances

The abundances of Na and Al appear to be enhanced for some of the stars in the sample. Similar enhancements have been observed in many open clusters. Most recently, an analysis of abundances in the Hyades cluster found abundance enhancements in Na and Al of 0.2-0.5 dex in giant stars when compared with dwarfs Schuler et al. (2009) in line with observations of giant stars in old open clusters (Friel et al. (2005), Jacobson et al. (2008),). These enhancements can be compared to those observed in the group members of this dissertation.

Plots of [Na/Fe] (top panel) and [Al/Fe] (bottom panel) versus surface gravity are presented in Figure 5.1. For the members of the group, the Na and Al enhancements are relatively modest, as seen in a relatively slight upward shift in abundances between dwarfs and subgiants. The giant abundances, in general, can be brought into agreement with dwarf abundances with downward revisions of 0.1-0.2 dex, consistent with NLTE corrections found in field clump giants with surface gravities down to logg=2.10 (Mishenina et al. (2006)). The single star which has greatly enhanced [Na/Fe] and [Al/Fe], Hip 114155, is an evolved, metal poor red giant with enrichments of 0.53 dex and 0.51 dex, comparable to those found by Schuler et al. (2009). According to the NLTE correction table of Takeda et al. (2003),

the recommended NLTE correction is at most -0.10, although the calculations performed do not extend below a temperature of 4500 K. Without targeted NLTE calculations available for a cool, moderately low metallicity giant like HIP114155, the enhanced abundances in this star are assumed to be a result of NLTE effects.

The other points of interest in Figure 5.1 are the two dwarfs with the greatest surface gravities ([Na/Fe]=-0.38 in HIP105341 and [Na/Fe]=-0.33 in HIP5027). Closer inspection shows that these are the two coolest dwarfs in the sample, perhaps pointing to overexcitation/ionization as a culprit for decreased abundances, similar to overexcitation/ionization effects observed in cool open cluster dwarfs (Schuler et al. (2003), King & Schuler (2005) ,Schuler et al. (2006) and Yong et al. (2004)).

These effects, if present, do not appear to similarly decrease abundances derived for [Al/Fe] which traces well with [Na/Fe] abundances for the other members of the sample. To understand the cause for this requires looking to the atomic parameters of the lines utilized for deriving the abundances, particularly the excitation potentials. A single Na line was measurable with a relatively low excitation potential of 2.10 eV and two lines were used for determining Al abundances, a 3.14 eV excitation potential line and a 4.02 eV excitation potential line. With the Na line having a lower excitation potential than the higher excitation potential Al lines, overexcitation would make Na abundances more deficient than Al.

Additionally, Na has a lower ionization potential of 5.139 eV while Al has a lower ionization potential of 5.986 eV, suggesting that Na can be more easily ionized than Al. If Na is overionized, it has a surplus of ionized atoms and abundances from neutral Na will be artificially low. The Al lines, having higher ionization potentials, will be less overionized. Additionally, the lines have moderate excitation potential, so if overexcitation is occuring, then the Al abundances from the moderately higher excitation potential lines may be enhanced, counteracting any abundance deficiencies from overionization. The presumed cause of the lowered [Na/Fe] abundances in the two coolest dwarfs is overexcitation/overionization, which is further explored below by comparing abundances from Fe I and Fe II.

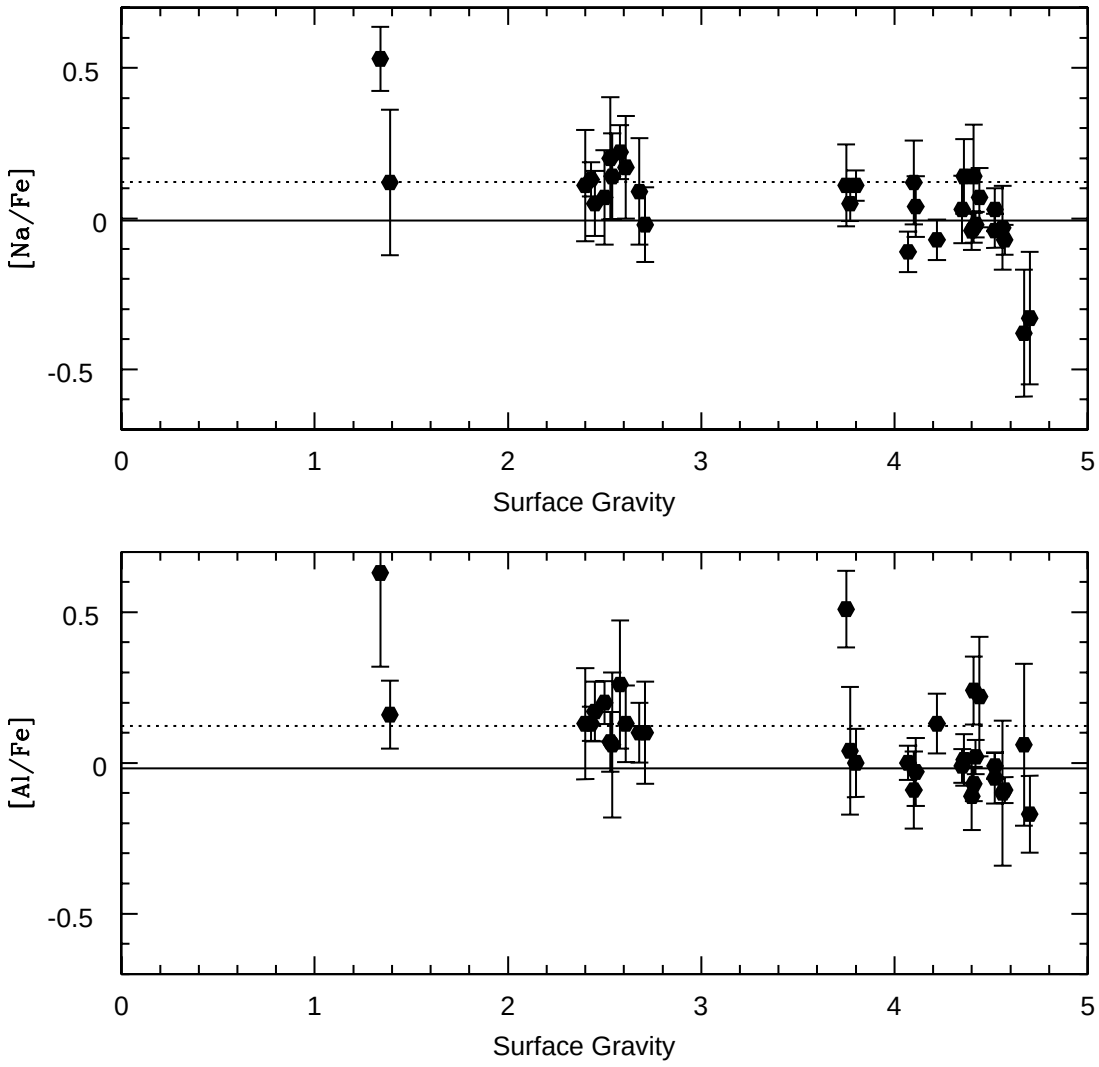

Figure 5.1 The abundances [Na/Fe] and [Al/Fe] are plotted versus surface gravity. The solid line gives the weighted mean [X/Fe] for the dwarfs, neglecting the two with unusually low [Na/Fe]. The dotted line gives the weighted mean [X/Fe] for the subgiants and giants, neglecting the giant with unusally high [Na/Fe] and [Al/Fe]. Subgiant and giant abundances are ~ 0.10 dex higher than dwarfs. This slight increase in abundances of Na and Al in the giants, relative to the dwarfs, can be corrected using literature suggested NLTE corrections. The point with enhanced [Na/Fe]=0.53 and [Al/Fe]=0.51 corresponds to HIP114155. The high abundances are expected to be a result of NLTE effects, similar to those in Hyades giants (Schuler et al., 2009). The final points of interest are the two dwarf stars that have low abundances of [Na/Fe]. A possible explanation for the abundances in these two stars is overexcitation/ionization effects, as discussed in the text.

5.1.2 Overexcitation and Overionization in Cool Dwarfs: Fe I and Fe II Abundances

In order to more closely examine the possible effects of overexcitation and overionization for the sample, abundances have been derived from Fe I and Fe II lines using physical surface gravities (recall that spectroscopic gravities are insufficient for this purpose since ionization balance forces agreement between abundances of Fe I and Fe II). Refer to Figure 5.2 where the difference in abundances between ionized and neutral Fe are plotted versus temperature (top panel) and versus surface gravity (bottom panel). For stars warmer than 4500 K the general trend, as seen in the top plot, suggests slight overionization (where Fe II abundances are mildly enhanced relative to Fe I abundances) as a function of temperature. The situation takes a drastic change for the two coolest dwarfs in the sample, the same two stars which evinced unusually low [Na/Fe], considered to be a side effect of overionization, which is seemingly confirmed by the overionization in Fe II abundances.

Two effects could explain the overionization results. The more "exotic" explanation is that the stars are active young dwarfs and, thus, heavily spotted. Recent work suggests that heavily spotted stars have radii which are "puffed" compared to a standard stellar model (Torres & Ribas (2002), Morales et al. (2008), King et al. (2009)). An increased radius would decrease the surface gravity of the star compared to unspotted analogs, which would be manifested by increasing Fe II line strengths via overionization. In order to explore the viability of this explanation, the radius that corresponds to the surface gravity needed to eliminate the abundance difference between [Fe II/H] and [Fe I/H] was determined for HIP5027. A surface gravity of 3.57 was found to result in agreement between abundances from Fe I and Fe II, neglecting the minization in correlations in temperature and microturbulence. From Yale-Yonsei isochrones, a mass of 0.66 $M_{\odot}$ is assumed. The radius for this gravity is R=2.19 $R_{\odot}$. The radius corresponding to this mass and the physical surface gravity of logg=4.70 is R=0.60 $R_{\odot}$. From Morales et al. (2008) an upper limit that can be expected for radius changes in this "spotted" regime is $\sim$10%, well beneath the radius change implied by the necessary surface gravity change to eliminate overionization and well outside of the uncertainty in the physical logg. This points to a more likely scenario of

significant NLTE effects yielding increased overionization as a function of decreasing temperature as observed in many cool open cluster dwarfs (Yong et al. (2004), Schuler et al. (2006)).

5.1.3 Oxygen Abundances: Moving Groups Versus Open Clusters

Abundances for the high excitation potential oxygen triplet at λ7771, λ7774, λ7775 have been derived from equivalent widths. In examining the results derived from the triplet, abundances from the λ7774 Å and λ7775 Å lines appear to be enhanced as a general function of decreasing temperature in both dwarfs (Figure 5.3) and giants. A similar enhancement of the central line (7774.1 Å) in cooler giants was noted by (Schuler et al., 2006) in their study of oxygen in Hyades giants. They believed this enhancement to be due to a possible blend with an Fe I feature at 7774.00 Å. While the nature of any blending for the reddest feature (7775 Å) is unclear, visual inspection of the spectral line reveals a slight asymmetry, possibly indicating a blend. The distinct increase in [O/H] abundances derived from the red features of the triplet as a function of decreasing temperature suggest that only the blue line (7771.1 Å) of the triplet should be used for oxygen abundance determinations in cooler stars. Furthermore, abundances derived from the triplet are believed to be enhanced by NLTE effects. Corrections from the work of (Takeda, 2003) have been applied to derive NLTE corrected abundances from the triplet lines. The oxygen equivalent widths for the triplet are given in Table 5.1. The LTE oxygen abundances are given in Table 5.2, and the final NLTE oxygen abundances are shown in Table 5.3.

Table 5.1

EQW of Oxygen Triplet

HIP	EW_{7771}	EW_{7774}	EW_{7775}
	mÅ	mÅ	mÅ
Solar	70.9	60.3	48.8
102531	157.7	139.7	114.0
103983	67.8	60.8	48.0
11033	23.0	37.8	27.1
112222	129.8	117.5	101.0

Table 5.1 – Continued

HIP	EW_{7771}	EW_{7774}	EW_{7775}
	mÅ	mÅ	mÅ
112447	109.1	96.3	76.6
113622	19.5	45.4	26.5
114155	44.2	52.0	35.3
114924	109.2	97.6	78.2
12784	31.4	36.5	29.9
13701	36.3	34.8	27.9
14501	75.0	71.9	55.8
17792	22.9	21.7	18.2
23852	80.8	66.3	55.4
29525	66.8	59.8	47.4
29843	121.8	104.1	85.2
33671	86.7	78.8	62.6
34440	36.7	40.3	31.4
3455	45.4	44.1	34.7
3559	77.1	66.8	56.1
36732	33.9	47.6	34.6
3992	39.3	46.5	37.6
40023	50.8	48.7	36.2
42499	21.2	17.7	13.5
43557	72.4	62.9	47.3
45617	11.8	14.3	8.9
5286	16.6	18.0	13.0
53229	28.2	39.3	26.4
53465	22.5	30.8	23.5
6732	37.9	42.3	34.4

Table 5.2

LTE Oxygen

HIP	$[O/H]_{6300}$	$[O/H]_{7771}$	$[O/H]_{7774}$	$[O/H]_{7775}$
102531	0.18 ± 0.07	0.48 ± 0.04	0.44 ± 0.04	0.33 ± 0.05
103983		-0.03 ± 0.09	0.00 ± 0.09	0.01 ± 0.11
11033	0.19 ± 0.14	-0.06 ± 0.14	0.62 ± 0.15	0.48 ± 0.14
112222		0.16 ± 0.09	0.18 ± 0.09	0.17 ± 0.14
112447		0.01 ± 0.09	0.01 ± 0.09	-0.06 ± 0.11
113622	0.04 ± 0.15	0.15 ± 0.28	1.06 ± 0.28	0.69 ± 0.29
114155	-0.59 ± 0.11	0.39 ± 0.37	0.75 ± 0.37	0.53 ± 0.18

Table 5.2 – Continued

HIP	$[O/H]_{6300}$	$[O/H]_{7771}$	$[O/H]_{7774}$	$[O/H]_{7775}$
114924		0.11 ± 0.03	0.14 ± 0.03	0.08 ± 0.04
12784	0.04 ± 0.10	0.02 ± 0.10	0.35 ± 0.10	0.35 ± 0.10
13701	0.03 ± 0.04	0.24 ± 0.06	0.37 ± 0.06	0.35 ± 0.06
14501		0.06 ± 0.07	0.16 ± 0.07	0.11 ± 0.07
17792	0.15 ± 0.10	-0.03 ± 0.15	0.09 ± 0.15	0.15 ± 0.15
23852	-0.01 ± 0.10	0.09 ± 0.05	0.04 ± 0.05	0.06 ± 0.07
29525		0.01 ± 0.04	0.07 ± 0.04	0.06 ± 0.04
29843		0.27 ± 0.06	0.22 ± 0.06	0.17 ± 0.06
33671		-0.05 ± 0.05	0.01 ± 0.05	-0.02 ± 0.05
34440	-0.04 ± 0.09	-0.09 ± 0.08	0.18 ± 0.14	0.13 ± 0.11
3455	-0.01 ± 0.05	0.01 ± 0.08	0.14 ± 0.08	0.10 ± 0.08
3559	0.16 ± 0.03	-0.04 ± 0.04	-0.03 ± 0.04	0.00 ± 0.04
36732	0.08 ± 0.12	0.06 ± 0.21	0.61 ± 0.20	0.46 ± 0.22
3992	0.05 ± 0.06	0.02 ± 0.13	0.38 ± 0.13	0.35 ± 0.12
40023	-0.14 ± 0.05	0.00 ± 0.05	0.13 ± 0.05	0.06 ± 0.04
42499		-0.18 ± 0.05	-0.16 ± 0.05	-0.13 ± 0.05
4346	-0.10 ± 0.16			
43557		-0.01 ± 0.05	0.01 ± 0.05	-0.05 ± 0.06
45617		-0.26 ± 0.08	-0.06 ± 0.09	-0.17 ± 0.08
5286		0.27 ± 0.23	0.50 ± 0.23	0.46 ± 0.23
53229	-0.10 ± 0.12	-0.11 ± 0.14	0.40 ± 0.15	0.17 ± 0.13
53465	0.22 ± 0.15	-0.19 ± 0.32	0.29 ± 0.33	0.23 ± 0.33
6732	0.01 ± 0.01	0.12 ± 0.09	0.41 ± 0.09	0.40 ± 0.11

Table 5.3

NLTE Oxygen

HIP	$[O/H]_{6300}$	NLTE $[O/H]_{7771}$	NLTE $[O/H]_{7774}$	NLTE $[O/H]_{7775}$
102531	0.18 ± 0.07	0.11 ± 0.04	0.13 ± 0.04	0.10 ± 0.05
103983		0.00 ± 0.09	0.01 ± 0.09	0.02 ± 0.11
11033	0.19 ± 0.14	-0.03 ± 0.14	0.63 ± 0.15	0.48 ± 0.14
112222		-0.05 ± 0.09	-0.02 ± 0.09	0.00 ± 0.14
112447		-0.02 ± 0.09	-0.14 ± 0.09	-0.07 ± 0.11
113622	0.04 ± 0.15	0.18 ± 0.28	1.00 ± 0.28	0.68 ± 0.29
114155	-0.59 ± 0.11	0.32 ± 0.37	0.65 ± 0.37	0.47 ± 0.18
114924		0.03 ± 0.03	0.07 ± 0.03	0.03 ± 0.04
12784	0.04 ± 0.10	0.05 ± 0.10	0.36 ± 0.10	0.36 ± 0.10
13701	0.03 ± 0.04	0.26 ± 0.06	0.39 ± 0.06	0.36 ± 0.06

Table 5.3 – Continued

HIP	$[O/H]_{6300}$	NLTE $[O/H]_{7771}$	NLTE $[O/H]_{7774}$	NLTE $[O/H]_{7775}$
14501		0.05 ± 0.07	0.14 ± 0.07	0.10 ± 0.07
17792	0.15 ± 0.10	-0.01 ± 0.15	0.11 ± 0.15	0.16 ± 0.15
23852	-0.01 ± 0.10	0.05 ± 0.05	0.01 ± 0.05	0.03 ± 0.07
29525		0.04 ± 0.04	0.10 ± 0.04	0.10 ± 0.04
29843		0.11 ± 0.06	0.10 ± 0.06	0.07 ± 0.06
33671		-0.08 ± 0.05	-0.02 ± 0.05	-0.04 ± 0.05
34440	-0.04 ± 0.09	-0.12 ± 0.08	0.13 ± 0.14	0.09 ± 0.11
3455	-0.01 ± 0.05	-0.04 ± 0.08	0.08 ± 0.08	0.05 ± 0.08
3559	0.16 ± 0.03	-0.09 ± 0.04	-0.07 ± 0.04	-0.04 ± 0.04
36732	0.08 ± 0.12	0.07 ± 0.21	0.60 ± 0.20	0.45 ± 0.22
3992	0.05 ± 0.06	-0.01 ± 0.13	0.32 ± 0.13	0.30 ± 0.12
40023	-0.14 ± 0.05	0.00 ± 0.05	0.12 ± 0.05	0.06 ± 0.04
42499		-0.09 ± 0.05	-0.08 ± 0.05	-0.06 ± 0.05
4346	-0.10 ± 0.16			
43557		0.00 ± 0.05	0.01 ± 0.05	-0.04 ± 0.06
45617		-0.17 ± 0.08	0.02 ± 0.09	-0.10 ± 0.08
5286		0.38 ± 0.23	0.60 ± 0.23	0.55 ± 0.23
53229	-0.10 ± 0.12	-0.08 ± 0.14	0.41 ± 0.15	0.18 ± 0.13
53465	0.22 ± 0.15	-0.15 ± 0.32	0.31 ± 0.33	0.24 ± 0.33
6732	0.01 ± 0.01	0.12 ± 0.09	0.41 ± 0.09	0.39 ± 0.11

Dwarfs

For the dwarfs, oxygen was derived solely from the high excitation near-IR triplet. The triplet abundances appear internally consistent until reaching the cool end of the sample. Two of the dwarfs cooler than 5000 K give enhanced oxygen from the λ7774 and λ7775 lines (HIP45617 and HIP5286) (Figure 5.3). In order to test the possibility of an Fe blend as discussed above, two cool stars of the sample with no measurable oxygen abundances (HIP5027 and HIP105341) were examined to see if they showed any indications of an Fe blending feature near 7774 Å. In HIP5027 a possible detection of a feature at 7774 Å was found to have a measured equivalent width of roughly 6.0 mÅ. This would not be inconsistent with the expected contribution required from a blending feature to give the observed abundance enhancement in the 7774 Å line. While there is no known blending feature near

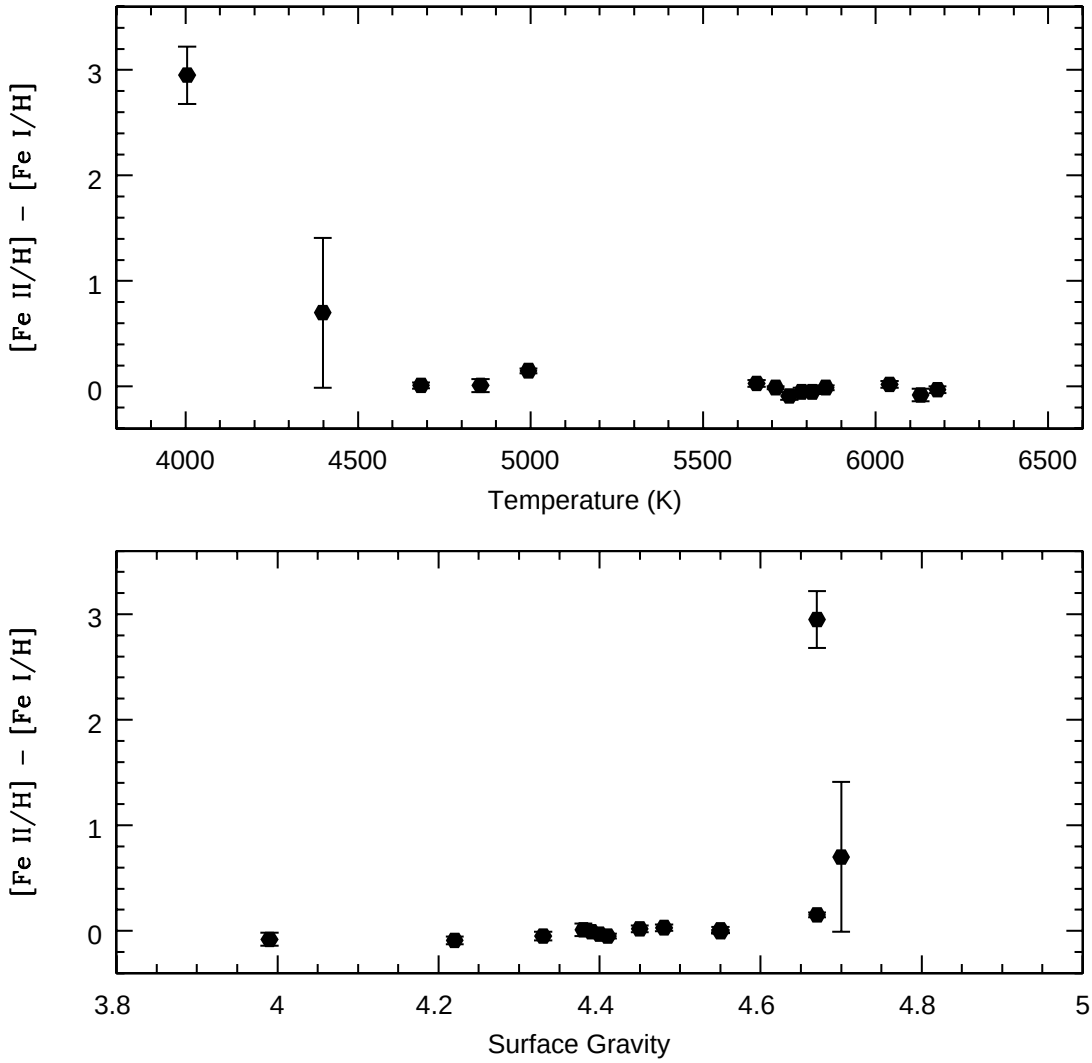

Figure 5.2 The difference [Fe II/H]-[Fe I/H] is plotted versus temperature (top) and surface gravity (bottom). Notice the clear overionization in the two coolest dwarfs of the sample. Recall that overionization was assumed to be the cause of lowered abundances in [Na/Fe] in the two cool dwarfs that appear to be overionized.

the λ7775 line, visual inspection shows possible indications of blending as evinced in a slight asymmetry of the spectral line.

Neglecting the two red triplet lines in the cool dwarfs, the [O/H] trend of the dissertation sample is plotted along with the Pleiades trend from Schuler et al. (2004) (where [Fe/H]=0.00 was assumed to calculate [O/Fe]), and the Hyades trend of Schuler et al. (2006) (where [Fe/H]=+0.13 was assumed to calculate [O/Fe]) in Figure 5.4. To summarize their findings, from triplet based [O/H] abundances in 45 Hyades dwarfs, they found a remarkable increase in [O/H] as a function of decreasing temperature for stars with $T_{eff} \leq 5400$ K. The curve describing the increasing [O/H] in the $\sim$ 120 Myr old Pleiades appeared to be more steep than the trend observed in the $\sim$ 625 Myr old Hyades, perhaps pointing to an age-related effect whereby [O/H] enhancements in cooler stars decrease as a function of increasing age. In fact Schuler et al. (2006) utilized toy spot models to simulate the effects of photospheric temperature inhomogeneities and found that, with appropriate choices for sizes of stellar hot spots, the equivalent widths of the Hyades triplet lines could be recreated. This perhaps points to an age related effect where younger stars which presumably have greater activity and spot coverage yield spuriously higher abundances than older counterparts which do not suffer from such temperature inhomogeneities. In this respect, the field dwarfs in this sample do not show a drastic increase in abundance as a function of decreasing temperature. If the abundance trend observed by Schuler et al. (2004) and Schuler et al. (2006) is age dependent, the lack of a distinct trend of increasing [O/Fe] with decreasing abundance may point to the stars in the sample being older than the Hyades, not inconsistent with the 2.7 Gyr age of the dominant subsample identified above. In leiu of an age-related effect this would point to an as yet unknown dichotomy between oxygen abundances in field stars and cluster stars, the nature of which would have to be explored with abundances in of field stars of quantifiable age. The single star that appears to reside within the increasing Hyades trend at cooler temperatures is metal weak (HIP 42499, [Fe/H]=-0.56), resulting in [O/Fe]=+0.47. The enhanced [O/Fe] ratio at this low metallicity is unsurprising and coincides with the characteristic field dwarf enhancements

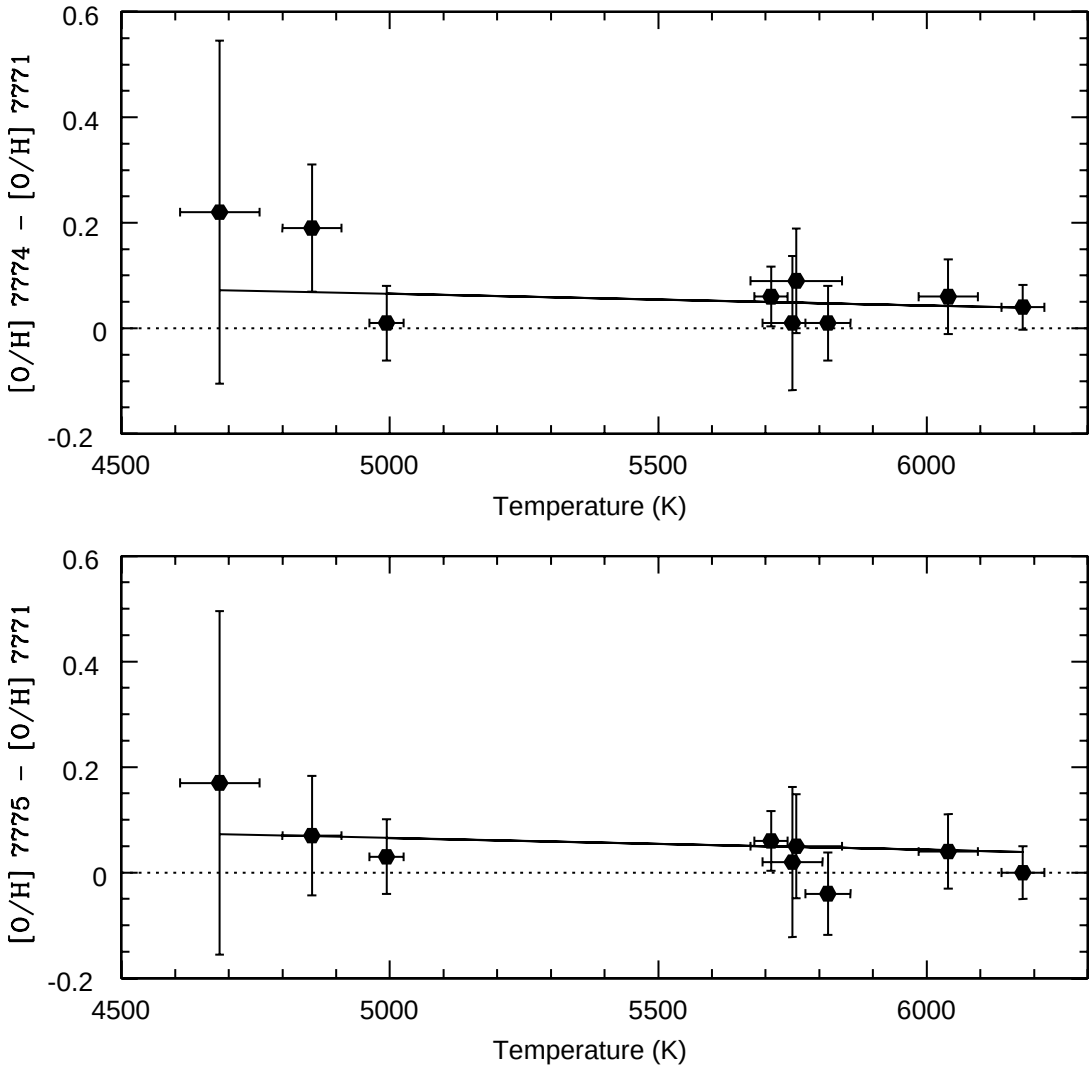

Figure 5.3 Differences in oxygen abundances for dwarf stars derived from the infrared triplet. The top plot shows the difference in the abundance from the 7774 line and the 7771 line. The difference in abundance between these two lines for the coolest two stars in the sample is of order 0.20 dex. The difference between the 7775 line and the 7771 line is slightly more modest, but the general trend is for the cooler stars to yield slight abundance enhancements.

observed as a function of decreasing temperature for oxygen in other metal poor field stars (Abia & Rebolo, 1989)

Giants

For the giant stars in the sample, oxygen abundances have been derived from the infrared triplet and from the forbidden line at λ6300.301 Å.

In examining the triplet abundances, a similar effect as in the dwarfs is observed as temperatures decrease. There appear to be enhancements in oxygen abundances derived from both the 7774 Å and 7775 Å lines. The enhancements appear greatest in the middle line, consistent with the assumption that there is a blending feature of Fe which appears at sufficiently cooler temperatures, as suggested by Schuler et al. (2006). NLTE corrections were performed by interpolating within the grids of Takeda (2003). The results of these corrections are presented in Table 5.3 and in Figure 5.5, where forbidden minus permitted [O/H] differences versus temperature are plotted. Notice that as the temperature decreases, the abundance from the redder lines of the triplet appear to be enhanced relative to the forbidden line. While the NLTE corrections decreased the abundance enhancements in the cooler stars of the sample, they did not eliminate them. This yields further evidence that there are distinct blending effects in the red lines of the triplet as a function of cooling temperature. Furthermore, the observations of the enhancements in both dwarf and giant stars may suggest that the effect is not evolutionary in origin. The nature of this blend should be explored in future work, but for the purposes of this dissertation, the oxygen abundances derived from the red features of the triplet will not be used.

In Figure 5.6 the difference in abundance from the forbidden oxygen line (6300.34 Å) and the NLTE corrected blue triplet line (7771 Å) is plotted versus temperature (top plot) and surface gravity (bottom plot). The dotted line shows a zero difference between the two abundances. The NLTE-corrected permitted oxygen abundances (7771 Å) appear to agree well with the forbidden oxygen abundance (6300 Å) indicating that the blue line

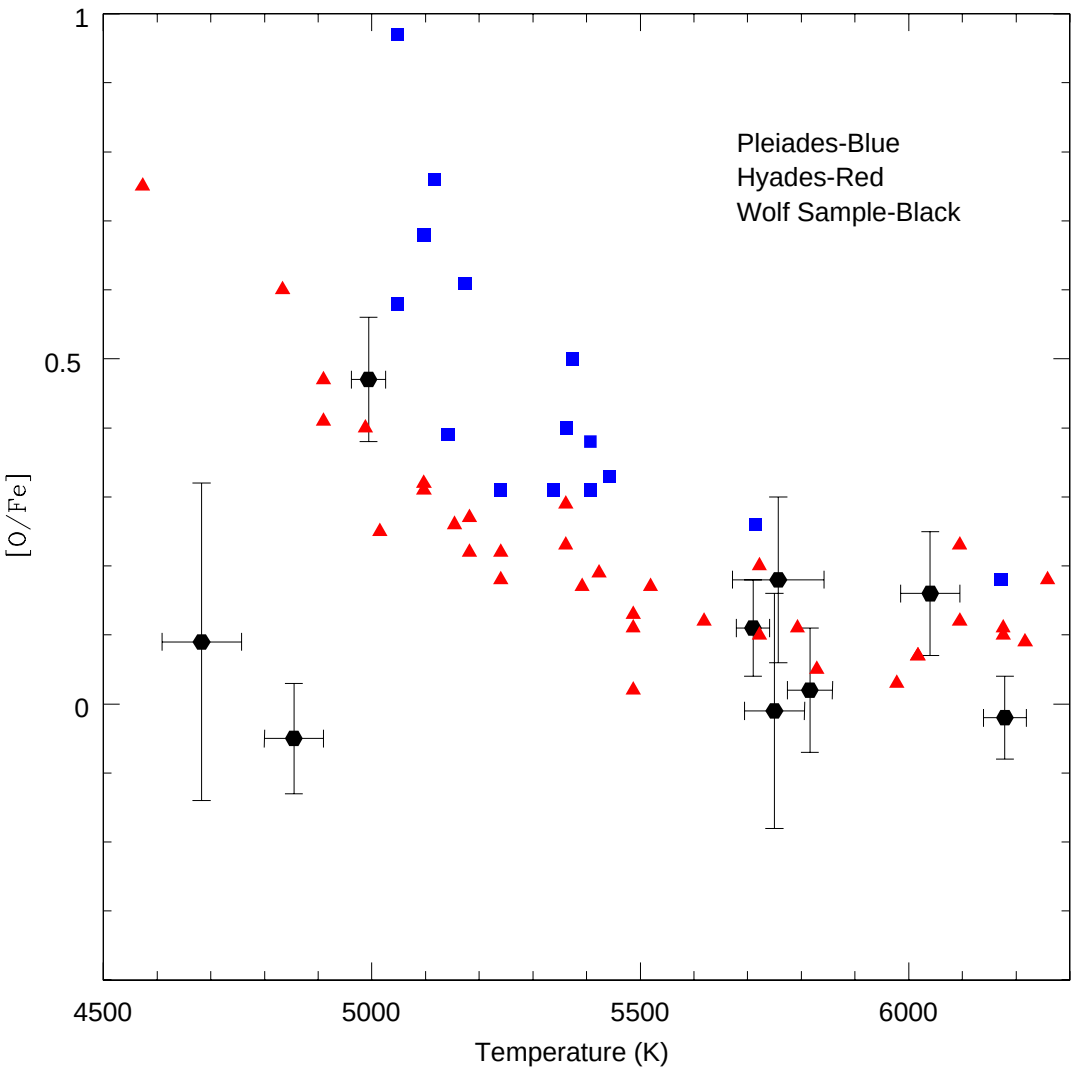

Figure 5.4 Oxygen abundances [O/Fe] versus temperature for the Wolf 630 sample (black), the Pleiades (blue) and the Hyades (red). The position of the Wolf stars in the plot is not inconsistent with an age dependent trend, where [O/Fe] abundances become less enhanced as a function of increasing age, perhaps suggesting that the Wolf stars are at least older than the Hyades.

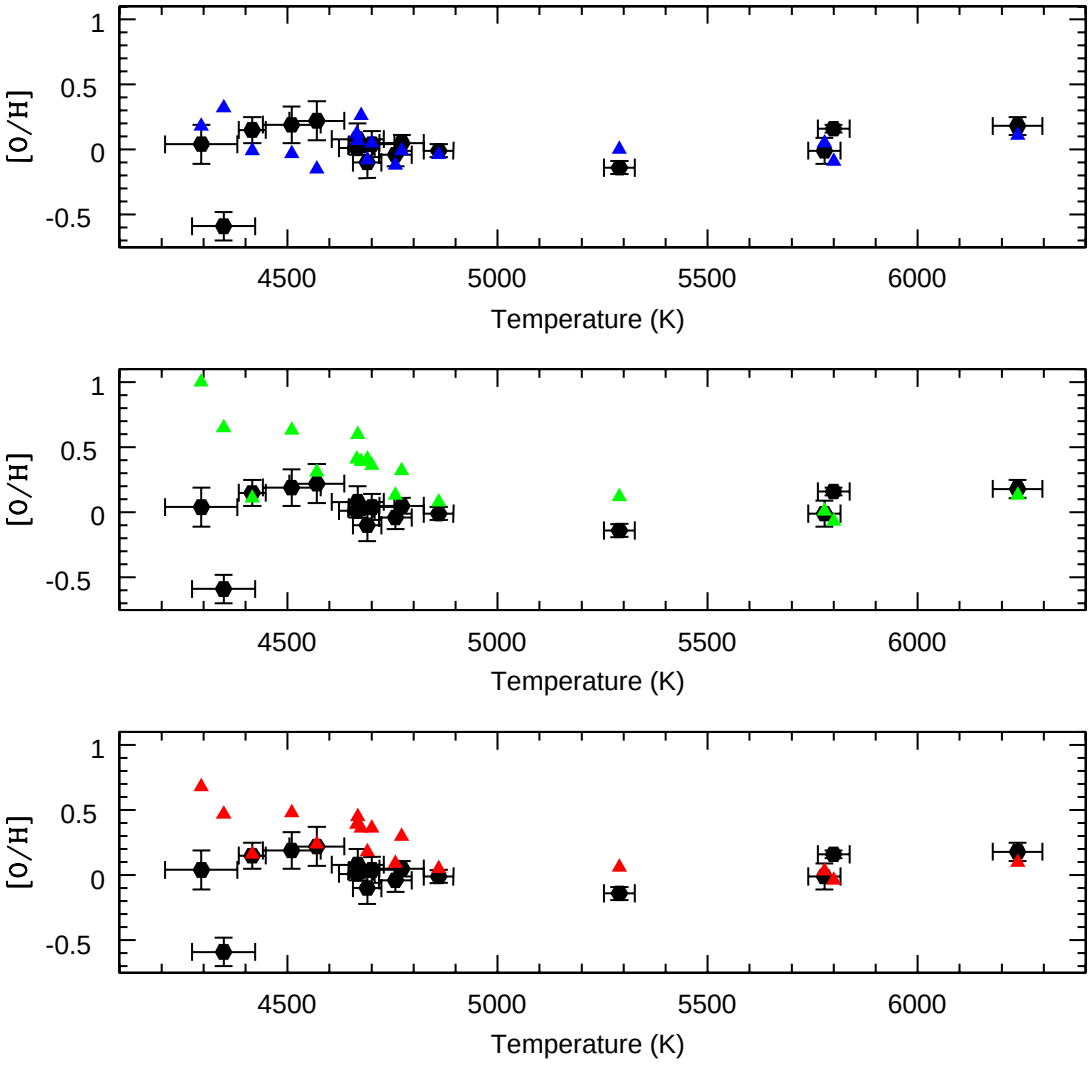

Figure 5.5 The [O/H] abundance for the forbidden line (black dots) is plotted versus temperature in all windows. The top plot shows the NLTE corrected [O/H] abundances from the 7771 line of the triplet (blue triangles), the middle plot shows the NLTE correct [O/H] from the 7774 line of the triplet (green triangles) and the bottom plot gives NLTE corrected [O/H] from the 7775 line (red triangles). Notice that the abundances derived from the 7771 line agree well, after NLTE corrections, with abundances from the forbidden line. Also notice the distinct increasing [O/H] abundance from the redder lines of the triplet as a function of decreasing temperature.

of the triplet can provide a reliable oxygen abundance when proper care is taken to make the necessary NLTE corrections.

The single outlier is HIP 114155. The larger than expected abundance from the triplet feature in this star is believed to be from NLTE effects that are not removed using the corrections of Takeda (2003) as the grid for the corrections does not extend below 4500 K. While the temperature extrapolation is sufficient for less evolved stars (i.e. NLTE triplet abundance in stars with surface gravities above 2.0 all agree with the the forbidden abundance, even at temperatures below 4500 K), the corrections for more evolved stars, with surface gravities $\sim$1.00, are significantly larger. The good agreement between all other forbidden and blue triplet oxygen abundances, therefore, points to the possible inadequacy of the NLTE corrections in cool, evolved stars.

The final salient point to make regarding the oxygen abundances is to address the alleged CN blending feature previously discussed. As mentioned, Davis & Phillips (1963) list CN features at 6300.265 Å and two features at 6300.482 Å with gf values of 5.78E-3, 6.82E-3 and 2.01E-3. Recall that the inability to adequately calibrate a linelist including these features with a high resolution solar atlas of Arcturus led to the features not being utilized in the derivation of forbidden line oxygen abundances. With the good agreement between forbidden oxygen neglecting the CN features and the NLTE corrected blue line of the triplet in Figure 5.6, it is suggested that the CN blending feature is either not real, or has no effect in the giant stars.

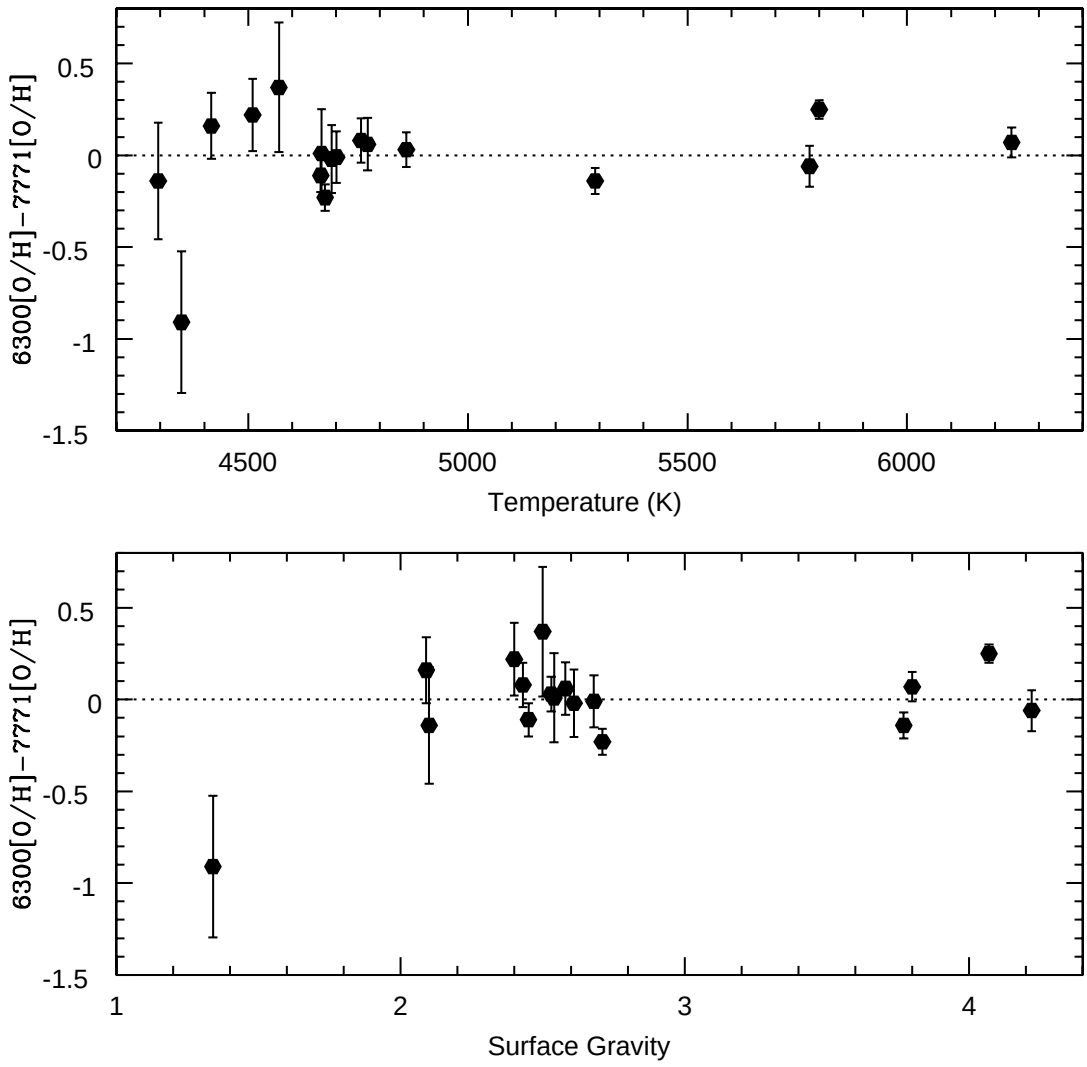

Figure 5.6 Differences in oxygen abundance between the forbidden line at 6300 Å and 7771 Å. The NLTE corrected abundances from the triplet line generally agree with the 6300 forbidden line, with the exception of the metal weak cool star, HIP 114155. The clear agreement between the forbidden and the NLTE triplet abundance until reaching a low surface gravity possibly indicates that greater than expected NLTE effects impact the triplet abundances in more evolved stars.

CHAPTER 6

CONCLUSIONS

Spatially unassociated groups of stars moving through the solar neighborhood with common U and V kinematics have been known about for over half a century (Eggen, 1958). Despite this long history, the exact origins of these so called moving groups is still a matter of some debate. The classical view contends that they are dissolved open clusters which have retained common kinematics and drifted into spatially elongated stellar streams. If this is indeed true, moving group members should possess similar characteristics to those of open cluster stars; particularly common chemical abundances and residence along a distinct evolutionary sequence in an HR diagram.

In order to address the viability of moving groups being dissolved open clusters, this dissertation has performed a high resolution spectroscopic abundance analysis of a 34 star sample of the kinematically distinct Wolf 630 moving group, selected for its residence in a sparsely populated region of the kinematic UV plane in the solar neighborhood. With these high quality abundance measurements, the entire sample has been confirmed to not be characterized by a single chemical abundance. To rigorously evaluate the group members for chemical homogeneity, the individual stars have been closely scrutinized, making use of abundances, evolutionary state and qualitative age information to constrain membership as an unlikely, possible or likely member of a subsample with a dominant abundance trend. There appears to be a group with a weighted mean of [Fe/H]=-0.01 $\pm$ 0.02 (uncertainty in the weighted mean) which is composed of 21 stars. These final members are well traced by an evolutionary sequence of 2.7 $\pm$ 0.5 Gyr as determined from fitting by Yale-Yonsei isochrones (Demarque et al., 2004).

Additionally, simple NBODY simulations of open cluster models in a Galactic potential have been performed to explore the dynamical evolution of an open cluster dissolving in a galactic disk potential studded with giant molecular clouds. The simulations suggest

that open clusters maintain kinematic cohesion after spatially dispersing into the field, validating the classical picture of moving group formation. These models also demonstrate the importance of the position of the Sun in allowing identification of distinct moving groups within the general solar neighborhood. Further results show that with an appropriate choice of initial conditions, the simple NBODY models used can recreate moving group structures similar to the Wolf 630 moving group. Finally, a cursory analysis of an exponential Milky Way disk suggests that field stars can populate the distinct Wolf 630 region of phase space. This perhaps points to the chemically deviant members of the Wolf group being bona-fide field star interlopers.

The big picture that emerges from this work is that open clusters can maintain a common kinematic identity after spatial dissolution into the field. If the Sun is in a favorable position relative to the stellar streams formed from open cluster evaporation, then a distinct moving group can be discerned. Due to the presence of background field star contamination, in order to rigorously constrain a moving group's members as relics of a dissolved cluster, precise chemical abundances should be obtained and a unique chemical signature determined to complement the kinematic cohesion.

CHAPTER 7

SUPPLEMENTARY PLOTS

The smoothed abundance distributions and abundance band homogeneity plots for Al, Ba, Ca, Cr, Mg, Mn, Na, Ni, Si, Ti and Ti2 are presented here. The stars plotted are in the final "possible" and "likely" group member sample.

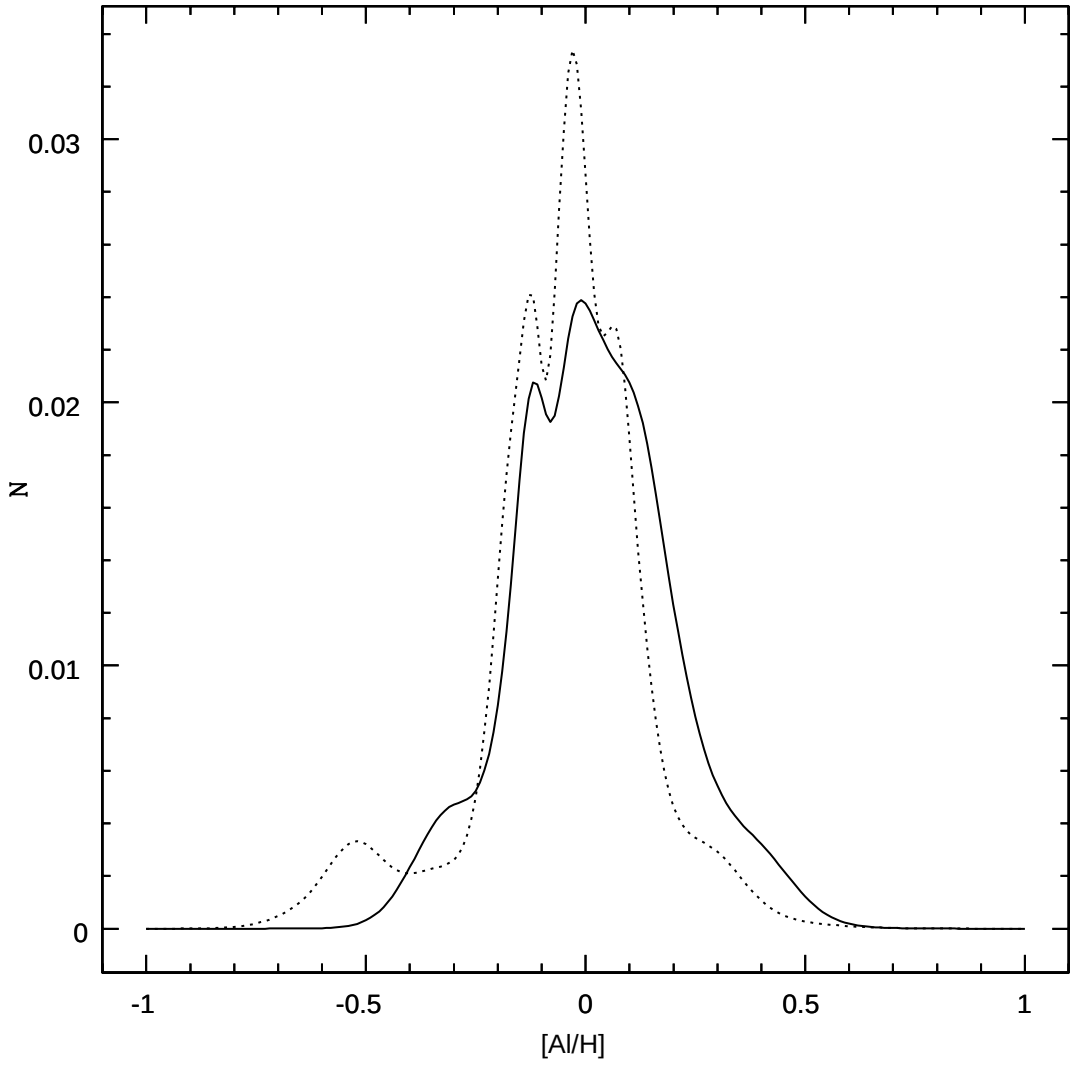

Figure 7.1 Smoothed distribution of Al for the whole sample (solid) with smooth distribution for Fe (dotted).

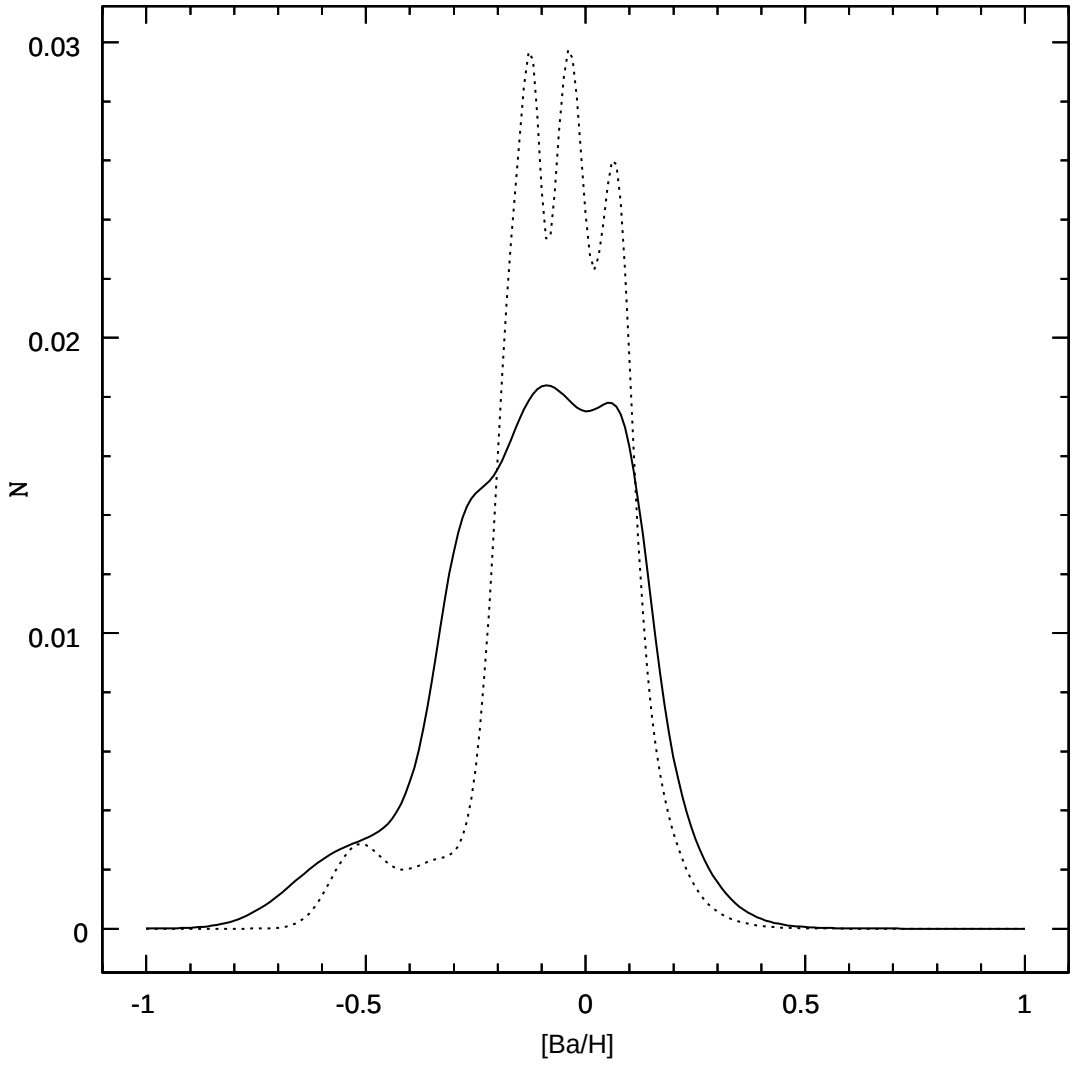

Figure 7.2 Smoothed distribution of Ba for the whole sample (solid) with smooth distribution for Fe (dotted).

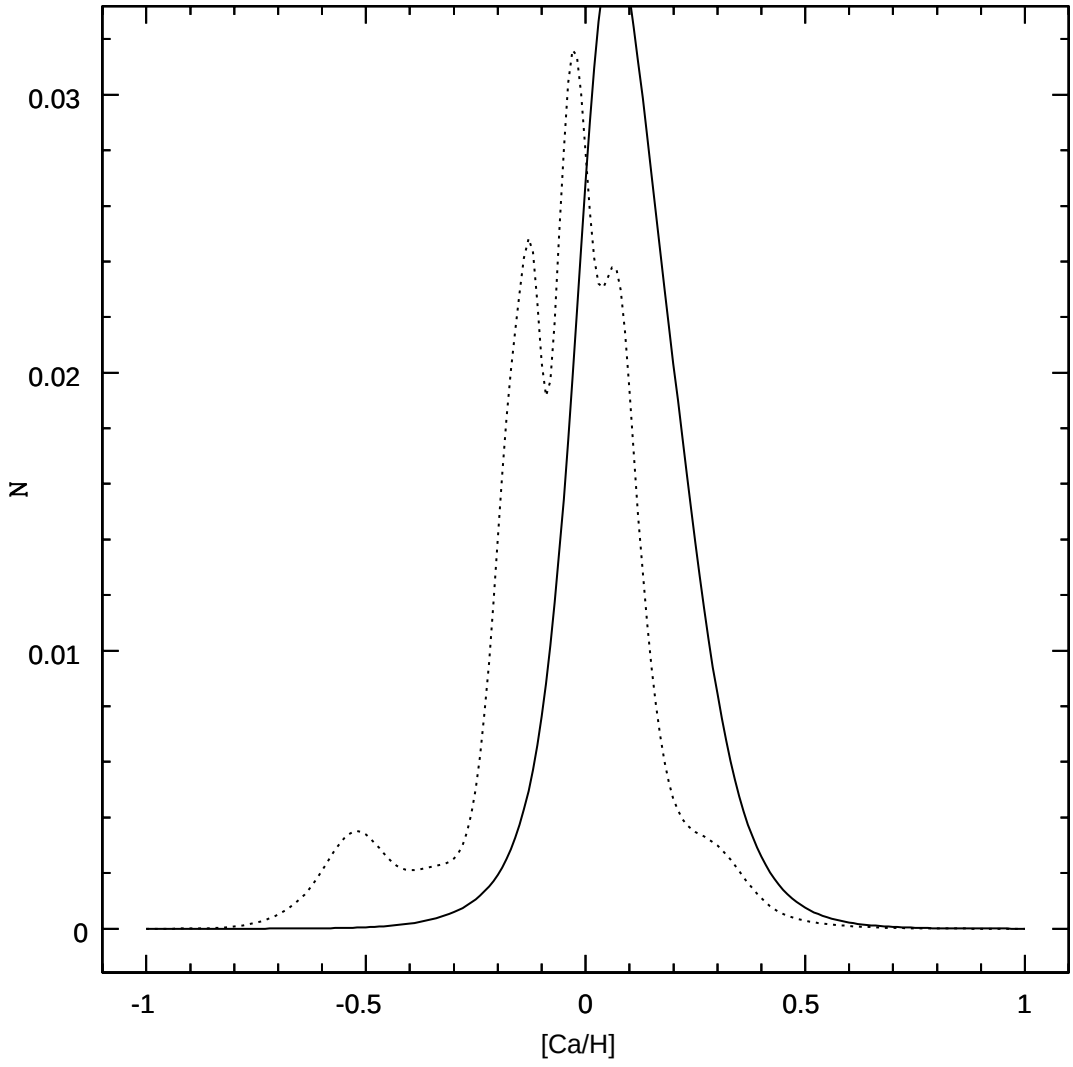

Figure 7.3 Smoothed distribution of Ca for the whole sample (solid) with smooth distribution for Fe (dotted).

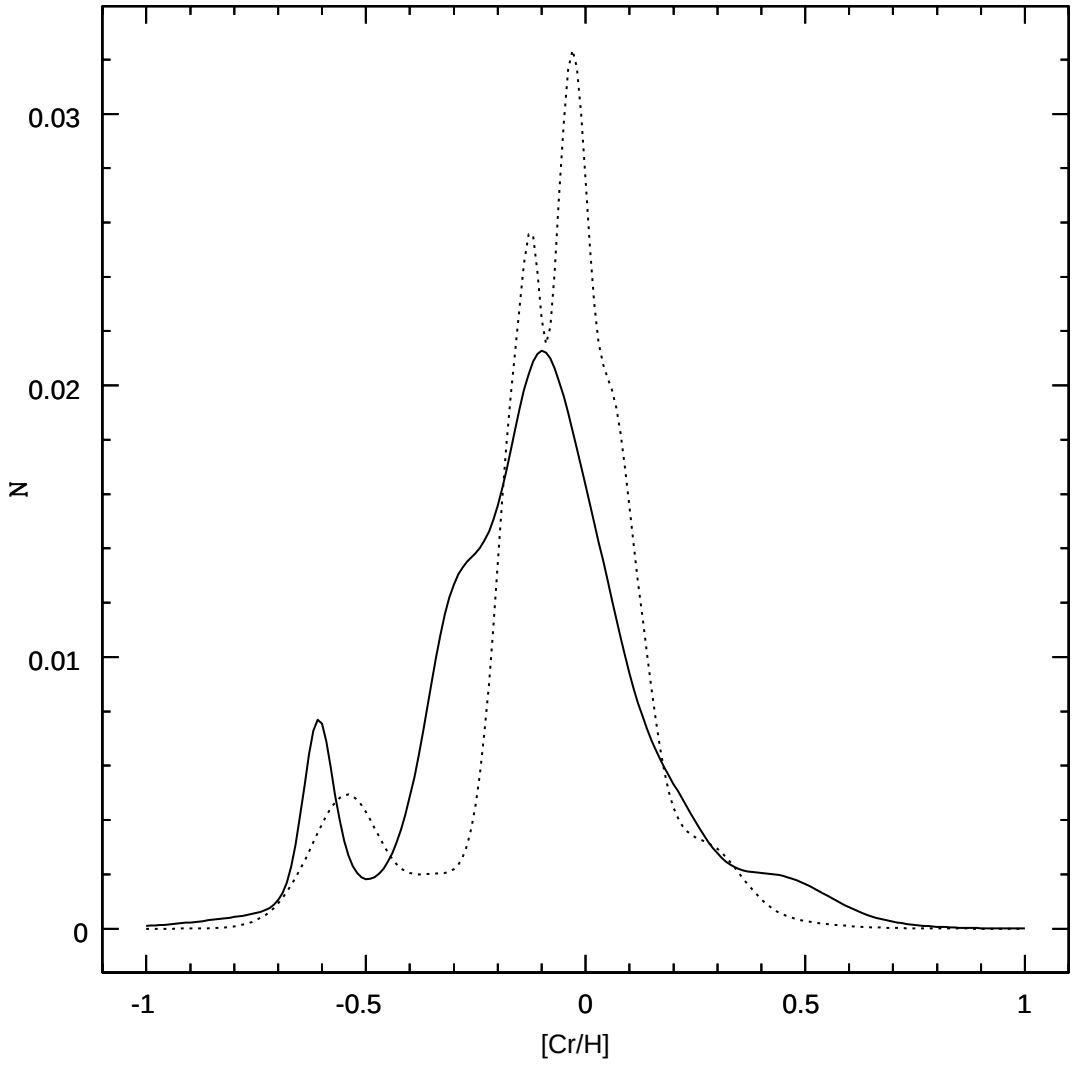

Figure 7.4 Smoothed distribution of Cr for the whole sample (solid) with smooth distribution for Fe (dotted).

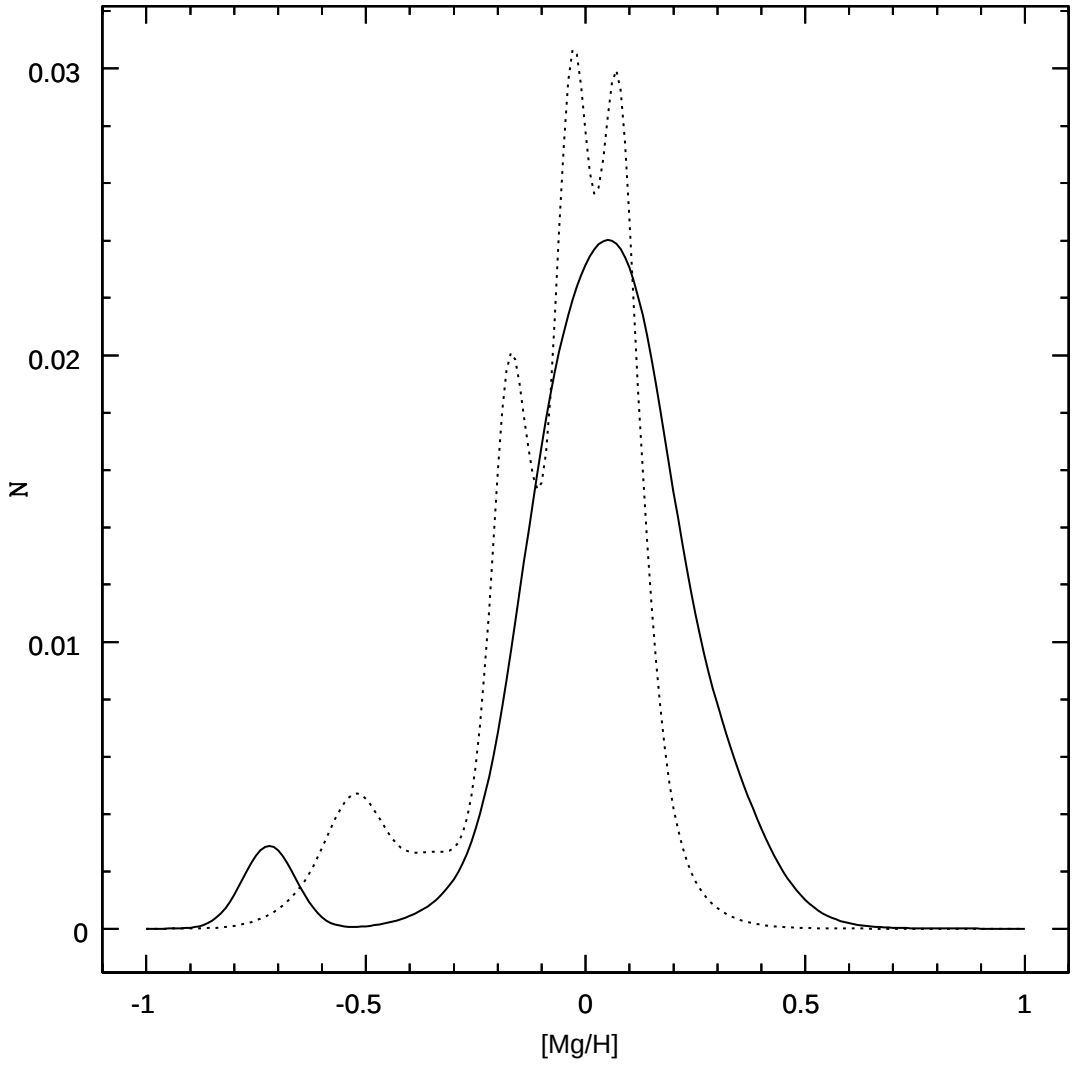

Figure 7.5 Smoothed distribution of Mg for the whole sample (solid) with smooth distribution for Fe (dotted).

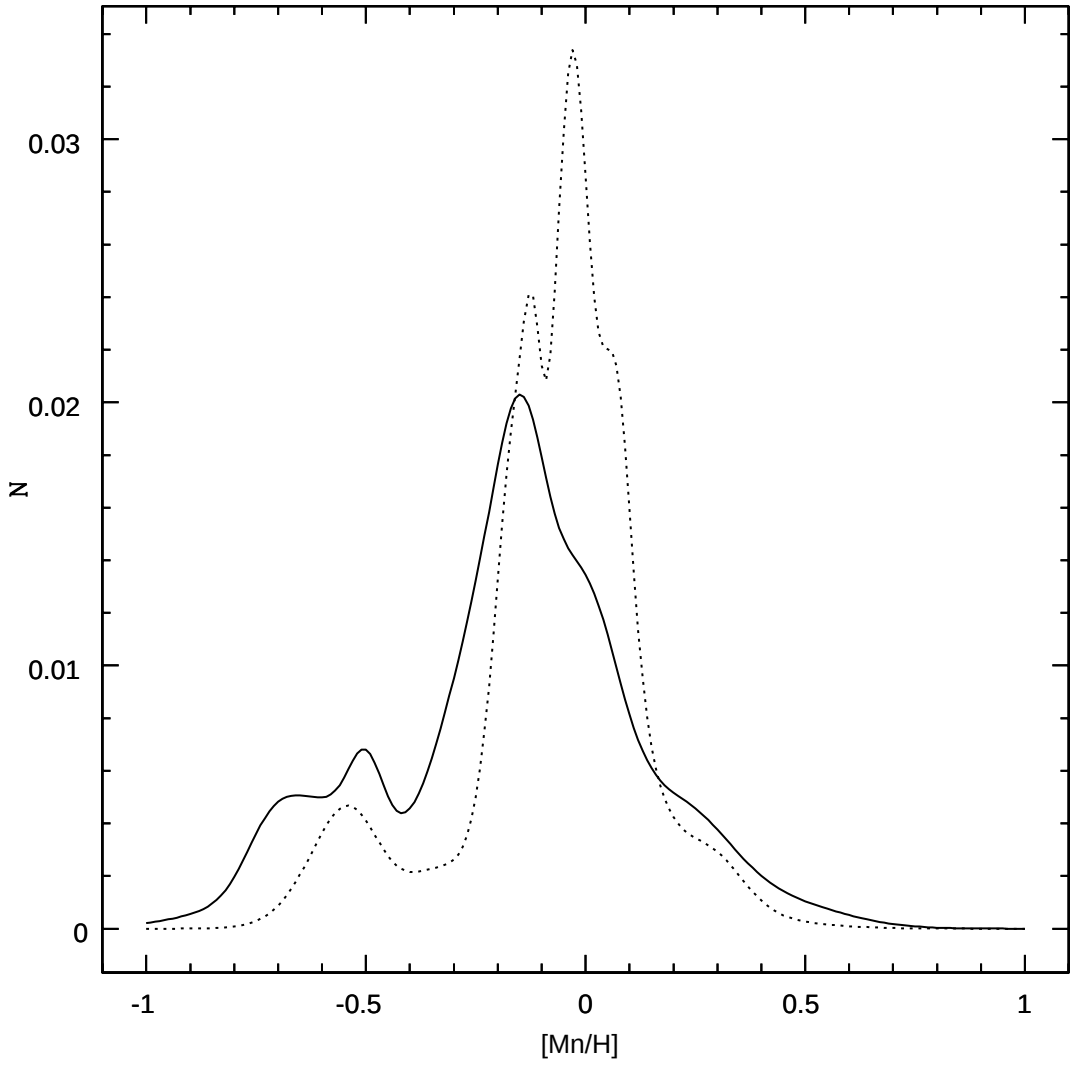

Figure 7.6 Smoothed distribution of Mn for the whole sample (solid) with smooth distribution for Fe (dotted).

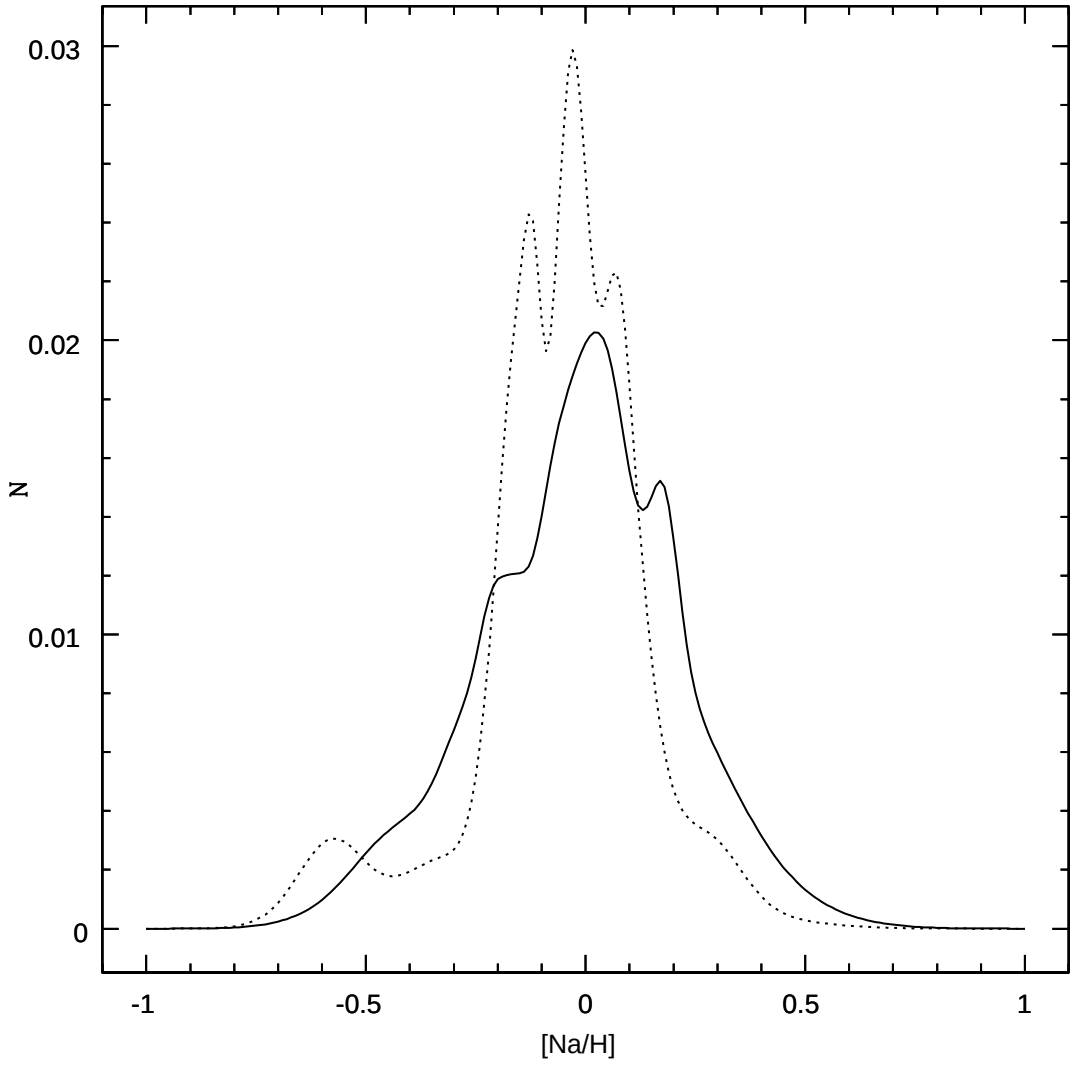

Figure 7.7 Smoothed distribution of Na for the whole sample (solid) with smooth distribution for Fe (dotted).

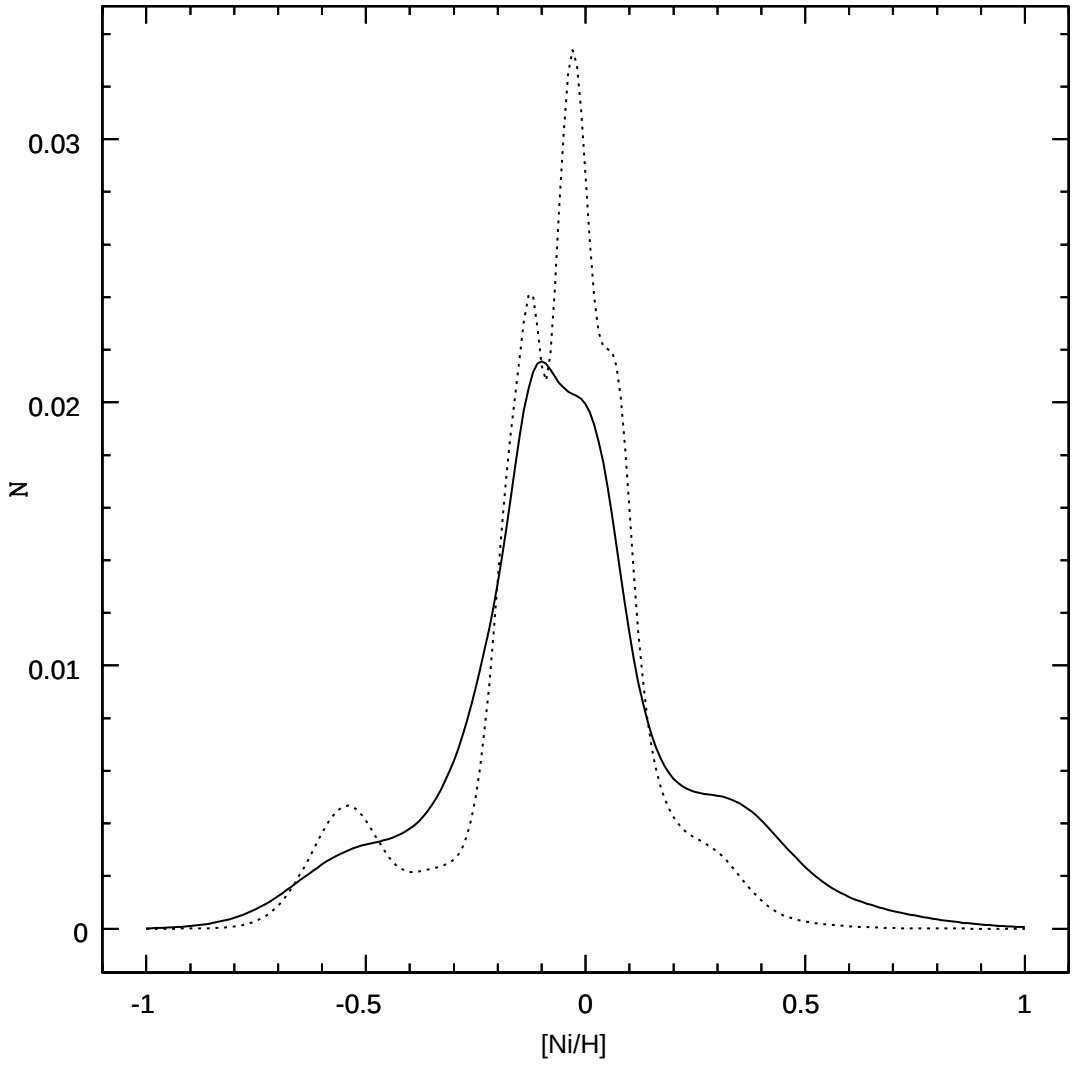

Figure 7.8 Smoothed distribution of Ni for the whole sample (solid) with smooth distribution for Fe (dotted).

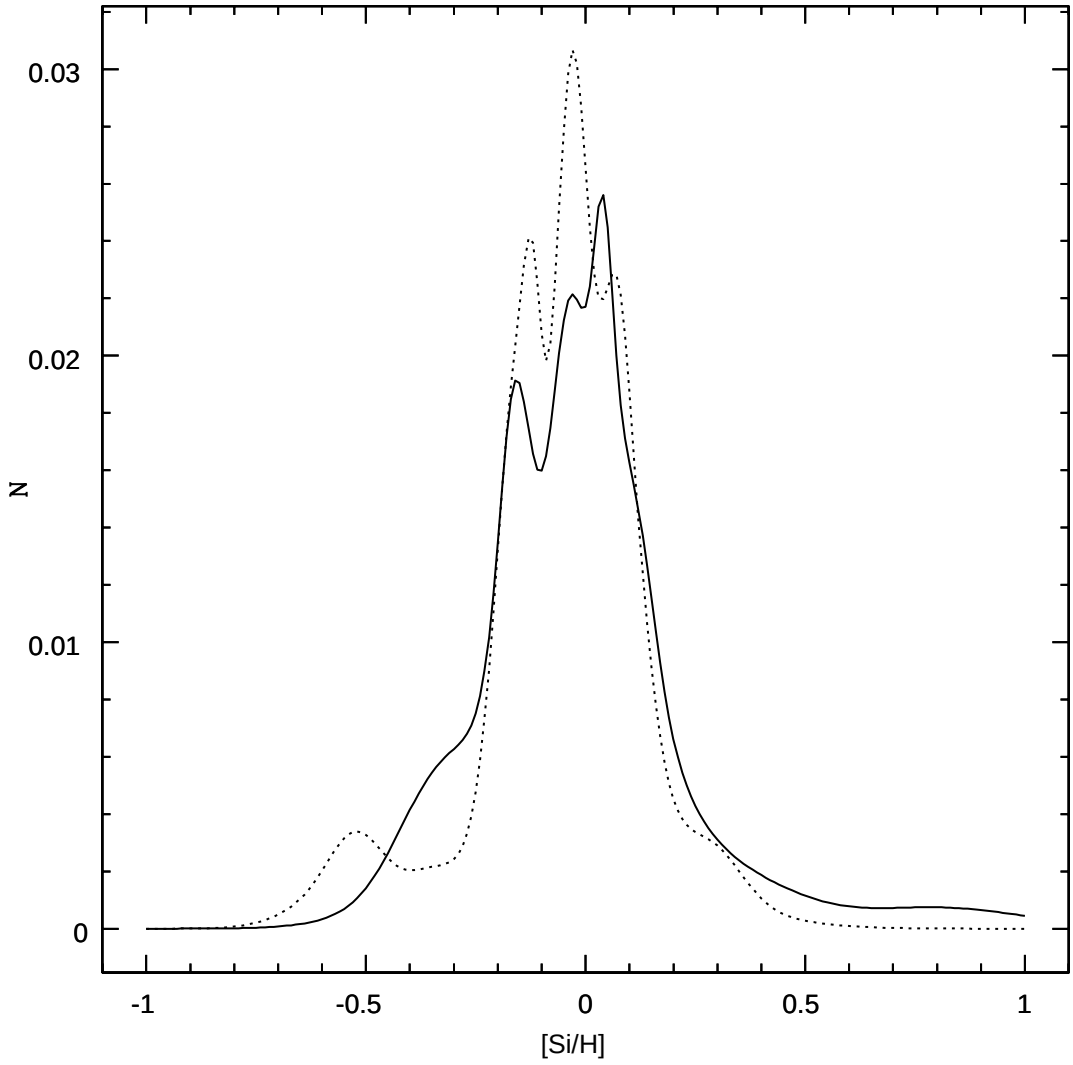

Figure 7.9 Smoothed distribution of Si for the whole sample (solid) with smooth distribution for Fe (dotted).

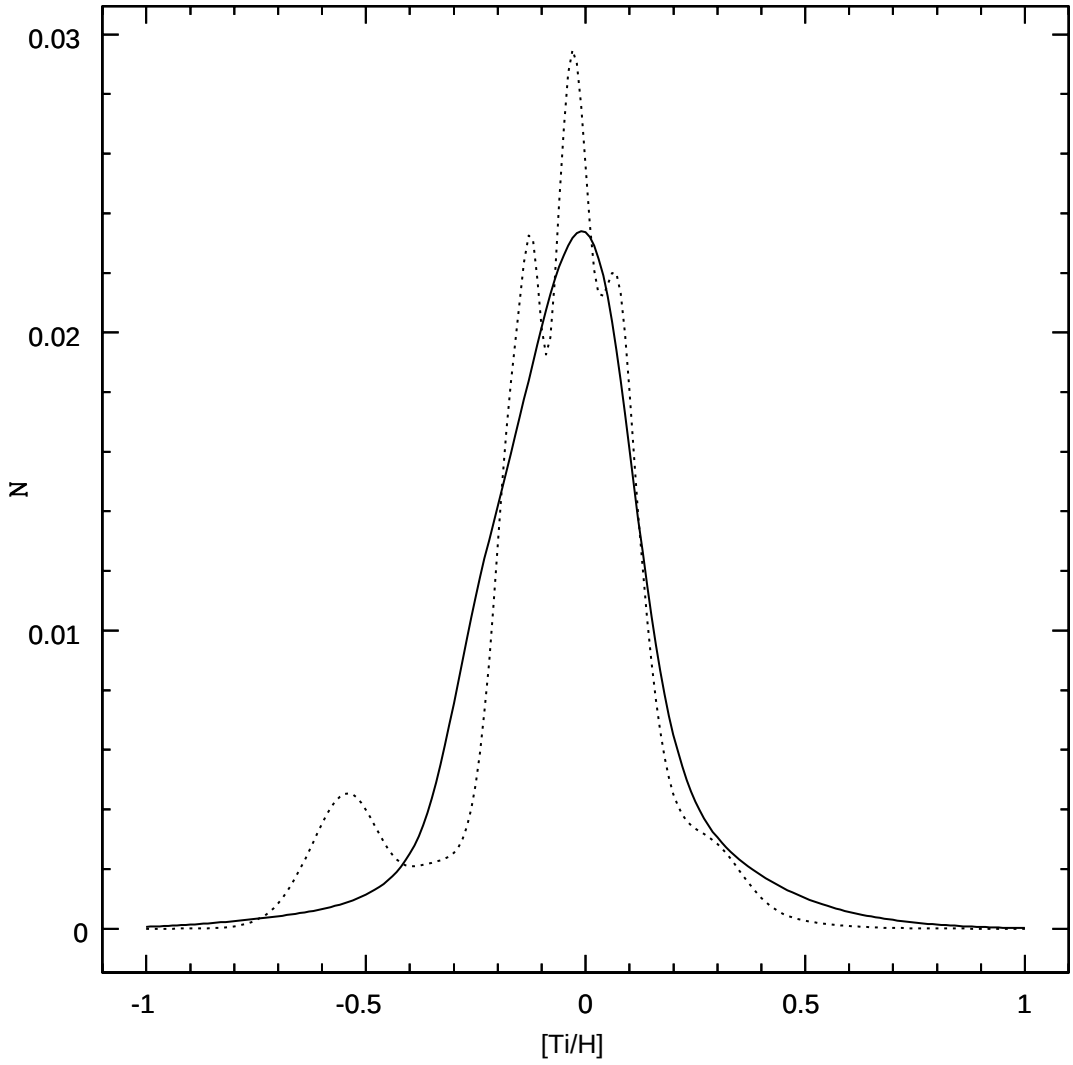

Figure 7.10 Smoothed distribution of Ti for the whole sample (solid) with smooth distribution for Fe (dotted).

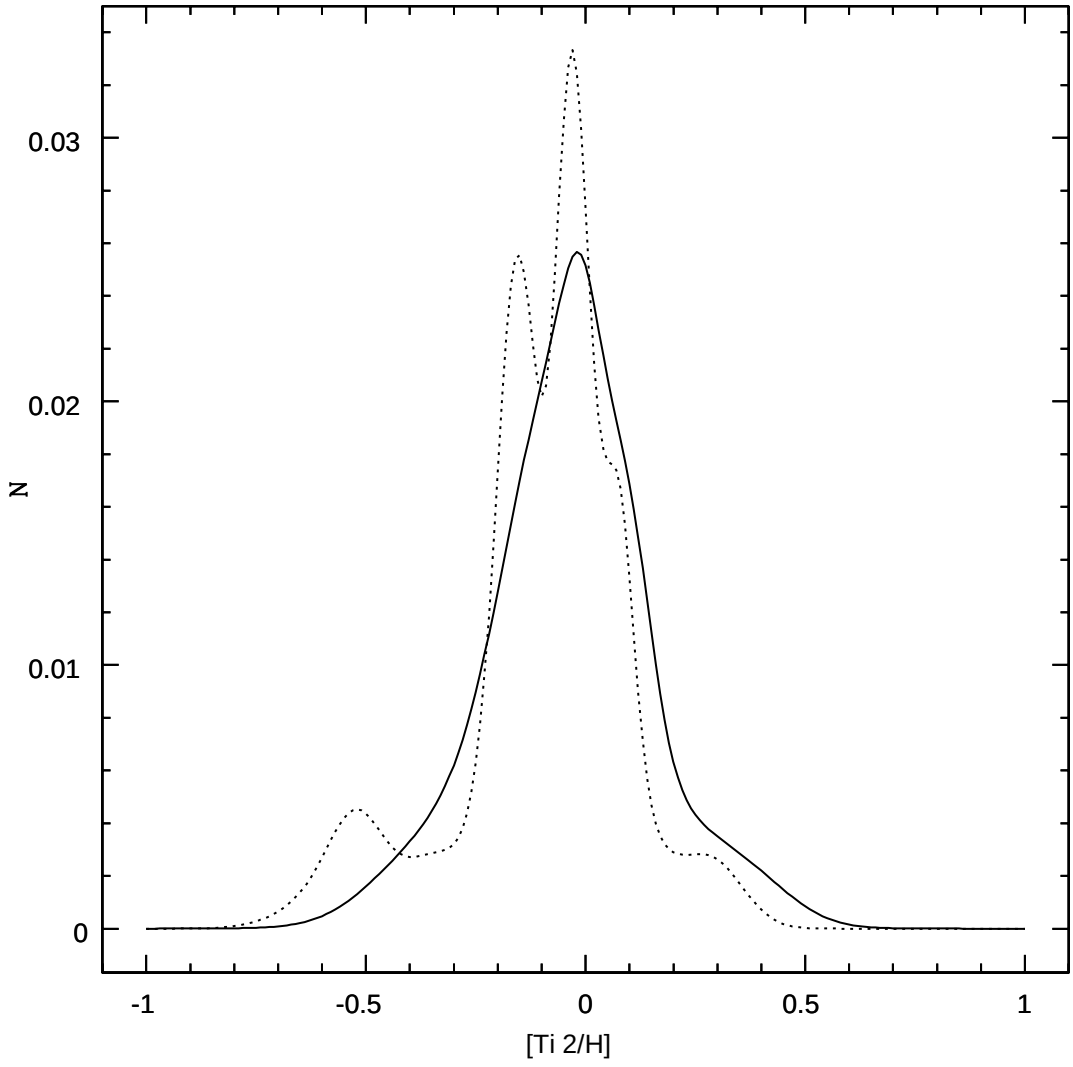

Figure 7.11 Smoothed distribution of Ti2 for the whole sample (solid) with smooth distribution for Fe (dotted).

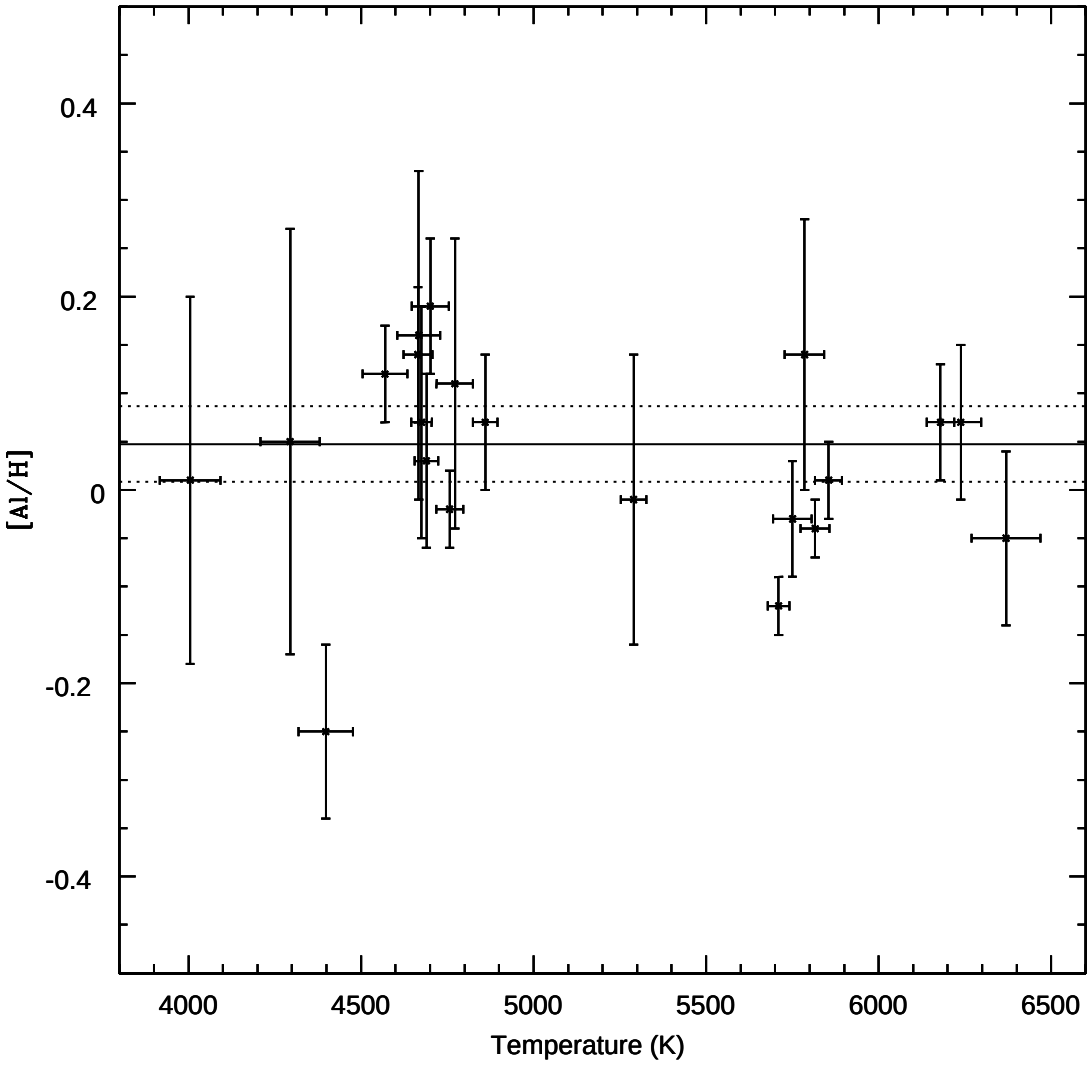

Figure 7.12 The [Al/H] for the stars that are labeled possible or likely members of a dominant homogeneous sample are plotted versus temperature. The solid line gives the weighted mean of the sample while the dotted lines are 3-σ deviations from this mean. If a star rests within the dotted lines (i.e. the abundance band) within its respective uncertainty, then it is considered homogeneous with the dominant sample.

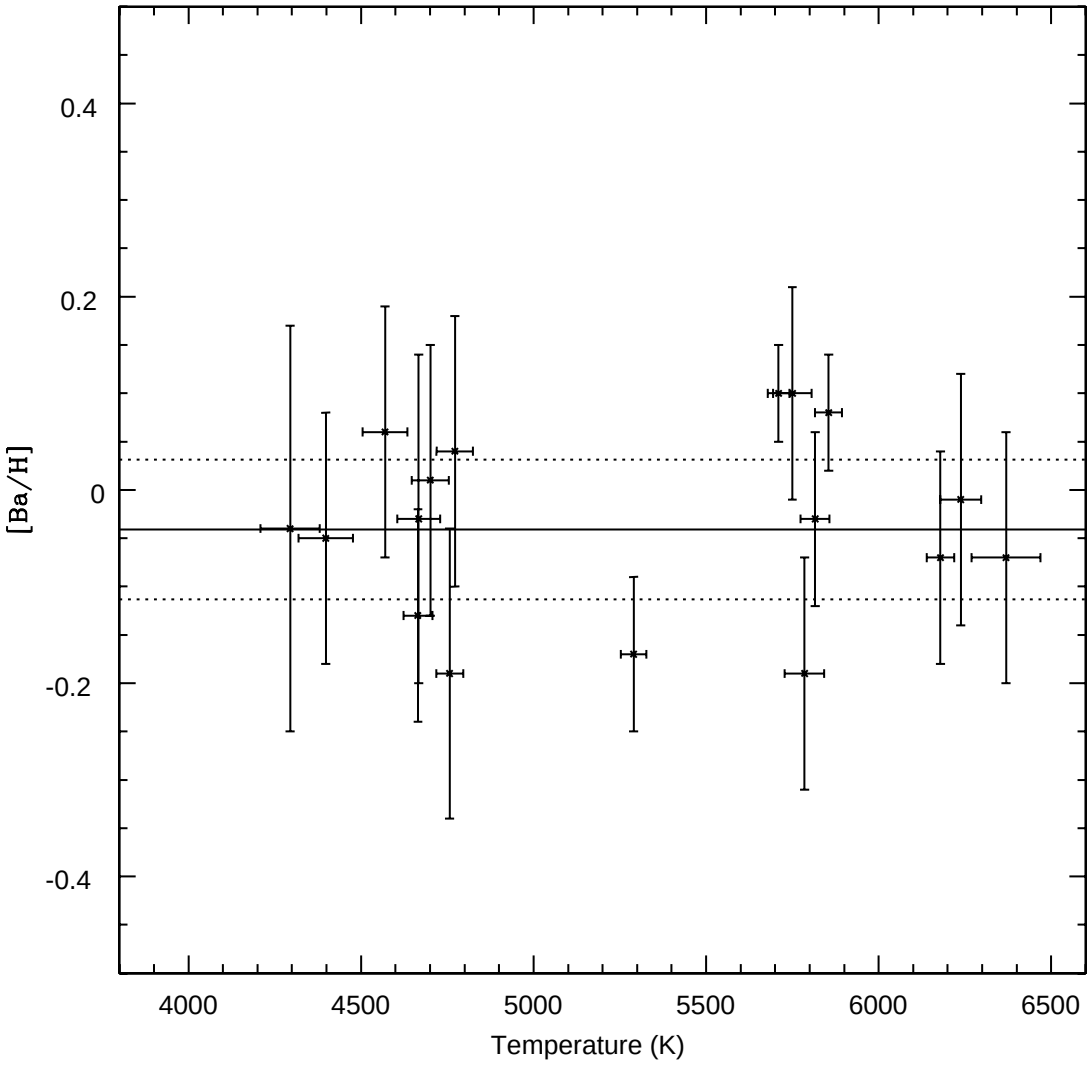

Figure 7.13 The [Ba/H] for the stars that are labeled possible or likely members of a dominant homogeneous sample are plotted versus temperature. The solid line gives the weighted mean of the sample while the dotted lines are 3-σ deviations from this mean. If a star rests within the dotted lines (i.e. the abundance band) within its respective uncertainty, then it is considered homogeneous with the dominant sample.

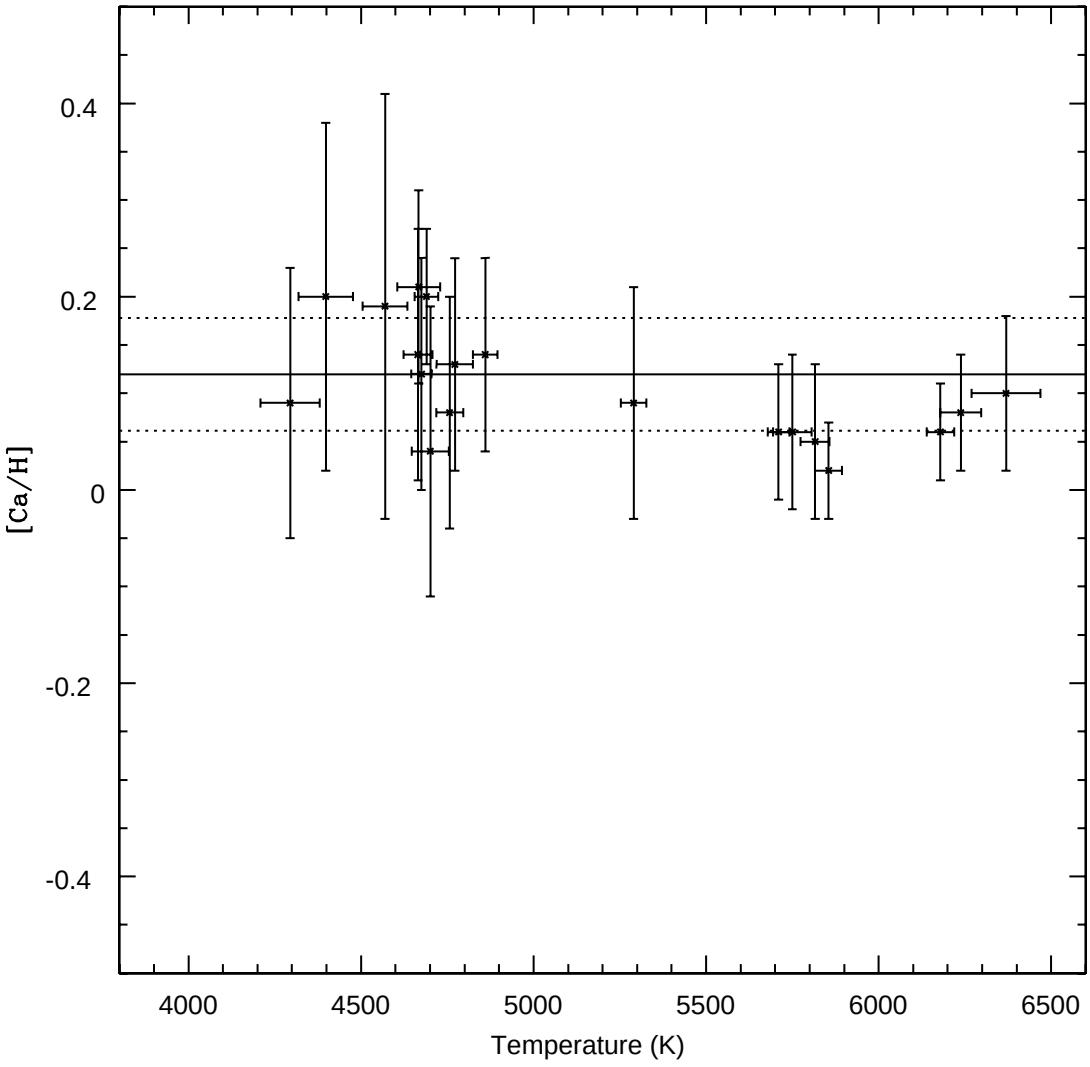

Figure 7.14 The [Ca/H] for the stars that are labeled possible or likely members of a dominant homogeneous sample are plotted versus temperature. The solid line gives the weighted mean of the sample while the dotted lines are 3-σ deviations from this mean. If a star rests within the dotted lines (i.e. the abundance band) within its respective uncertainty, then it is considered homogeneous with the dominant sample.

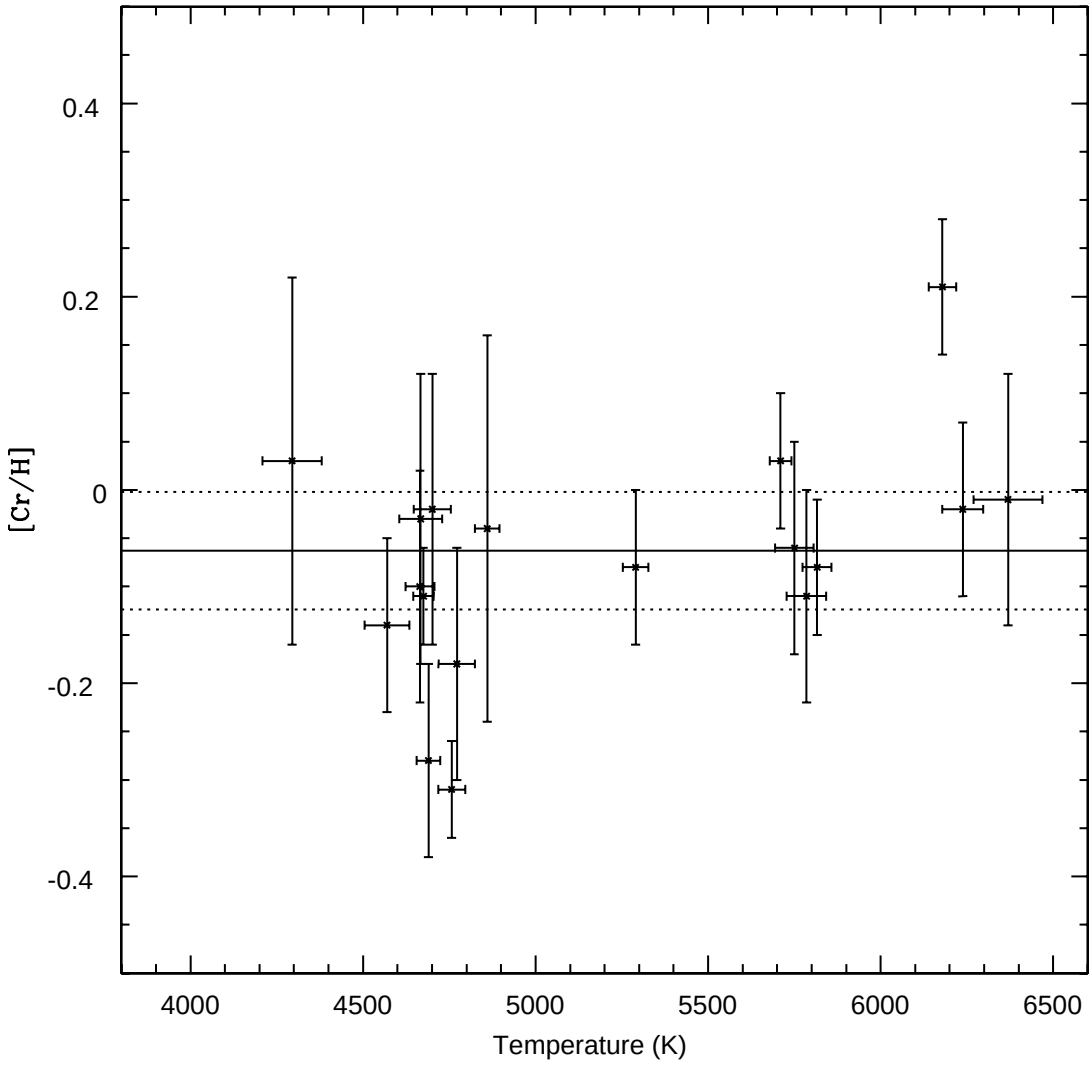

Figure 7.15 The [Cr/H] for the stars that are labeled possible or likely members of a dominant homogeneous sample are plotted versus temperature. The solid line gives the weighted mean of the sample while the dotted lines are 3-σ deviations from this mean. If a star rests within the dotted lines (i.e. the abundance band) within its respective uncertainty, then it is considered homogeneous with the dominant sample.

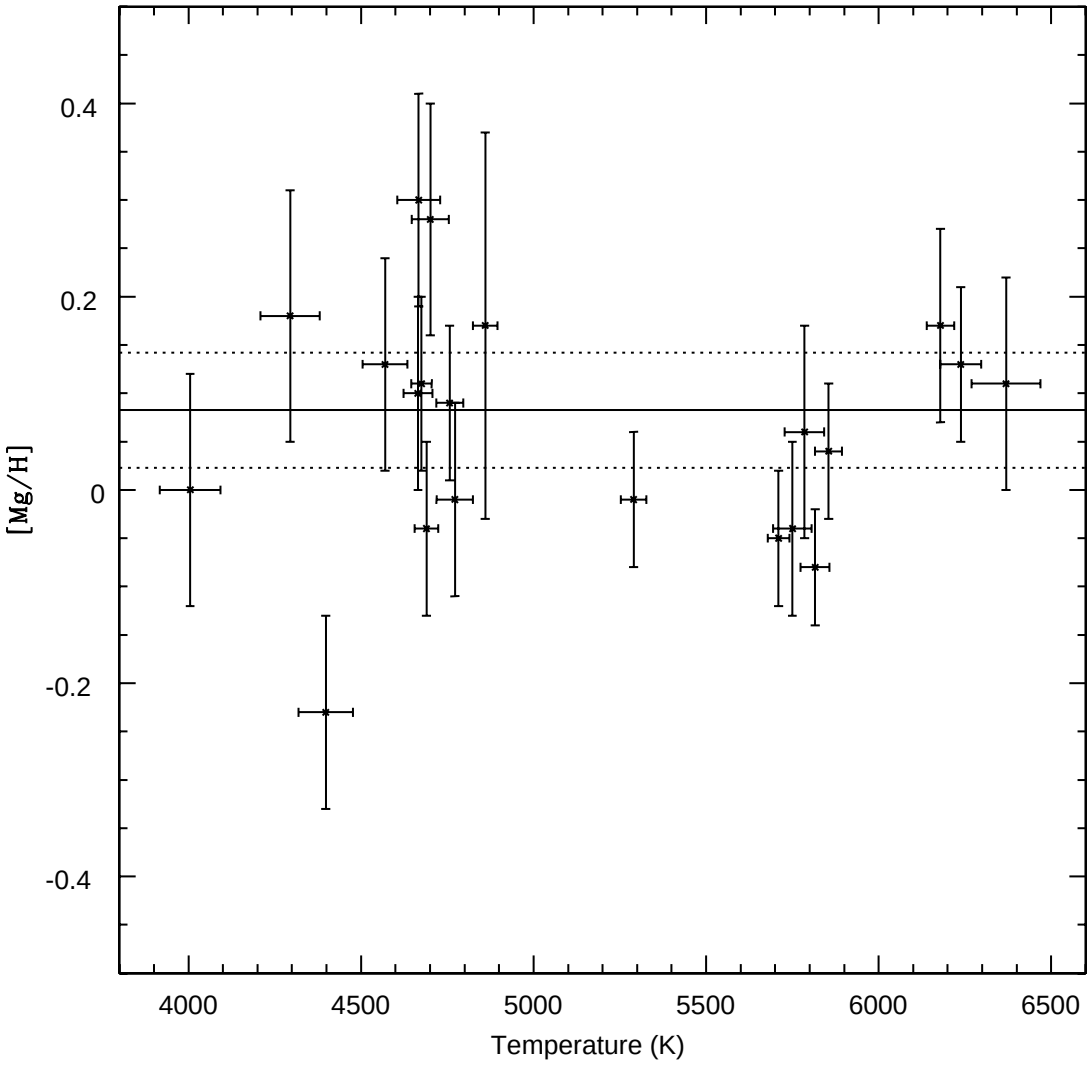

Figure 7.16 The [Mg/H] for the stars that are labeled possible or likely members of a dominant homogeneous sample are plotted versus temperature. The solid line gives the weighted mean of the sample while the dotted lines are 3-σ deviations from this mean. If a star rests within the dotted lines (i.e. the abundance band) within its respective uncertainty, then it is considered homogeneous with the dominant sample.

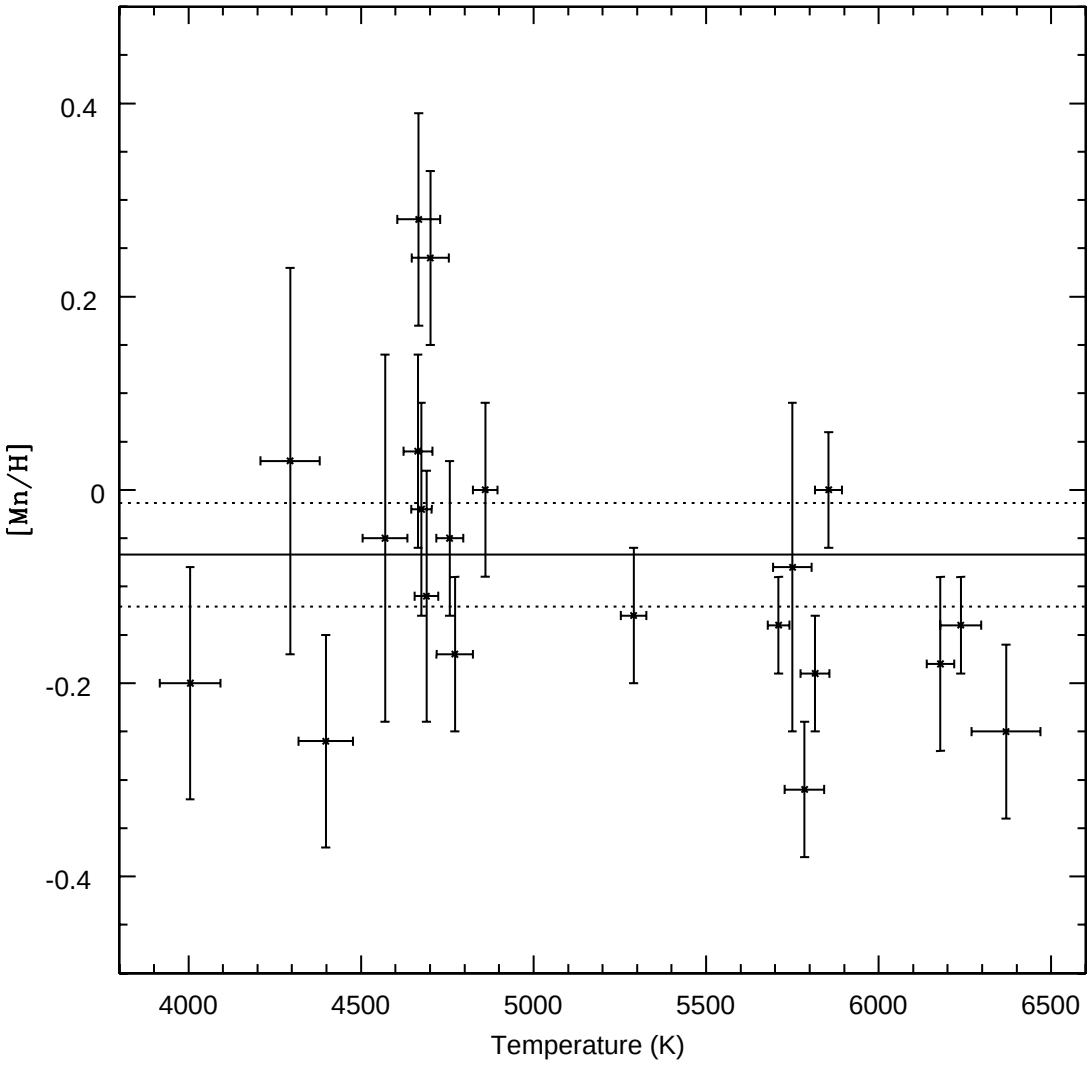

Figure 7.17 The [Mn/H] for the stars that are labeled possible or likely members of a dominant homogeneous sample are plotted versus temperature. The solid line gives the weighted mean of the sample while the dotted lines are 3-σ deviations from this mean. If a star rests within the dotted lines (i.e. the abundance band) within its respective uncertainty, then it is considered homogeneous with the dominant sample.

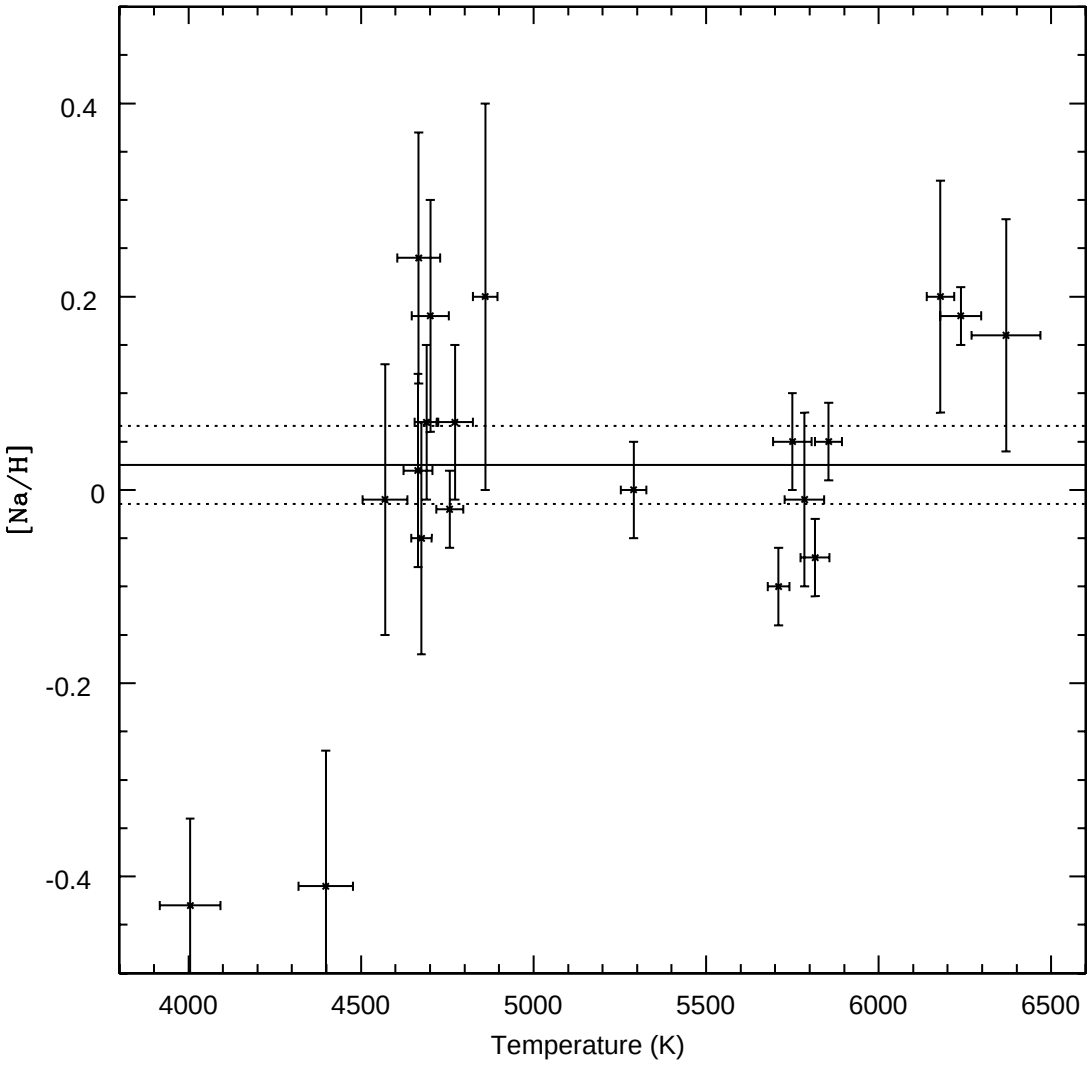

Figure 7.18 The [Na/H] for the stars that are labeled possible or likely members of a dominant homogeneous sample are plotted versus temperature. The solid line gives the weighted mean of the sample while the dotted lines are 3-σ deviations from this mean. If a star rests within the dotted lines (i.e. the abundance band) within its respective uncertainty, then it is considered homogeneous with the dominant sample.

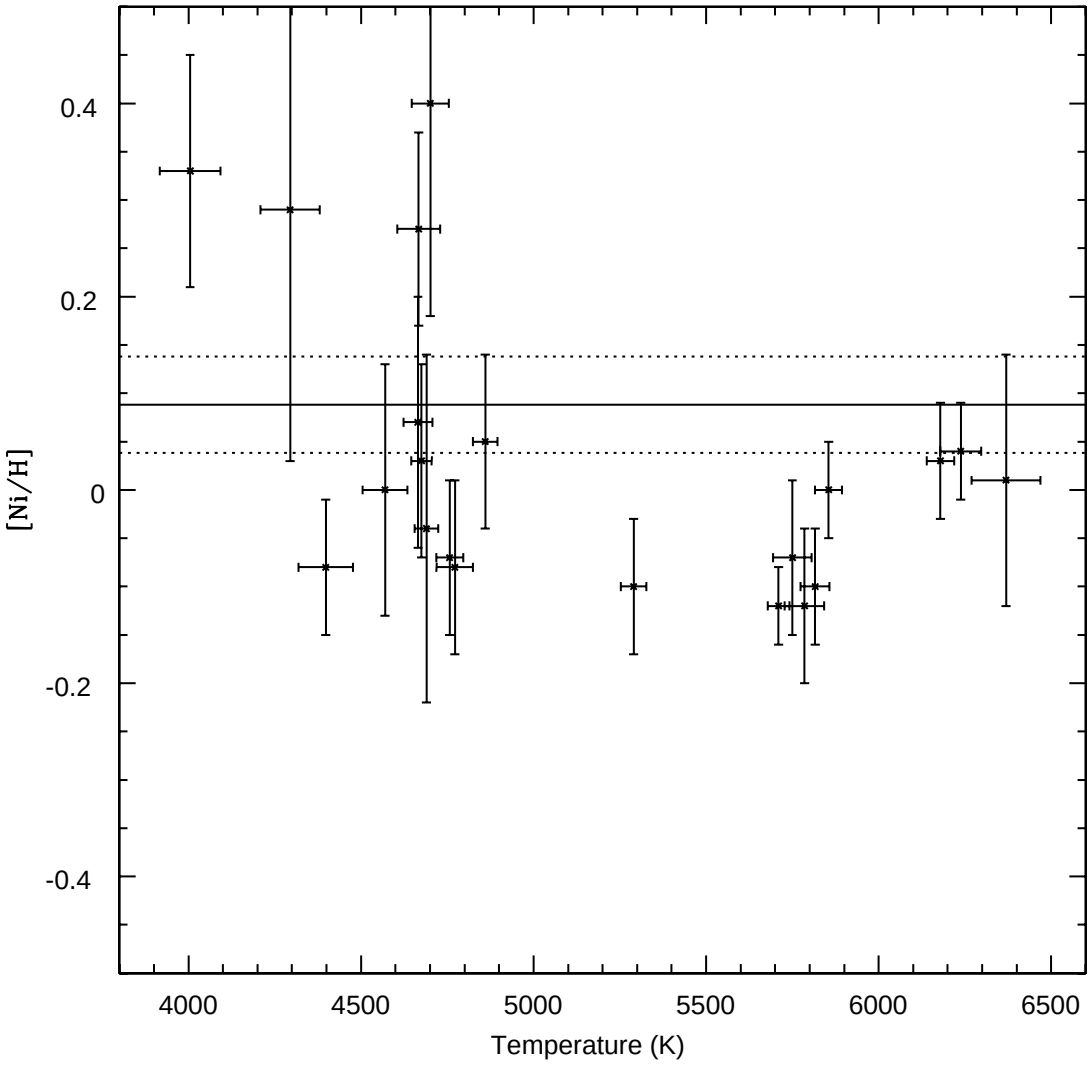

Figure 7.19 The [Ni/H] for the stars that are labeled possible or likely members of a dominant homogeneous sample are plotted versus temperature. The solid line gives the weighted mean of the sample while the dotted lines are 3-σ deviations from this mean. If a star rests within the dotted lines (i.e. the abundance band) within its respective uncertainty, then it is considered homogeneous with the dominant sample.

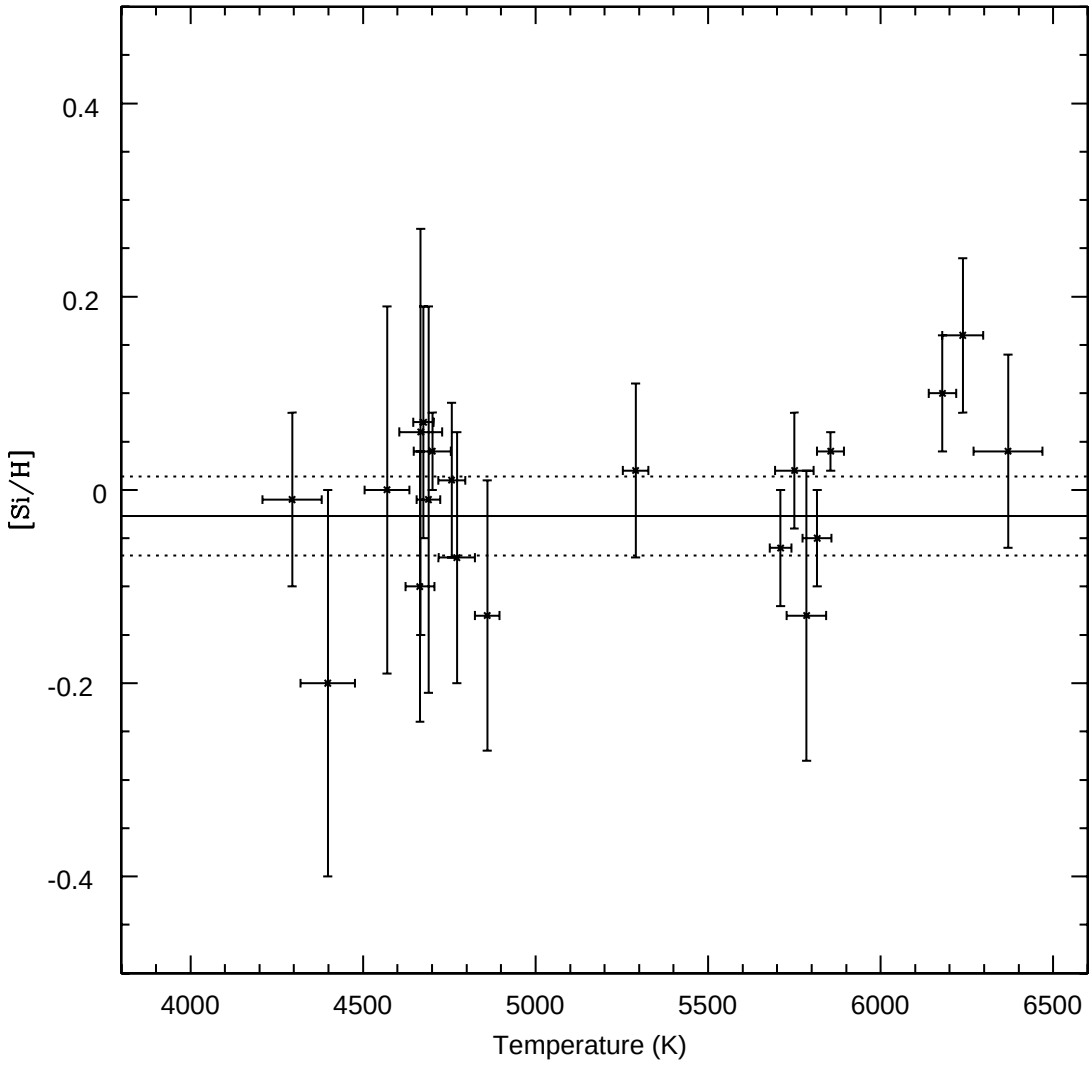

Figure 7.20 The [Si/H] for the stars that are labeled possible or likely members of a dominant homogeneous sample are plotted versus temperature. The solid line gives the weighted mean of the sample while the dotted lines are 3-σ deviations from this mean. If a star rests within the dotted lines (i.e. the abundance band) within its respective uncertainty, then it is considered homogeneous with the dominant sample.

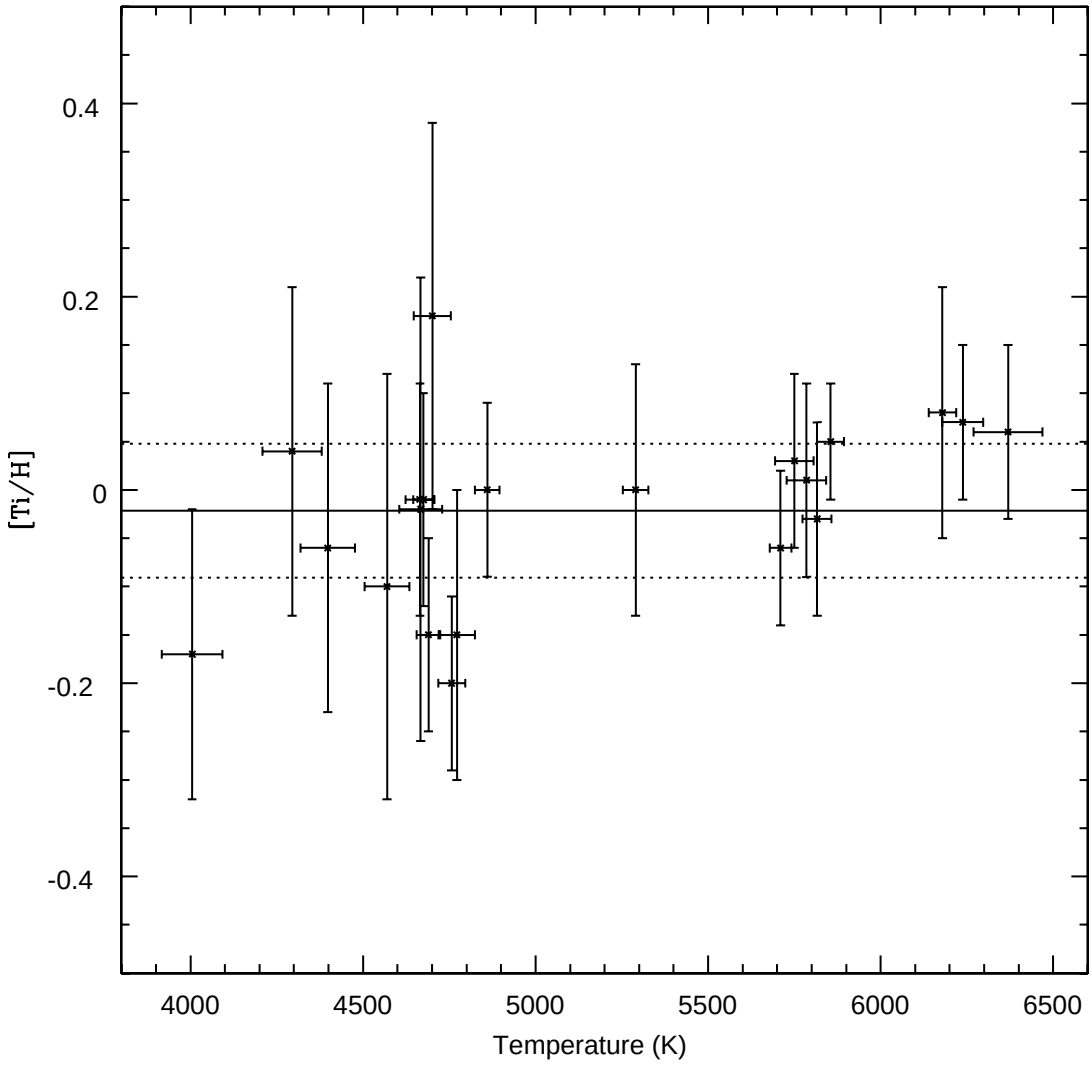

Figure 7.21 The [Ti/H] for the stars that are labeled possible or likely members of a dominant homogeneous sample are plotted versus temperature. The solid line gives the weighted mean of the sample while the dotted lines are 3-σ deviations from this mean. If a star rests within the dotted lines (i.e. the abundance band) within its respective uncertainty, then it is considered homogeneous with the dominant sample.

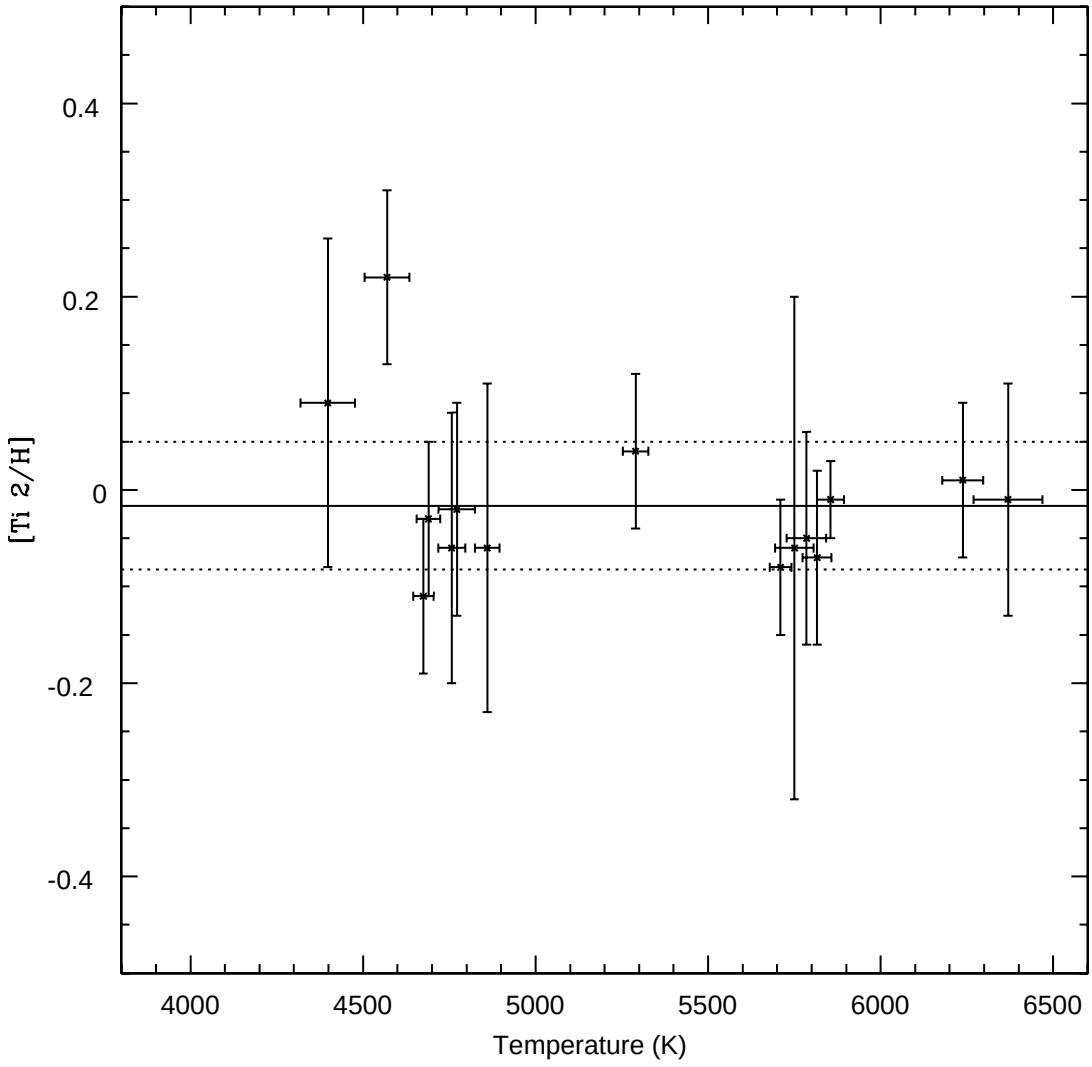

Figure 7.22 The [Ti 2/H] for the stars that are labeled possible or likely members of a dominant homogeneous sample are plotted versus temperature. The solid line gives the weighted mean of the sample while the dotted lines are 3-σ deviations from this mean. If a star rests within the dotted lines (i.e. the abundance band) within its respective uncertainty, then it is considered homogeneous with the dominant sample.

BIBLIOGRAPHY

Adams, F. C., & Myers, P. C. 2001, ApJ, 553, 744

Allende Prieto, C., Barklem, P. S., Lambert, D. L., & Cunha, K. 2004, A&A, 420, 183

Antoja, T., Figueras, F., Fernández, D., & Torra, J. 2008, A&A, 490, 135

Abia, C., & Rebolo, R. 1989, ApJ, 347, 186

Balachandran, S. 1990, Cool Stars, Stellar Systems, and the Sun, 9, 357

Balachandran, S. 1995, ApJ, 446, 203

Barnes, S. A. 2007, ApJ, 669, 1167

Bensby, T., Oey, M. S., Feltzing, S., & Gustafsson, B. 2007, ApJ, 655, L89

Binney, J., & Tremaine, S. 1987, Princeton, NJ, Princeton University Press, 1987, 747 p.,

Boesgaard, A. M., & Friel, E. D. 1990, ApJ, 351, 467

Bragaglia, A., & Tosi, M. 2006, Chemical Abundances and Mixing in Stars in the Milky Way and its Satellites, ESO ASTROPHYSICS SYMPOSIA. ISBN 978-3-540-34135-2. Springer-Verlag, 2006, p. 9, 9

Bragaglia, A. 2008, Memorie della Societa Astronomica Italiana, 79, 365

Carpenter, J. M., Snell, R. L., & Schloerb, F. P. 1995, ApJ, 450, 201

Carroll, B. W., & Ostlie, D. A. 1996, Institute for Mathematics and Its Applications,

Castelli, F., & Kurucz, R. L. 2004, arXiv:astro-ph/0405087

Castellani, V., Degl'Innocenti, S., Prada Moroni, P. G., & Tordiglione, V. 2002, MNRAS, 334, 193

Cenarro, A. J., et al. 2007, MNRAS, 374, 664

Clemens, D. P. 1985, ApJ, 295, 422

Cutri, R. M., et al. 2003, The IRSA 2MASS All-Sky Point Source Catalog, NASA/IPAC Infrared Science Archive. http://irsa.ipac.caltech.edu/applications/Gator/,

Davis, S. P., & Phillips, J. G. 1963, Berkeley Analyses of Molecular Spectra, Berkeley: University of California Press, 1963,

Dehnen, W. 1998, AJ, 115, 2384

Demarque, P., Woo, J.-H., Kim, Y.-C., & Yi, S. K. 2004, ApJS, 155, 667

De Silva, G. M., Sneden, C., Paulson, D. B., Asplund, M., Bland-Hawthorn, J., Bessell, M. S., & Freeman, K. C. 2006, AJ, 131, 455

De Silva, G. M., Freeman, K. C., Bland-Hawthorn, J., Asplund, M., & Bessell, M. S. 2007, AJ, 133, 694

De Silva, G. M., Freeman, K. C., Asplund, M., Bland-Hawthorn, J., Bessell, M. S., & Collet, R. 2007, AJ, 133, 1161

de Silva, G. M., Freeman, K. C., Bland-Hawthorn, J., & Asplund, M. 2008, Astronomical Society of the Pacific Conference Series, 396, 59

Elmegreen, B. G., & Efremov, Y. N. 1997, ApJ, 480, 235

Elmegreen, B. G., & Scalo, J. 2004, ARA&A, 42, 211

Eggen, O. J. 1958, MNRAS, 118, 65

Eggen, O. J. 1965, The Observatory, 85, 191

Eggen, O. J. 1969, PASP, 81, 553

Eggen, O. J. 1970, PASP, 82, 99

Eggen, O. J. 1996, AJ, 112, 1595

Eggen, O. J. 1996, AJ, 111, 1615

Famaey, B., Jorissen, A., Luri, X., Mayor, M., Udry, S., Dejonghe, H., & Turon, C. 2005, The Three-Dimensional Universe with Gaia, 576, 129

Famaey, B., Pont, F., Luri, X., Udry, S., Mayor, M., & Jorissen, A. 2007, A&A, 461, 957

Flynn, C., Sommer-Larsen, J., & Christensen, P. R. 1996, MNRAS, 281, 1027

Friel, E. D. 1995, ARA&A, 33, 381

Friel, E. D., Jacobson, H. R., & Pilachowski, C. A. 2005, AJ, 129, 2725

Friel, E. D. 2006, Chemical Abundances and Mixing in Stars in the Milky Way and its Satellites, ESO ASTROPHYSICS SYMPOSIA. ISBN 978-3-540-34135-2. Springer-Verlag, 2006, p. 3, 3

Gieles, M., Portegies Zwart, S. F., Baumgardt, H., Athanassoula, E., Lamers, H. J. G. L. M., Sipior, M., & Leenaarts, J. 2006, MNRAS, 371, 793

Girardi, L., Bressan, A., Bertelli, G., & Chiosi, C. 2000, A&AS, 141, 371

Gray, R. O., Corbally, C. J., Garrison, R. F., McFadden, M. T., Bubar, E. J., McGahee, C. E., O'Donoghue, A. A., & Knox, E. R. 2006, AJ, 132, 161

Gray, D. F. 1981, ApJ, 245, 992

Gray, D. F. 2005, The Observation and Analysis of Stellar Photospheres, 3rd Edition, by D.F. Gray. ISBN 0521851866. Cambridge, UK: Cambridge University Press, 2005

Hall, J. C., Lockwood, G. W., & Skiff, B. A. 2007, AJ, 133, 862

Hauck, B., & Mermilliod, M. 1997, VizieR Online Data Catalog, 2215, 0

Hinkle, K., Wallace, L., Valenti, J., & Harmer, D. 2000, Visible and Near Infrared Atlas of the Arcturus Spectrum 3727-9300 A ed. Kenneth Hinkle, Lloyd Wallace, Jeff Valenti, and Dianne Harmer. (San Francisco: ASP) ISBN: 1-58381-037-4, 2000.,

Holmberg, J., & Flynn, C. 2004, MNRAS, 352, 440

Holmberg, J., Nordström, B., & Andersen, J. 2007, A&A, 475, 519

Friel, E. D., Jacobson, H. R., & Pilachowski, C. A. 2005, AJ, 129, 2725

Jacobson, H. R., Friel, E. D., & Pilachowski, C. A. 2007, AJ, 134, 1216

Jacobson, H. R., Friel, E. D., & Pilachowski, C. A. 2008, AJ, 135, 2341

Johnson, D. R. H., & Soderblom, D. R. 1987, AJ, 93, 864

Jones, B. F., Fischer, D., & Soderblom, D. R. 1999, AJ, 117, 330

Kaehler, H. 1978, The HR Diagram - The 100th Anniversary of Henry Norris Russell, 80, 303

Kuijken, K., & Gilmore, G. 1989, MNRAS, 239, 605

King, J. R., Deliyannis, C. P., Hiltgen, D. D., Stephens, A., Cunha, K., & Boesgaard, A. M. 1997, AJ, 113, 1871

King, J. R., Stephens, A., Boesgaard, A. M., & Deliyannis, C. 1998, AJ, 115, 666

King, J. R., Krishnamurthi, A., & Pinsonneault, M. H. 2000, AJ, 119, 859

King, J. R., Villarreal, A. R., Soderblom, D. R., Gulliver, A. F., & Adelman, S. J. 2003, AJ, 125, 1980

King, J. R., & Schuler, S. C. 2005, PASP, 117, 911

King, J. R., Schuler, S. C., Hobbs, L. M., & Pinsonneault, M. H., 2009, SUBMITTED

King, I. R. 1966, AJ, 71, 64

Kramer, C., Stutzki, J., Rohrig, R., & Corneliussen, U. 1998, A&A, 329, 249

Kupka, F., & Ryabchikova, T. A. 1999, Publications de l'Observatoire Astronomique de Beograd, 65, 223

Kupka, F. G., Ryabchikova, T. A., Piskunov, N. E., Stempels, H. C., & Weiss, W. W. 2000, Baltic Astronomy, 9, 590

Kurucz, R. L. 2005, Memorie della Societa Astronomica Italiana Supplement, 8, 189

Lada, E. A., Bally, J., & Stark, A. A. 1991, ApJ, 368, 432

Lada, E. A., Depoy, D. L., Evans, N. J., II, & Gatley, I. 1991, ApJ, 371, 171

Lada, C. J., Young, E. T., & Greene, T. P. 1993, ApJ, 408, 471

Lada, C. J., & Lada, E. A. 2003, ARA&A, 41, 57

Lamers, H. J. G. L. M., Gieles, M., Bastian, N., Baumgardt, H., Kharchenko, N. V., & Portegies Zwart, S. 2005, A&A, 441, 117

Lamers, H. J. G. L. M., & Gieles, M. 2006, A&A, 455, L17

Luyten, W. J. 1926, The Scientific Monthly, 22, 494

Mamajek, E. E., Meyer, M. R., & Liebert, J. 2002, AJ, 124, 1670

Mamajek, E. E., & Hillenbrand, L. A. 2008, ApJ, 687, 1264

McDonald, A. R. E., & Hearnshaw, J. B. 1983, MNRAS, 204, 841

Mermilliod, J.-C., Mayor, M., & Udry, S. 2009, A&A, 498, 949

Mihalas, D., & Routly, P. M. 1968, A Series of Books in Astronomy and Astrophysics, San Francisco: W.H. Freeman and Company, —c1968,

Mihalas, D. 1978, San Francisco, W. H. Freeman and Co., 1978. 650 p.,

Mishenina, T. V., Bienaymé, O., Gorbaneva, T. I., Charbonnel, C., Soubiran, C., Korotin, S. A., & Kovtyukh, V. V. 2006, A&A, 456, 1109

Morales, J. C., Ribas, I., & Jordi, C. 2008, A&A, 478, 507

Nordström, B., et al. 2004, A&A, 418, 989

Paulson, D. B., Sneden, C., & Cochran, W. D. 2003, AJ, 125, 3185

Perryman, M. A. C., & ESA 1997, The Hipparcos and Tycho catalogues. Astrometric and photometric star catalogues derived from the ESA *HIPPARCOS* Space Astrometry Mission, Publisher: Noordwijk, Netherlands: ESA Publications Division, 1997, Series: ESA SP Series vol no: 1200, ISBN: 9290923997 (set),

Perryman, M. A. C., et al. 1998, A&A, 331, 81

Piskunov, N. E., Kupka, F., Ryabchikova, T. A., Weiss, W. W., & Jeffery, C. S. 1995, A&AS, 112, 525

Piskunov, A. E., Schilbach, E., Kharchenko, N. V., Roeser, S., & Scholz, R.-D. 2007, VizieR Online Data Catalog, 346, 80151

Piskunov, A. E., Schilbach, E., Kharchenko, N. V., Röser, S., & Scholz, R.-D. 2008, A&A, 477, 165

Piskunov, A. E., Kharchenko, N. V., Schilbach, E., Röser, S., Scholz, R.-D., & Zinnecker, H. 2008, A&A, 487, 557

Phelps, R. L., & Lada, E. A. 1997, ApJ, 477, 176

Ramírez, I., & Meléndez, J. 2005, ApJ, 626, 465

Randich, S., Gratton, R., Pallavicini, R., Pasquini, L., & Carretta, E. 1999, A&A, 348, 487

Roberts, M. S. 1957, PASP, 69, 59

Ryabchikova, T. A., Piskunov, N. E., Kupka, F., & Weiss, W. W. 1997, Baltic Astronomy, 6, 244

Salasnich, B., Girardi, L., Weiss, A., & Chiosi, C. 2000, A&A, 361, 1023

Schuler, S. C., King, J. R., Fischer, D. A., Soderblom, D. R., & Jones, B. F. 2003, AJ, 125, 2085

Schuler, S. C., King, J. R., Hobbs, L. M., & Pinsonneault, M. H. 2004, ApJ, 602, L117

Schuler, S. C., Hatzes, A. P., King, J. R., Kürster, M., & The, L.-S. 2006, AJ, 131, 1057

Schuler, S. C., King, J. R., & The, L. -. 2009, arXiv:0906.4812

Schilbach, E., Kharchenko, N. V., Piskunov, A. E., Röser, S., & Scholz, R.-D. 2006, A&A, 456, 523

Sanders, D. B., Solomon, P. M., & Scoville, N. Z. 1984, ApJ, 276, 182

Sestito, P., Randich, S., & Pallavicini, R. 2004, A&A, 426, 809

Skrutskie, M. F., et al. 2006, AJ, 131, 1163

Skuljan, J., Hearnshaw, J. B., & Cottrell, P. L. 1999, MNRAS, 308, 731

Smith, V. V., et al. 2002, AJ, 124, 3241

Sneden, C. A. 1973, Ph.D. Thesis,

Soderblom, D. R., & Mayor, M. 1993, AJ, 105, 226

Sousa, S. G., et al. 2008, A&A, 487, 373

Spitzer, L. J. 1958, ApJ, 127, 17

Spitzer, L., Jr., & Shull, J. M. 1975, ApJ, 201, 773

Stahler, S. W., & Palla, F. 2005, The Formation of Stars, by Steven W. Stahler, Francesco Palla, pp. 865. ISBN 3-527-40559-3. Wiley-VCH , January 2005.,

Takeda, Y. 2003, A&A, 402, 343

Takeda, Y., Zhao, G., Takada-Hidai, M., Chen, Y.-Q., Saito, Y.-J., & Zhang, H.-W. 2003, Chinese Journal of Astronomy and Astrophysics, 3, 316

Taylor, B. J. 1994, Bulletin of the American Astronomical Society, 26, 1382

Teuben, P. 1995, Astronomical Data Analysis Software and Systems IV, 77, 398

Thevenin, F. 1990, A&AS, 82, 179

Torres, G., & Ribas, I. 2002, ApJ, 567, 1140

Tuominen, I. V., & Vilhu, O. 1979, Liege International Astrophysical Colloquia, 22, 355

Updike, A. C., Hartmann, D. H., Greiner, J., & Klose, S. 2009, American Institute of Physics Conference Series, 1133, 257

Valenti, J. A., & Fischer, D. A. 2005, ApJS, 159, 141

van den Bergh, S., & Lafontaine, A. 1984, AJ, 89, 1822

van Leeuwen, F. 2007, A&A, 474, 653

van Leeuwen, F. 2008, VizieR Online Data Catalog, 1311, 0

Vilhu, O., Tuominen, I., Kyrolainen, J., & Holsti, N. 1978, Nauchnye Informatsii, 45, 90

Whitworth, A. 1979, MNRAS, 186, 59

Wielen, R. 1985, Dynamics of Star Clusters, 113, 449

Yong, D., Lambert, D. L., Allende Prieto, C., & Paulson, D. B. 2004, ApJ, 603, 697